Monitoring Amyloid Aggregation *via* Twisted Intramolecular Charge Transfer (TICT)-Based Fluorescent Sensor Array

Chao Wang,[a, b, #] Wenchao Jiang,[a, d, #] Davin Tan,[b] Lu Huang,[b, c] Jin Li,[a, d] Qinglong Qiao,[a] Priya Yadav,[b] Xiaogang Liu,[b, *] and Zhaochao Xu[a, d, *]

[a] Dr. C. Wang, W. Jiang, Dr. Q. Qiao, Prof. Dr. Z. Xu, CAS Key Laboratory of Separation Science for Analytical Chemistry, Dalian Institute of Chemical Physics, Chinese Academy of Sciences, 457 Zhongshan Road, Dalian 116023 (China)
E-mail: zcxu@dicp.ac.cn

[b] Dr. C. Wang, Prof. Dr. L. Huang, Prof. Dr. X. Liu, Fluorescence Research Group Singapore University of Technology and Design, 8 Somapah Road, Singapore 487372 (Singapore)
E-mail: xiaogang_liu@sutd.edu.sg

[c] Prof. Dr. L. Huang, Ocean College, Minjiang University, Fuzhou 350108 (China)

[d] W. Jiang, J. Li, Prof. Dr. Z. Xu, University of Chinese Academy of Sciences, Beijing 100049 (China)

Content

1. Computational and Experimental Details

1.1 Computational details

All density functional theory (DFT) and time-dependent density functional theory (TD-DFT) calculations were performed with *Gaussian 16* software.[1] The excited-state geometries were optimized at the *ω*B97XD/Def2SVP level for cyanines and hemi-cyanines and the CAM-B3LYP/Def2SVP level for other fluorophores in water. The use of *ω*B97XD/Def2SVP for the geometry optimization of cyanine derivatives is reasonable as this theory can provide a balanced description of the delocalization and localization over the π-conjugated bridge in cyanines and polymethines.[2] SMD atomic radii[3] was applied to replace the original UFF atomic radii in the PCM solvent model along with the linear response (LR-PCM)[4] formalism for geometry optimization and with the corrected linear response (cLR-PCM)[5] for calculating the total energies on the potential energy surfaces for describing TICT tendency. The cLR-PCM solvent formalism along with SMD atomic radii has been proven reliable for describing the TICT formation.[6]

The mean localization distance (d_{LOL}) measures the degree of conjugation of the molecule using the localized orbital locator (LOL).[7, 8] A large d_{LOL} value suggests an extensive conjugation. Natural transition orbitals (NTOs)[9] can provide more compact molecular orbital presentations for LE, ICT, and TICT states. Charge transfer distance (d_{CT})[10] can quantitatively measure the degree of intramolecular charge transfer. The molecular volume based on an improved Marching Tetrahedra algorithm[11] and

distance projection map can qualify the spatial parameters of the fluorophore. We used Multiwfn 3.4.0 to calculate d_{LOL}, NTOs, d_{CT}, molecular volume, and distance projection map.[12]

1.2 Materials and instruments

All common reagents were purchased from commercial suppliers (Sigma-Aldrich, J&K, Innochem, and Aladdin) and used without further purification. Solvents such as dimethyl sulfoxide (DMSO), methanol, ethanol, chloroform, and acetonitrile were purchased from J&K; silica gel (200-300 mesh) was purchased from Innochem.

The ^{1}H-NMR and ^{13}C-NMR spectra were recorded on a Bruker 400 spectrometer, with tetramethylsilane (TMS) as the internal standard. Chemical shifts were given in ppm and coupling constants (J) in Hz. High-resolution mass spectrometry (HRMS) data were recorded using ESI (6540 UHD Q-TOF, positive ion). UV-vis absorption spectra were collected on an Agilent Cary 60 UV-Vis Spectrophotometer. Fluorescence measurements were observed on an Agilent CARY Eclipse fluorescence spectrophotometer. Confocal images were performed on Olympus FV1000 MPE with a microscope IX 71, a 100× / NA 1.40 oil objective lens, LU-NV series laser unit (laser combination: 488 nm; 543 nm). The single-photon confocal microscope system was built on an Olympus inverted microscope IX81. Structured illumination microscopy (SIM) super-resolution images were detected on a Nikon N-SIM system with a 100×oil immersion objective lens, 1.49 NA (Nikon). Images were captured using Nikon NIS-Elements and reconstructed using slice reconstruction in NIS elements.

1.3 Experimental procedures

1.3.1 Spectral measurements in the different solvents

The probe stock solution (2 mM) was prepared in DMSO. The UV−vis absorption and fluorescence spectra of **A1-A5**, **B1-B5**, and **C1-C5** were measured in different solvents, including toluene, $CHCl_3$, DCM, Dioxane, EA, EtOH, MeCN, MeOH, DMSO, and PBS 7.4, at a concentration of 5 *μ*M (except for **A3**, **B3**, and **C3** at 10 *μ*M).

The viscosity response of the dye was carried out at 25 °C. In this experiment, the concentration of the dye solution was the same as those for the solvent response, and the dyes were incubated in a methanol-glycerol mixture with varying viscosity.

Coumarin 153, Rhodamine 6G, Rhodamine 101, and Oxazine 1 were used to obtain fluorescence quantum yields of other compounds using the relative determination method. For example, the fluorescence quantum yield of Coumarin 153 is 0.53 in ethanol, Rhodamine 6G is 0.91 in ethanol, Rhodamine 101 is 0.915 in ethanol, and Oxazine 1 is 0.15 in ethanol. The quantum yield (*φ*) was calculated using the following equation:[13]

$$\varphi F_{(X)} = \varphi F_{(S)} \cdot (A_S F_X / A_X F_S)(\eta_X / \eta_S)^2$$

where *φ*F, A, and F represent the fluorescence quantum yield, the absorbance at the excitation wavelength, and the area under the corrected emission curve. *η* is the refractive index of the solvent. Subscripts X and S refer to the unknown and the standard samples, respectively.

1.3.2 A*β* Peptide Pretreatment and Measuring aggregation kinetics of A*β*

Aβ Peptide Pretreatment:

Amyloid-*β* 1−40 (Aβ40, >95%) was purchased from Synpeptide Co., Ltd. (China). A standard method was used to prepare the A*β*40 peptide solution (J. Am. Chem. Soc. 2014, 136, 30, 10736–10742). The A*β*40 peptide powder was first dissolved in HFIP at a concentration of 1 mg/mL and incubated at 25 °C for 2 h. The stock solution was

then dried under a gentle stream of nitrogen to remove HFIP, followed by vacuum drying. The peptide was dissolved in 100 μL DMSO and stored at −20 °C. Before use, the peptide in DMSO was diluted with phosphate buffer solution (PBS) (10 mM, pH 7.4) to the desired concentration and thoroughly mixed by vortexing.

Measuring aggregation kinetics of Aβ:

50 μM dyes (**ThT**, **A3**-**A5**, **B3**-**B5**, **C3**-**B5**) were added separately to 50 μM A*β*40 peptide (buffer condition: 10 mM PBS, pH 7.4). A 200 μL protein-dye mixture (final concentration of both dye and protein was 25 μM) was loaded into a clear bottom 96-well plate (each "protein-dye" sample was repeated in three parallel experiments). Fluorescence data were recorded using a Synergy™ H1M Multifunctional Microplate Tester with a bottom-reading mode in 96-well flat bottom plates sealed with a PlateMax film. Plates were shaken for 2 s before reading fluorescent data every 10 min. Fluorescence intensities were measured at Ex = 450 nm/Em = 510 nm for **ThT**, **A3**, **B3**, and **C3**; Ex = 560 nm/Em = 610 nm for **A4**, **B4**, and **C4**; Ex = 640 nm/Em = 700 nm for **A5**, **B5**, and **C5**.

1.3.3 Confocal imaging of A*β* fibrillar structures

A confocal laser scanning microscope Olympus FV1000 MPE was used to obtain the fluorescence images of the **A4**-, **B3**-, **C3**-, and **ThT**- stained fibrillar structures. After the kinetics measurements, the samples from Aβ aggregates were attached to the culture dish, which was stored in the refrigerator at 4 °C for 30 minutes before using it for imaging.

1.3.4 Structured illumination microscopy (SIM) super-resolution imaging of Aβ fibrillar structures

We obtained the super-resolution imaging of the **A4**-, **B3**-, **C3**-and, **ThT**- stained fibrillar structures using a Nikon N-SIM system with a 100×oil immersion objective lens,

1.49 NA (Nikon). Sample preparation was the same as that for confocal imaging. Images were captured using Nikon NIS-Elements and reconstructed using slice reconstruction.

2. Additional Computational Results for Establishing the TICT Tuning Framework

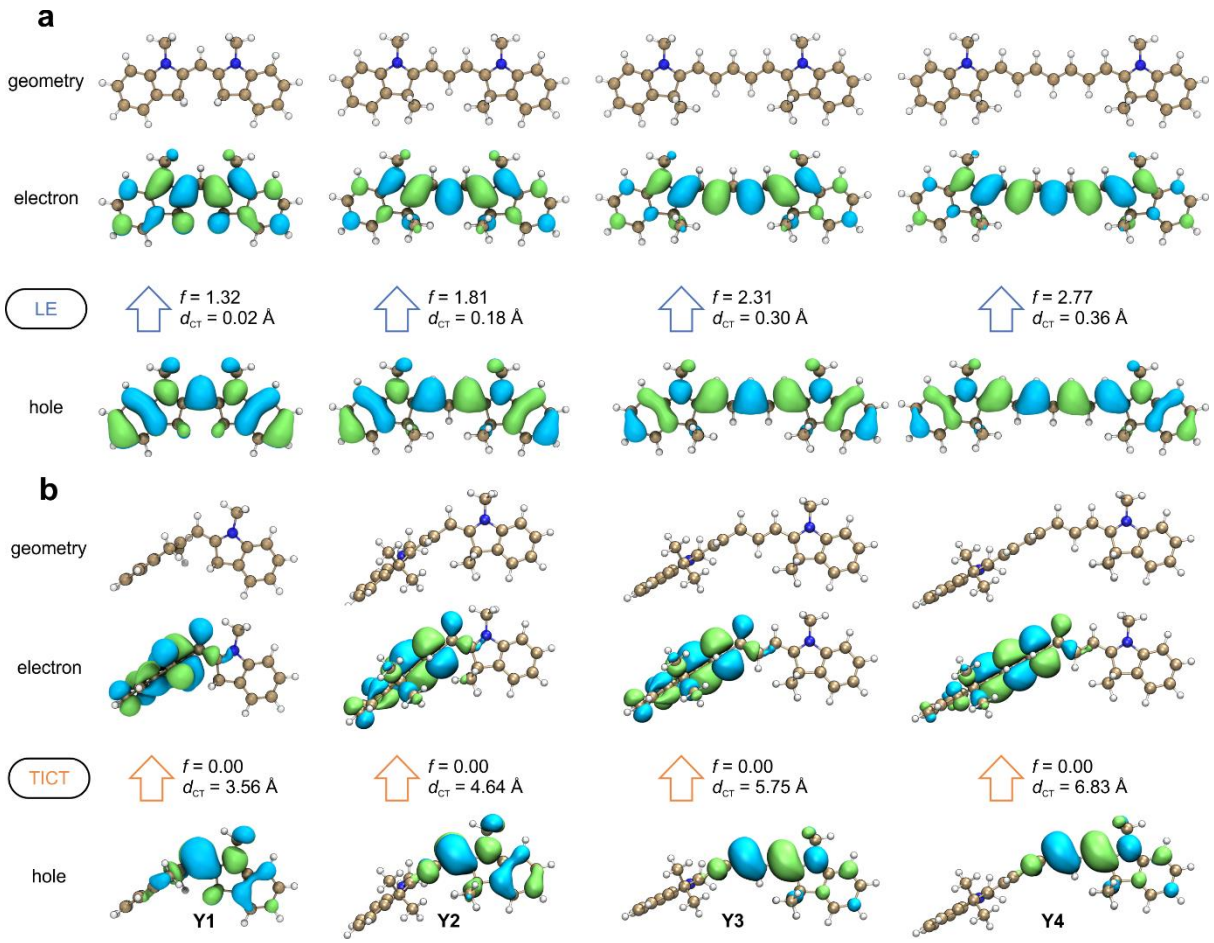

*Figure S1. NTOs of (a) LE and (b) TICT states of **Y1** – **Y4** optimized at the ωB97XD/Def2SVP level in the water. The corresponding oscillator strength (f) and charge transfer distance (d_{CT}) are labeled in the inset.*

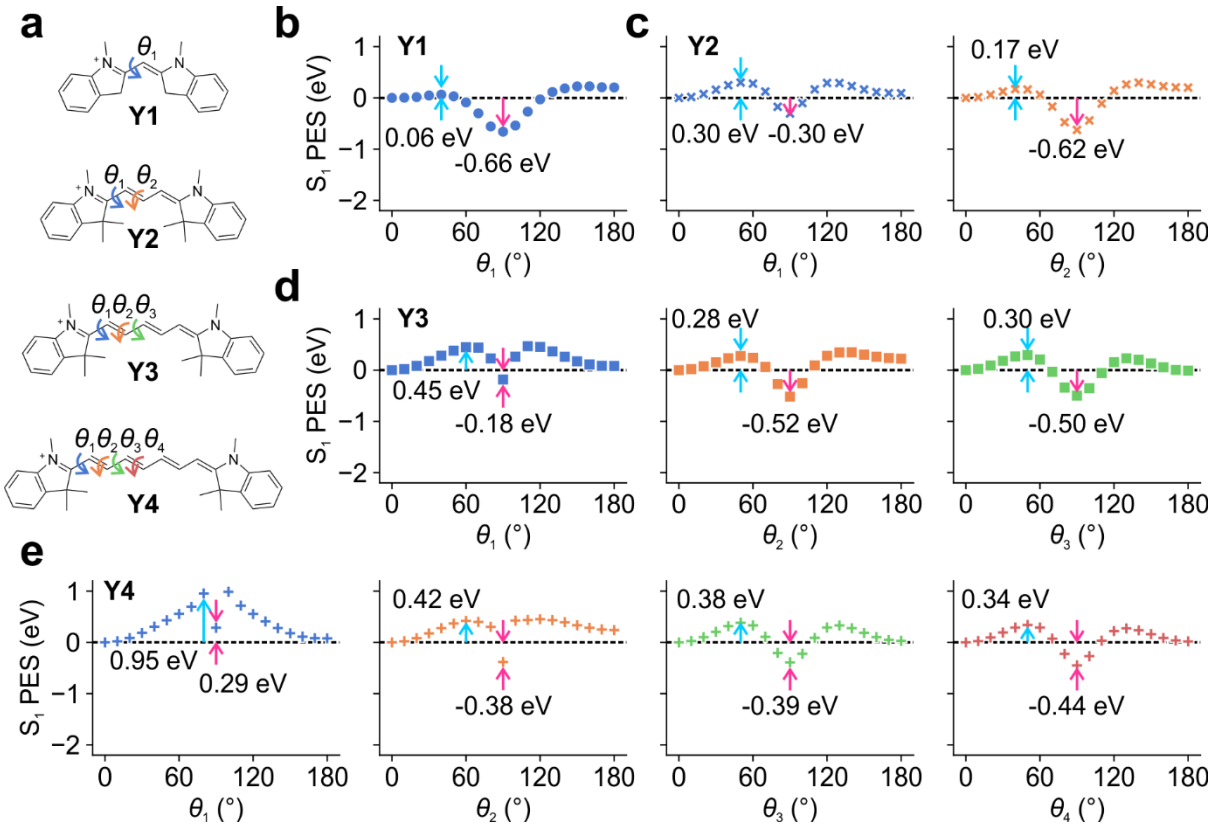

*Figure S2. (a) Chemical structures of **Y1** – **Y4** and different rotating angles for TICT. Calculated S_1 PES for TICT of (b) **Y1**, (c) **Y2**, (d) **Y3**, and (e) **Y4** at the ωB97XD/Def2SVP/cLR-PCM level in the water.*

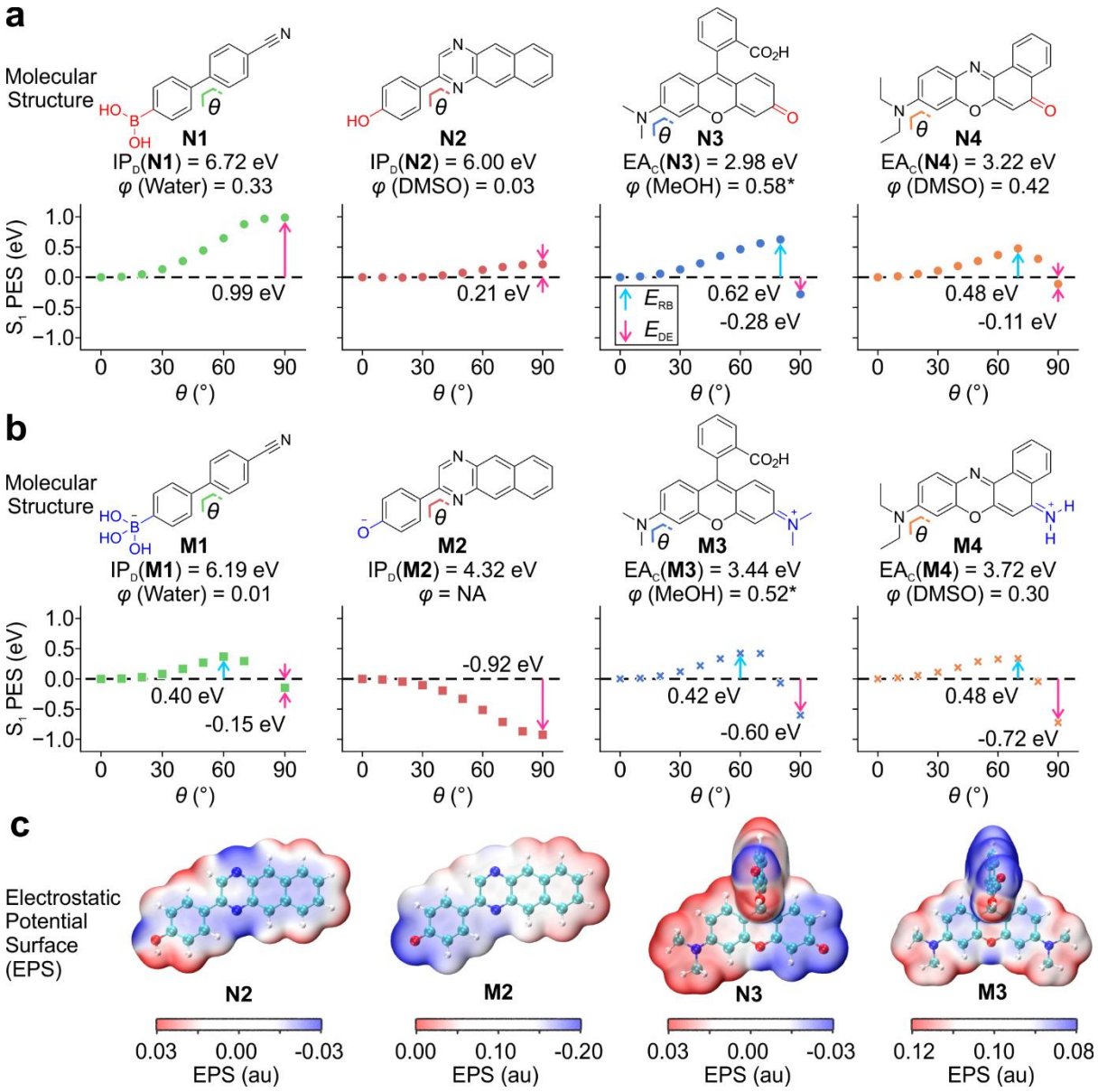

*Figure S3. Calculated S_1 PESs for TICT of (a) **N1** – **N4** and (b) **N1** – **N4** at the CAM-B3LYP/Def2SVP/cLR-PCM level in the water. The rotation barrier (E_{RB}), driving energy (E_{DE}), and quantum yield (φ) [14-17] were labeled in the inset. As we cannot find φ of **N4** and **M4** in aprotic solvents, we adapted data from their diethylamino-substituted analogs in MeOH.[17] (c) Electrostatic potential surfaces (EPSs) of **N2**, **M2**, **N3**, and **M3**. The vertical ionic potential of donor fragments and the electron affinity of chromophore fragments are calculated at the B3LYP/Def2SVP level in the water and labeled in the inset.*

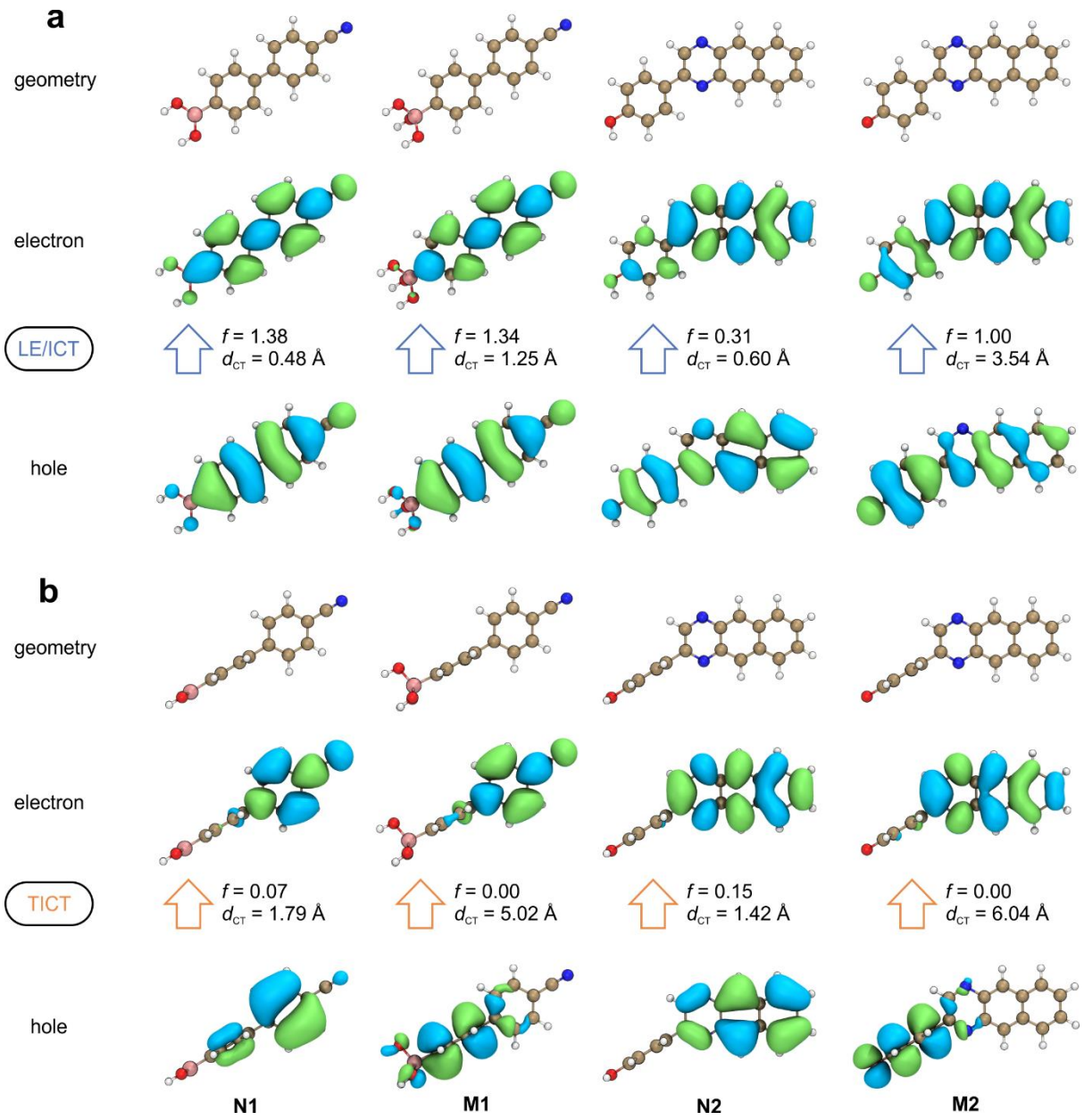

*Figure S4. NTOs of (a) LE and (b) TICT states of **N1** – **N2** and **M1** – **M2** were optimized at the CAM-B3LYP/Def2SVP level in the water. The corresponding oscillator strength (f) and charge transfer distance (d_{CT}) are labeled in the inset.*

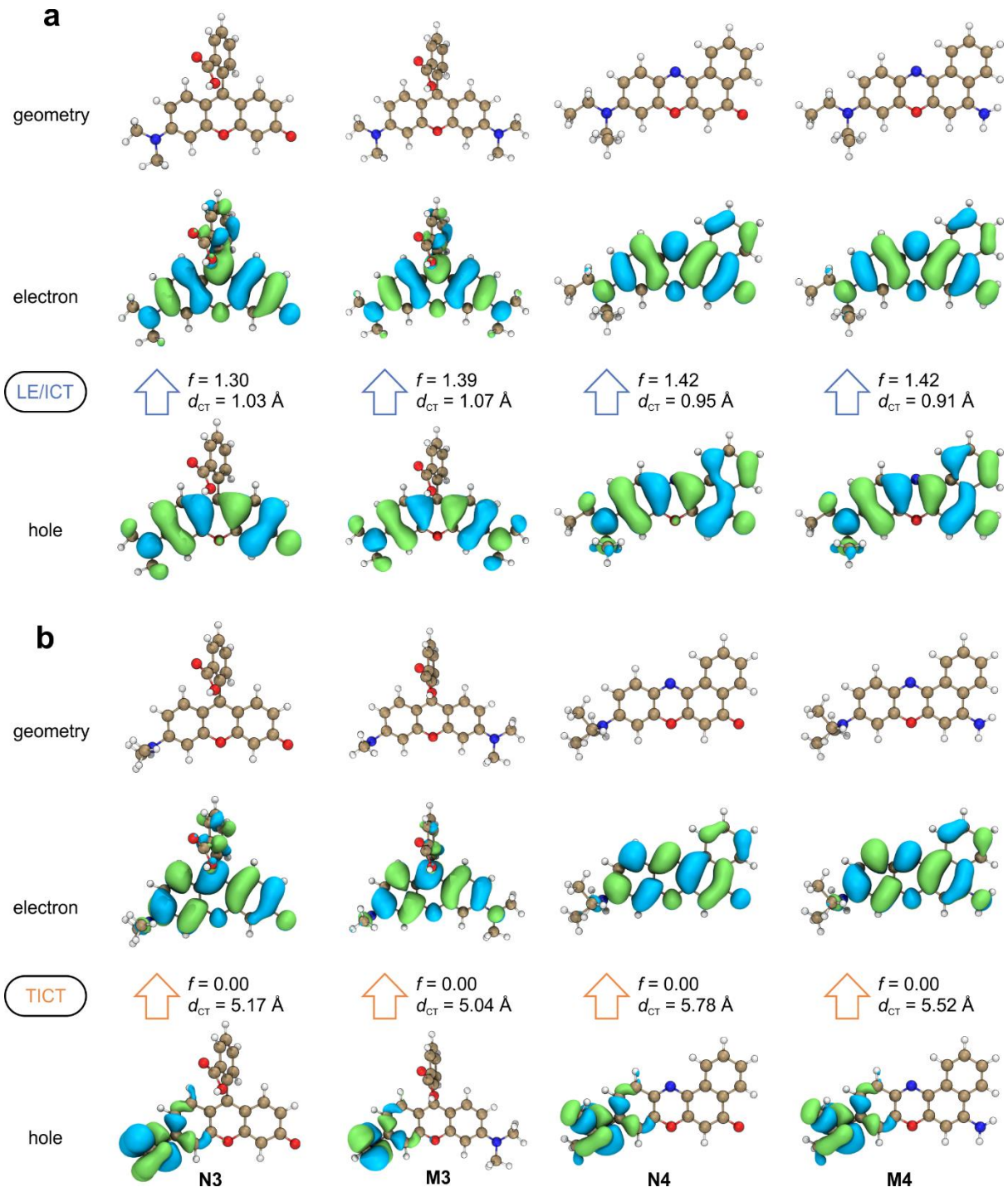

*Figure S5. NTOs of (a) LE and (b) TICT states of **N3** – **N4** and **M3** – **M4** optimized at the CAM-B3LYP/Def2SVP level in the water. The corresponding oscillator strength (f) and charge transfer distance (d_{CT}) are labeled in the inset.*

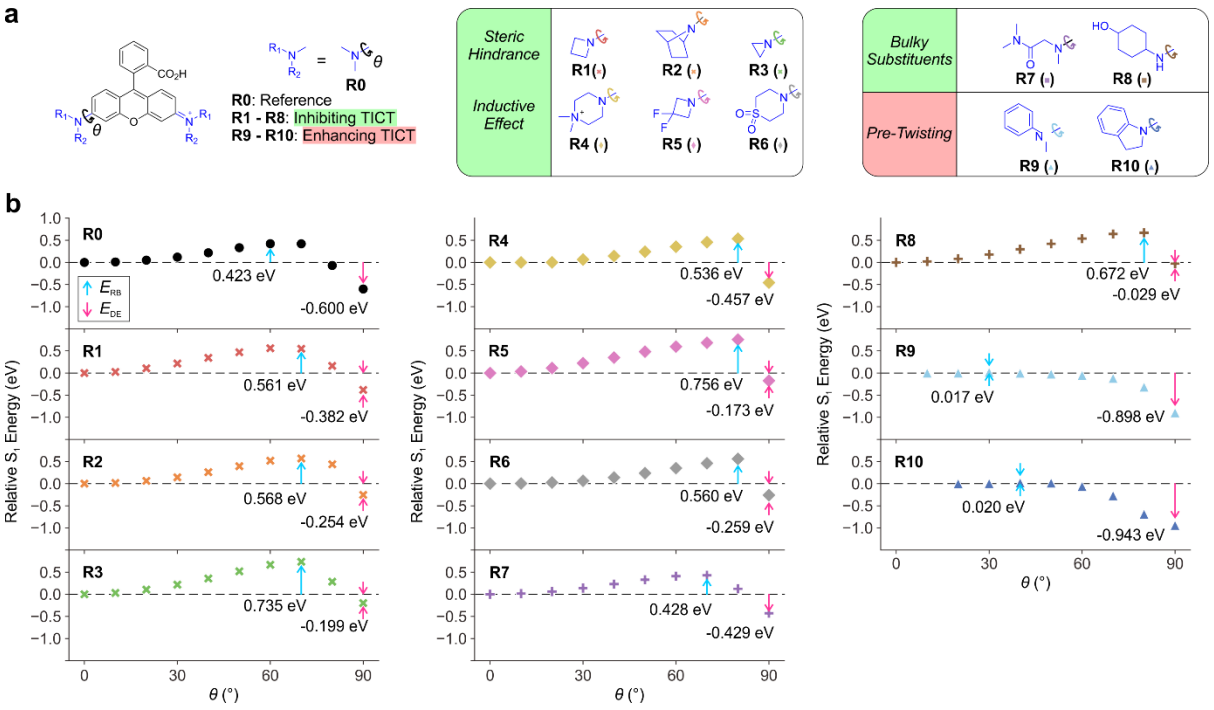

*Figure S6. (a) Chemical structures of rhodamine derivatives for inhibiting and enhancing TICT, respectively. (b) S_1 PES for TICT of **R0**-**R10** was calculated using CAM-B3LYP/Def2SVP/cLR-PCM level in the water. The rotation barrier (E_{RB}) and driving energy (E_{DE}) are labeled in the inset.*

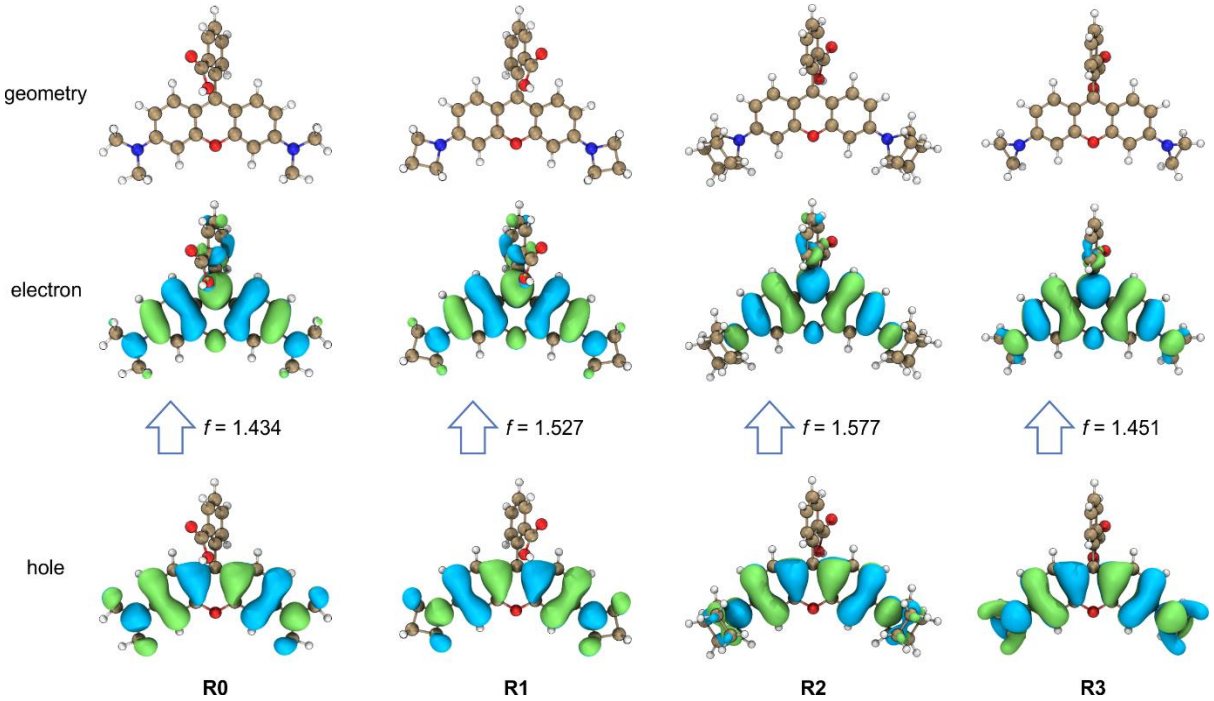

*Figure S7. NTOs of LE state of **R0** – **R3** optimized at the CAM-B3LYP/Def2SVP level in the water. The corresponding oscillator strength (f) is labeled in the inset.*

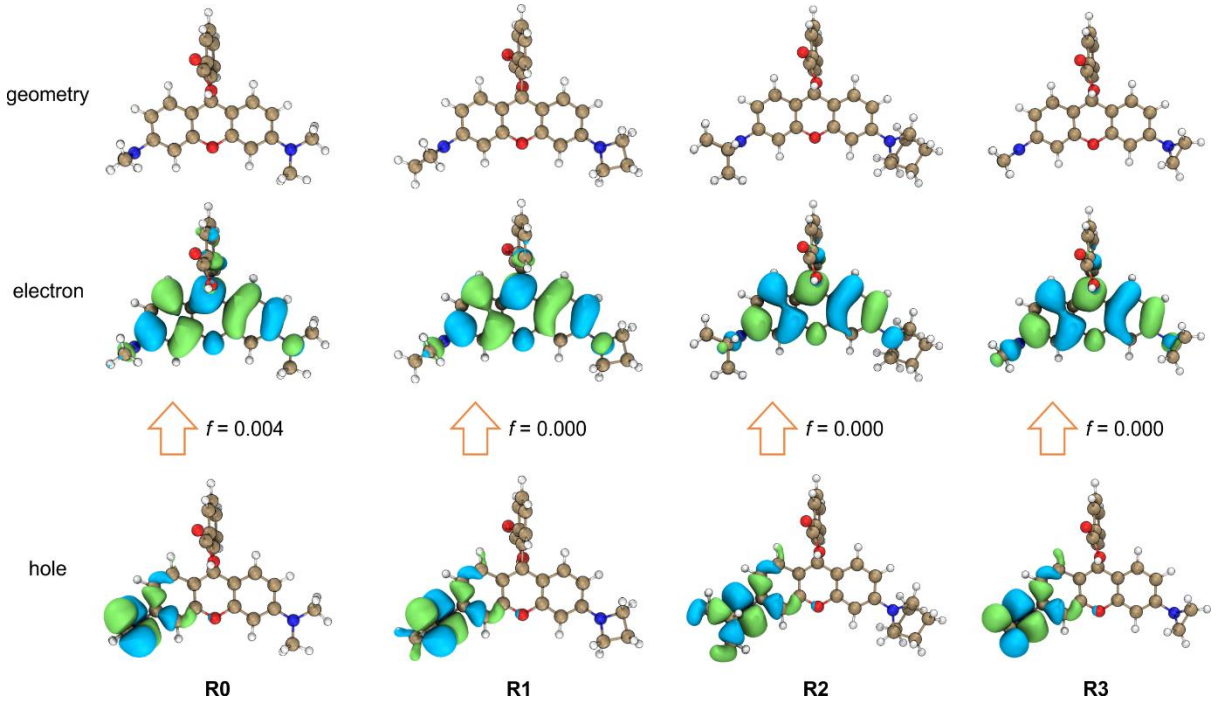

*Figure S8. NTOs of TICT state of **R0** – **R3** optimized at the CAM-B3LYP/Def2SVP level in the water. The corresponding oscillator strength (f) is labeled in the inset.*

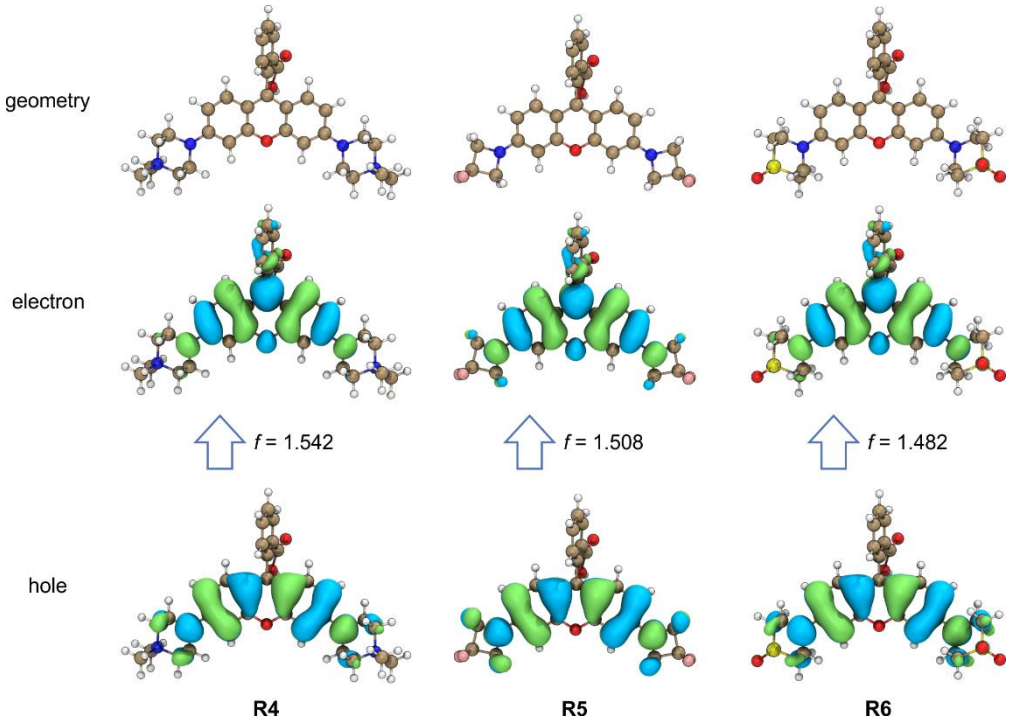

*Figure S9. NTOs of LE state of **R4** – **R6** optimized at the CAM-B3LYP/Def2SVP level in the water. The corresponding oscillator strength (f) is labeled in the inset.*

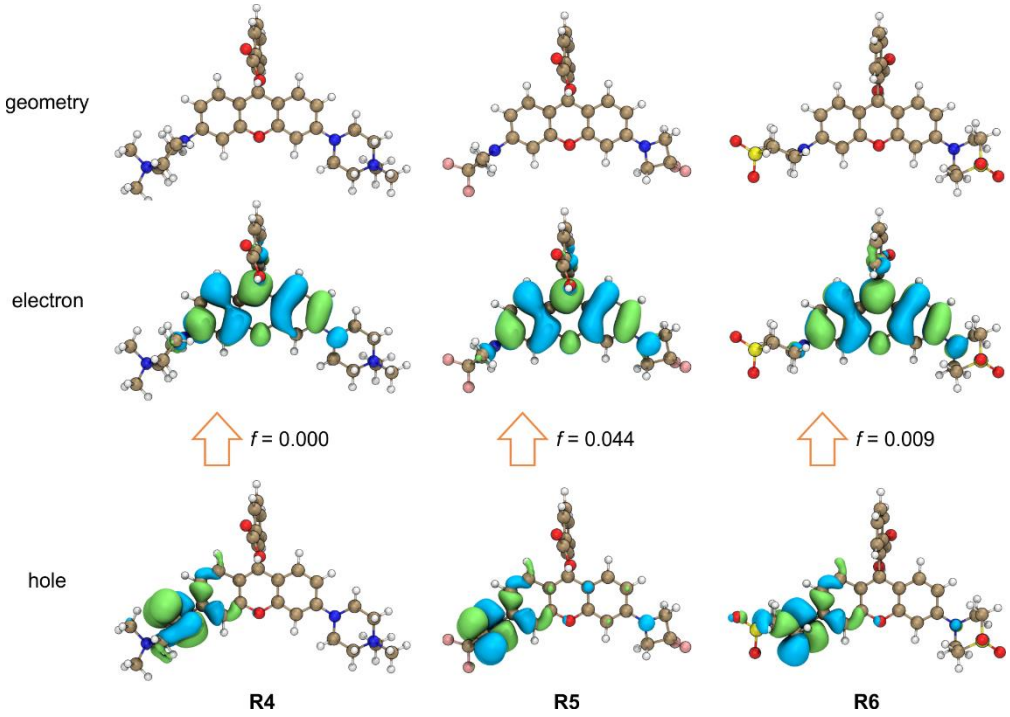

*Figure S10. NTOs of TICT state of **R4** – **R6** optimized at the CAM-B3LYP/Def2SVP level in the water. The corresponding oscillator strength (f) is labeled in the inset.*

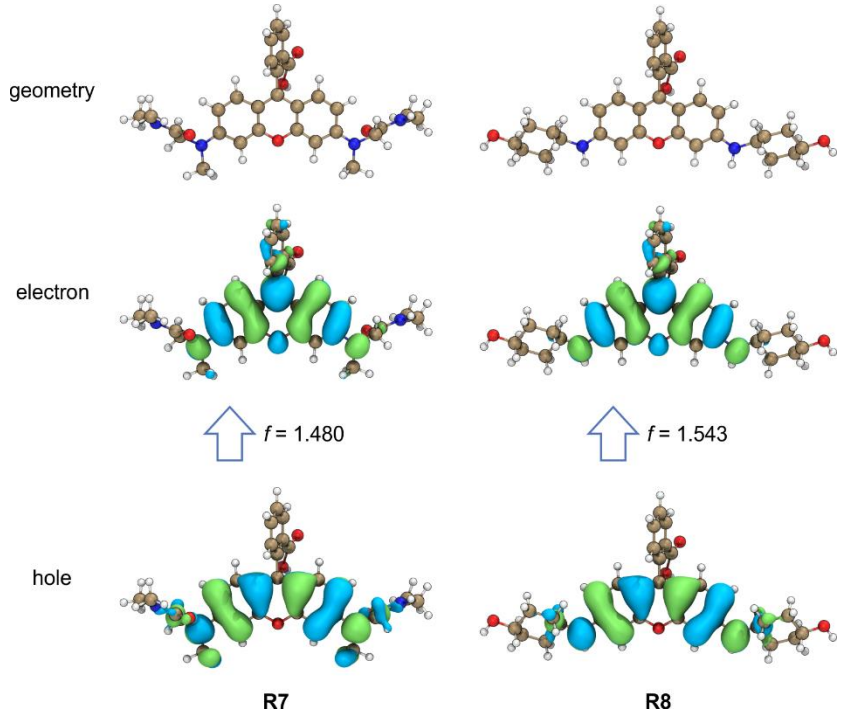

*Figure S11. NTOs of LE state of **R7** – **R8** optimized at the CAM-B3LYP/Def2SVP level in the water. The corresponding oscillator strength (f) is labeled in the inset.*

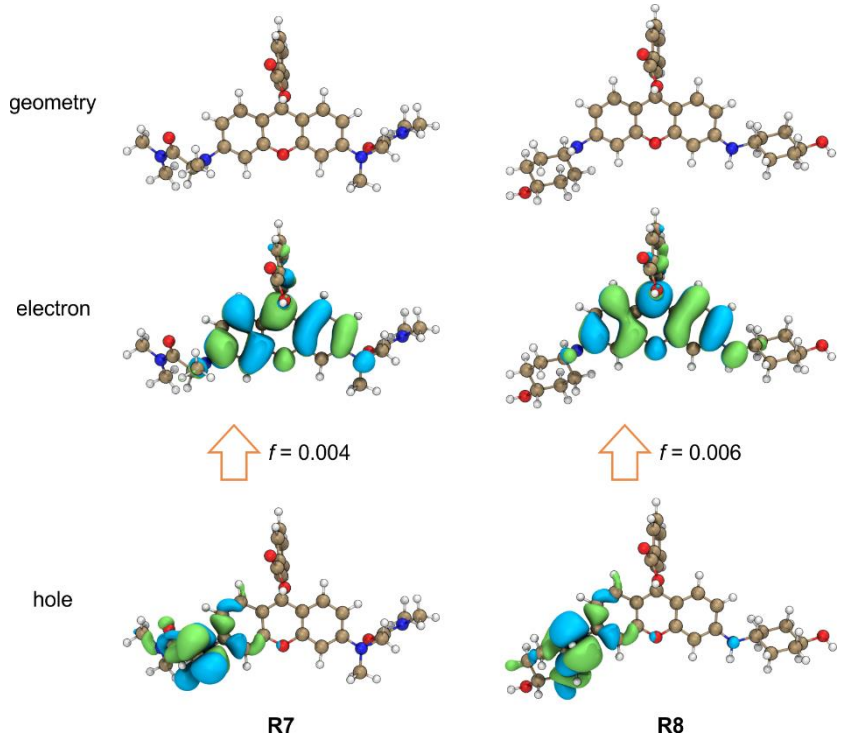

*Figure S12. NTOs of TICT state of **R7** – **R8** optimized at the CAM-B3LYP/Def2SVP level in the water. The corresponding oscillator strength (f) is labeled in the inset.*

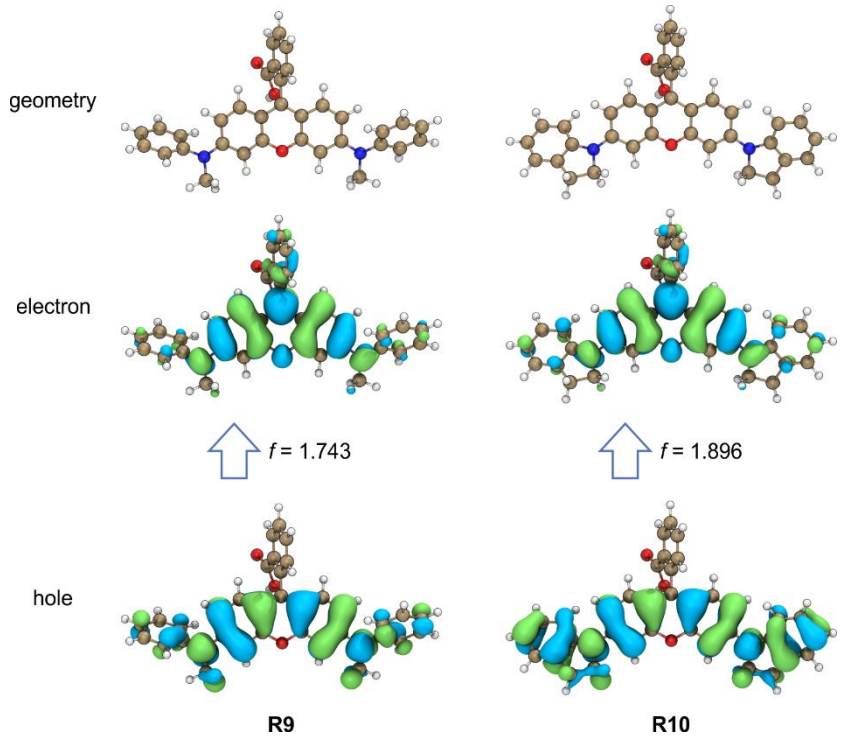

*Figure S13. NTOs of LE state of **R9** – **R10** optimized at the CAM-B3LYP/Def2SVP level in the water. The corresponding oscillator strength (f) is labeled in the inset.*

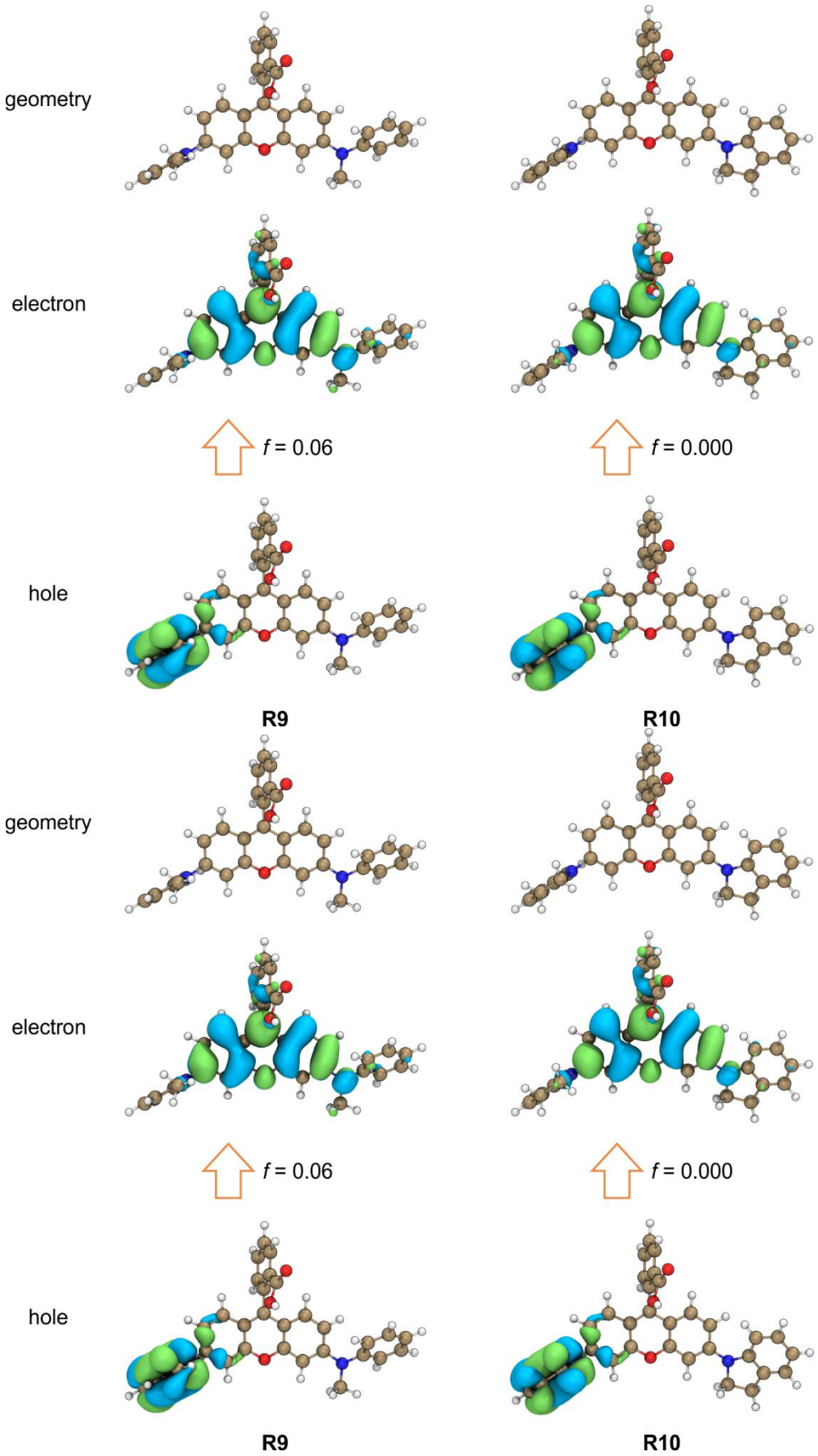

*Figure S14. NTOs of TICT state of **R9** – **R10** optimized at the CAM-B3LYP/Def2SVP level in the water. The corresponding oscillator strength (f) is labeled in the inset.*

3. Synthesis of Hemi-Cyanine Derivatives

3.1 Synthesis of S1 and PC1

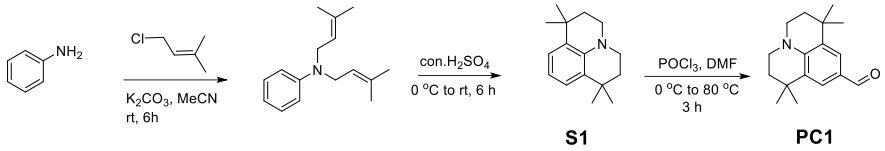

*Scheme S1. The synthesis procedure of **S1** and **PC1***

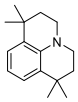

1,1,7,7-tetramethyl-2,3,6,7-tetrahydro-1H,5H-pyrido[3,2,1-ij] quinoline (**S1**): To a stirred solution of aniline (2 g, 21.5 mmol,1 eq.) in MeCN (50 mL), K_2CO_3 (6.23 g, 45.0mmol, 2.1eq), molecular sieves (MS 4Å) (2 g) and 1-chloro-3- methylbut-2-ene (5.6 g, 53.7 mmol, 2.5 eq) were added, respectively. The resultant mixture was allowed to stir for 6 h at room temperature. The reaction mixture was filtered, and the filtrate was concentrated in vacuo. The crude mixture was purified by a silica gel column chromatography (PE/EA= 30:1) to obtain the compound N, N-bis(3-methylbut-2-en-1-yl) aniline (2.9 g, 59% yield) as a colorless oily liquid for next reaction. Concentrated sulfuric acid was added to N, N-bis(3-methylbut-2-en-1-yl) aniline (2.9 g.) at 0 °C, then warmed to room temperature and stirred vigorously for 6 h. The solution was poured into ice water, extracted with CH_2Cl_2, dried over Na_2SO_4, filtered, and evaporated. The residue was purified by flash column chromatography (silica gel, PE/EA = 30/1) to afford **S1** (900 mg, 31% yield).^{1}H NMR (400 MHz, $CDCl_3$) δ 7.05 (d, J = 7.6 Hz, 2H), 6.61 (d, J = 6.9 Hz, 1H), 3.28 – 2.96 (m,4H), 1.87 – 1.65 (m, 4H), 1.29 (s, 12H).

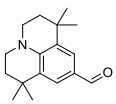

1,1,7,7-tetramethyl-2,3,6,7-tetrahydro-1H,5H-pyrido[3,2,1-ij]quinoline-9-carbaldehyde (**PC1**): $POCl_3$ (3.6 mL, 10 eq) and DMF (6 mL, 20 eq) were stirred

together in a flask for 30 min at 0 °C before **S1** solution (900 mg, 3.9 mmol) in anhydrous DMF (4 mL) was added slowly. The resulting mixture was stirred at 80 ℃ for 8 h. After cooling to room temperature, the solution was poured into ice water, neutralized with sodium bicarbonate, and extracted with EA. The combined extracts were dried over Na_2SO_4, filtered, and evaporated. The residue was purified by flash column chromatography (silica gel, PE/EA = 20/1 to 5/1) to afford **PC1** (725 mg, 71.8% yield) as a white solid.^{1}H NMR (400 MHz, $CDCl_3$) δ 9.54 (s, 1H), 7.45 (s, 2H), 3.38 – 2.95 (m, 4H), 1.77 – 1.52 (m, 4H), 1.19 (s, 12H).

3.2 Synthesis of A1, B1, C1, A3, B3, C3, and the corresponding intermediates

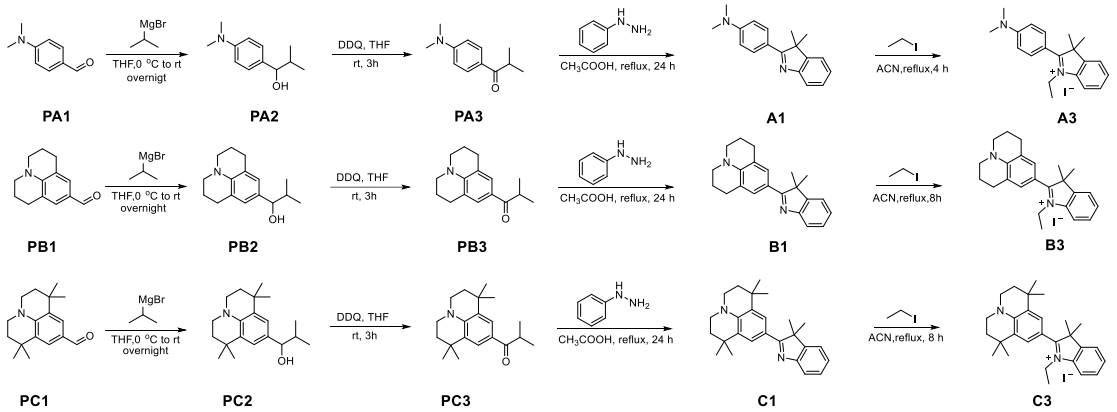

*Scheme S2. Synthesis of **A1**, **B1**, **C1**, **A3**, **B3**, **C3,** and the corresponding intermediates.*

General Procedure 1: **Preparation of PA2, PB2, and PC2**. The following procedure for **PA2** is representative. In a dried flask flushed with nitrogen, **PA1** (500 mg, 3.35 mmol, 1 eq.) was dissolved in anhydrous THF (15 mL). The solution was cooled to 0 °C. A solution of 1 M Isopropylmagnesium bromide in THF (5.0 mL,5.0 mmol, 1.5 eq.) was slowly added dropwise. After the addition, the mixture was stirred at room temperature overnight. The reaction was quenched by adding saturated NH_4Cl aq. and extracted with EA. The combined extracts were dried over Na_2SO_4, filtered, and evaporated. The residue was purified by flash column chromatography (silica gel, PE/EA = 20/1 to 5/1) to afford **PA2** (537 mg, 82.9% yield) as a light yellow liquid.

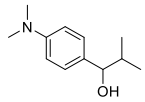

1-(4-(dimethylamino)phenyl)-2-methylpropan-1-ol(PA2): Light yellow liquid (537 mg, 82.9% yield).^{1}H NMR (400 MHz, $CDCl_3$) δ 7.11 (d, J = 8.5 Hz, 2H), 6.65 (d, J = 8.4 Hz, 2H), 4.16 (d, J = 7.3 Hz, 1H), 2.87 (s, 6H), 1.86 (dq, J = 13.6, 6.8 Hz, 1H), 1.67 (s, 1H), 0.95 (d, J = 6.6 Hz, 3H), 0.69 (d, J = 6.8 Hz, 3H).

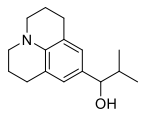

2-methyl-1-(2,3,6,7-tetrahydro-1H,5H-pyrido[3,2,1-ij]quinolin-9-yl)propan-1-ol(PB2): Light yellow solid (451 mg, 74% yield). ^{1}H NMR (400 MHz, $CDCl_3$) δ 6.64 (s, 2H), 4.02 (d, J = 7.5 Hz, 1H), 3.06 – 3.01 (m, 4H), 2.67 (t, J = 6.5 Hz, 4H), 1.93 – 1.86 (m, 4H), 1.82 (dd, J = 13.7, 6.8 Hz, 1H), 1.59 (s, 1H), 0.95 (d, J = 6.6 Hz, 3H), 0.70 (d, J = 6.8 Hz, 3H); ^{13}C NMR (101 MHz, CDCl3) δ 142.36, 131.01, 125.34, 121.28, 80.39, 50.06, 34.92, 27.72, 22.16, 19.36, 18.87; HRMS (ESI) m/z Found 246.1831 $(M+H)^+$, calculated 246.1852 for $C_{16}H_{24}NO$.

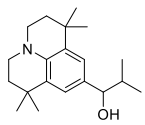

2-methyl-1-(1,1,7,7-tetramethyl-2,3,6,7-tetrahydro-1H,5H-pyrido[3,2,1-ij]quinolin-9-yl)propan-1-ol(PC2): Light yellow solid (415 mg, 70.8% yield). ^{1}H NMR (400 MHz, CDCl3) δ 6.96 (s, 2H), 4.18 (d, J = 6.4 Hz, 1H), 3.17 – 3.02 (m, 4H), 1.93 (dt, J = 13.7, 6.9 Hz, 1H), 1.82 – 1.71 (m, 4H), 1.65 (d, J = 2.2 Hz, 1H), 1.28 (d, J = 2.4 Hz, 12H), 1.02 (d, J = 6.6 Hz, 3H), 0.76 (d, J = 6.7 Hz, 3H); ^{13}C NMR (101 MHz, $CDCl_3$) δ 140.30, 130.65, 130.42, 122.75, 80.84, 47.09, 37.31, 35.20, 32.54, 31.86, 19.23, 18.97; HRMS (ESI) m/z Found 302.2457 $(M+H)^+$, calculated 302.2478 for $C_{20}H_{32}NO$.

General Procedure 2: **Preparation of PA3, PB3, and PC3.** The following procedure for **PA3** is representative. In a dried flask, **PA2**(300 mg 1.55 mmol) was dissolved in anhydrous THF (15 mL), then DDQ (420 mg, 1.86 mmol, 1.2 eq.) was added slowly in several portions. The resultant mixture was stirred at room temperature for 3 h. After the mixture was washed with saturated $NaHCO_3$ and extracted with EA, the combined organic layer was dried over Na_2SO_4, filtered, and evaporated. The residue was purified by flash column chromatography (silica gel, PE/EA = 10/1) to afford **PA3** (250 mg, 84% yield) as a white solid.

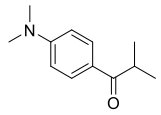

1-(4-(dimethylamino)phenyl)-2-methylpropan-1-one (PA3): White solid (250 mg, 84% yield).^{1}H NMR (400 MHz, $CDCl_3$) δ 7.81 (d, J = 8.6 Hz, 2H), 6.58 (d, J = 8.6 Hz, 2H), 3.42 (dt, J = 13.4, 6.7 Hz, 1H), 2.96 (s, 6H), 1.12 (s, 3H), 1.10 (s, 3H).

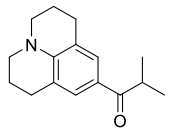

2-methyl-1-(2,3,6,7-tetrahydro-1H,5H-pyrido[3,2,1-ij]quinolin-9-yl)propan-1-one (PB3) : White solid (237 mg 79.6% yield).^{1}H NMR (400 MHz, $CDCl_3$) δ 7.38 (s, 2H), 3.40 (dt, J = 13.6, 6.8 Hz, 1H), 3.24 – 3.08 (m, 4H), 2.68 (t, J = 6.3 Hz, 4H), 1.96 – 1.80 (m, 4H), 1.09 (d, J = 6.8 Hz, 6H).

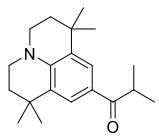

2-methyl-1-(1,1,7,7-tetramethyl-2,3,6,7-tetrahydro-1H,5H-pyrido[3,2,1-ij]quinolin-9-yl)propan-1-one (PC3): White solid (230 mg 77% yield).^{1}H NMR (400 MHz, CDCl3) δ 7.66 (s, 2H), 3.43 (dt, J = 13.6, 6.8 Hz, 1H), 3.26 – 3.11 (m, 4H), 1.73 – 1.57 (m, 4H), 1.22 (s, 12H), 1.11 (d, J = 6.8 Hz, 6H).

General Procedure 3: **Preparation of A1, B1, and C1.** The following procedure for **A1** is representative. A solution of **PA3** (100 mg, 0.52 mmol,1 eq) and phenylhydrazine (68 mg, 0.63 mmol, 1.2 eq) in CH_3COOH (10 mL) was heated under reflux for 24 h. After cooling to ambient temperature, the solution was diluted with H_2O (20 mL) and the pH was adjusted to ~8 with aqueous KOH (0.3 M). Then the mixture was extracted with CH_2Cl_2 (3 × 15 mL). The organic phase was dried over Na_2SO_4, filtered and the solvent was evaporated to dryness. The residue was purified by column chromatography (silica gel, PE/EA = 10/1) to afford **A1** (69 mg, 50% yield) as a yellow solid.

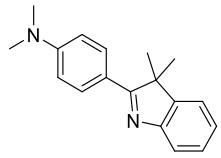

4-(3,3-dimethyl-3H-indol-2-yl)-N,N-dimethylaniline (A1):yellow solid (69 mg, 50% yield). ^{1}H NMR (400 MHz, $CDCl_3$) δ 8.03 (d, J = 8.5 Hz, 2H), 7.54 (d, J = 7.6 Hz, 1H), 7.28 – 7.19 (m, 2H), 7.12 (t, J = 7.3 Hz, 1H), 6.67 (d, J = 8.5 Hz, 2H), 2.97 (s, 6H), 1.52 (s, 6H).

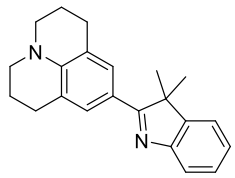

9-(3,3-dimethyl-3H-indol-2-yl)-2,3,6,7-tetrahydro-1H,5H-pyrido[3,2,1-ij]quinoline (B1): yellow solid (87 mg, 67% yield).^{1}H NMR (400 MHz, $CDCl_3$) δ 7.67 (s, 2H), 7.60 (d, J = 7.6 Hz, 1H), 7.30 (dd, J = 11.2, 7.4 Hz, 2H), 7.17 (t, J = 7.3 Hz, 1H), 3.25 (t, J = 5.4 Hz, 4H), 2.82 (t, J = 6.1 Hz, 4H), 2.06 – 1.89 (m, 4H), 1.58 (s, 6H); ^{13}C NMR (101 MHz, $CDCl_3$) δ 183.15, 153.76, 147.57, 144.99, 127.61, 127.52, 124.32, 120.65, 120.55, 119.63, 119.46, 52.81, 49.93, 27.88, 25.65, 21.70; HRMS (ESI) m/z Found 317.1985 $(M+H)^+$, calculated 317.2012 for $C_{22}H_{25}N_2$.

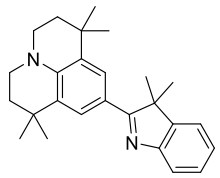

9-(3,3-dimethyl-3H-indol-2-yl)-1,1,7,7-tetramethyl-2,3,6,7-tetrahydro-1H,5H-pyrido[3,2,1-ij]quinoline (C1): yellow solid (50 mg, 40% yield). ^{1}H NMR (400 MHz, CDCl3) δ 7.94 (s, 2H), 7.61 (d, J = 7.5 Hz, 1H), 7.33 – 7.27 (m, 2H), 7.16 (t, J = 7.3 Hz, 1H), 3.35 – 3.21 (m, 4H), 1.81 – 1.74 (m, 4H), 1.59 (s, 6H), 1.37 (s, 12H); HRMS (ESI) m/z Found 373.2633 $(M+H)^+$, calculated 373.2638 for $C_{26}H_{33}N_2$.

General Procedure 4: **Preparation of A3, B3, and C3.** The following procedure for **A3** is representative. In a sealed tube, a solution of **A1** (30 mg, 0.11 mmol, 1 eq) and CH_3CH_2I (86 µL, 1.1 mmol, 10 eq) in MeCN (3 mL) was refluxed for 4 h. After cooling the mixture to the ambient temperature, the solvent was evaporated under reduced pressure. The residue was purified by column chromatography (silica gel, DCM/MeOH = 15/1) to afford **A3** (15 mg, 31.4% yield) as a yellow solid.

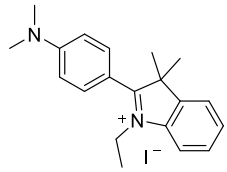

2-(4-(dimethylamino)phenyl)-1-ethyl-3,3-dimethyl-3H-indol-1-ium (A3): Orange solid (15 mg ,31.4% yield). ^{1}H NMR (400 MHz, MeOD) δ 7.88 (d, J = 9.1 Hz, 2H), 7.84 (d, J = 7.6 Hz, 1H), 7.76 (d, J = 7.1 Hz, 1H), 7.69 – 7.55 (m, 2H), 7.06 (d, J = 9.1 Hz, 2H), 4.59 (q, J = 7.2 Hz, 2H), 3.23 (s, 6H), 1.76 (s, 6H), 1.72 (t, J = 7.3 Hz, 3H).

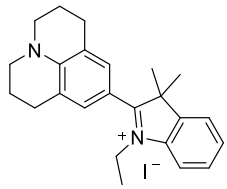

1-ethyl-3,3-dimethyl-2-(2,3,6,7-tetrahydro-1H,5H-pyrido[3,2,1-ij]quinolin-9-yl)-3H-indol-1-ium (B3): Orange solid (28 mg, 62.5% yield).^{1}H NMR (400 MHz, $CDCl_3$)

δ 7.69 (d, J = 8.0 Hz, 1H), 7.54 (t, J = 7.5 Hz, 1H), 7.47 (q, J = 7.7 Hz, 2H), 7.40 (s, 2H), 4.77 (q, J = 7.1 Hz, 2H), 3.47 (t, J = 5.7 Hz, 4H), 2.87 (t, J = 6.1 Hz, 4H), 2.11 – 1.98 (m, 4H), 1.76 – 1.68 (m, 9H); HRMS (ESI) m/z Found 345.2306 M^+, calculated 345.2325 for $C_{24}H_{29}N_2$.

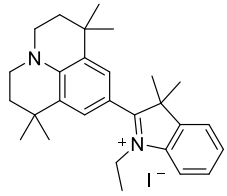

1-ethyl-3,3-dimethyl-2-(1,1,7,7-tetramethyl-2,3,6,7-tetrahydro-1H,5H-pyrido[3,2,1-ij]quinolin-9-yl)-3H-indol-1-ium (C3): Orange solid (21 mg, 49% yield). ^{1}H NMR (400 MHz, MeOD) δ 7.76 – 7.68 (m, 4H), 7.61 (t, J = 7.7 Hz, 1H), 7.55 (t, J = 7.4 Hz, 1H), 4.54 (q, J = 7.3 Hz, 2H), 3.57 (t, J = 6.1 Hz, 4H), 1.89 – 1.84 (m, 4H), 1.82 – 1.75 (m, 9H), 1.39 (s, 12H); HRMS (ESI) m/z Found 401.2943 M^+, calculated 401.2951 for $C_{28}H_{37}N_2$.

3.3 Synthesis of A4, B4, and C4

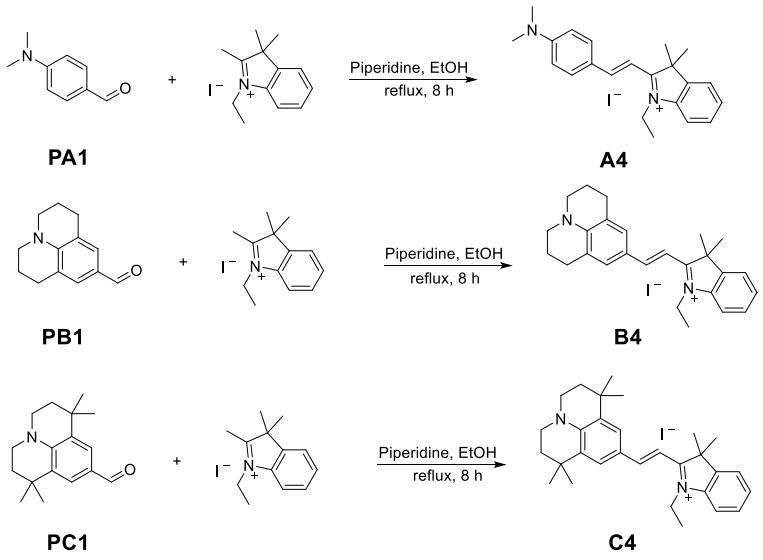

*Scheme S3. Synthesis of **A4, B4,** and **C4.***

General Procedure 5: **Preparation of A4, B4, and C4**. The following procedure for **A4** is representative. Compound **PA1** (30 mg, 0.20 mmol, 1 eq), Indole salt (70 mg,

0.22 mmol,1.1 eq), and piperidine (catalyst, 5 drops) were dissolved in pure ethanol (10 mL). The mixture was refluxed for 8 h under an inert nitrogen environment. After cooling to room temperature, the solvent was evaporated under reduced pressure. The residue was purified by column chromatography (silica gel, DCM/MeOH = 20/1) to afford **A4** (45 mg, 50% yield) as a red solid.

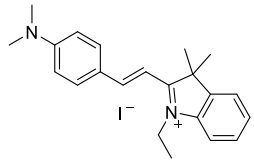

(E)-2-(4-(dimethylamino)styryl)-1-ethyl-3,3-dimethyl-3H-indol-1-ium (A4): Red solid (45 mg, 50% yield).^{1}H NMR (400 MHz, MeOD) δ 8.32 (d, J = 15.5 Hz, 1H), 7.96 (d, J = 8.8 Hz, 2H), 7.67 (d, J = 7.3 Hz, 1H), 7.62 (d, J = 7.9 Hz, 1H), 7.55 (td, J = 7.7, 1.2 Hz, 1H), 7.52 – 7.46 (m, 1H), 7.20 (d, J = 15.5 Hz, 1H), 6.91 (d, J = 9.2 Hz, 2H), 4.51 (q, J = 7.3 Hz, 2H), 3.22 (s, 6H), 1.80 (s, 6H), 1.51 (t, J = 7.3 Hz, 3H).

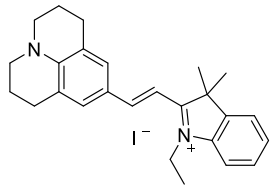

(E)-1-ethyl-3,3-dimethyl-2-(2-(2,3,6,7-tetrahydro-1H,5H-pyrido[3,2,1-ij]quinolin-9-yl)vinyl)-3H-indol-1-ium (B4): Purple solid (33 mg, 44.4% yield).^{1}H NMR (400 MHz, MeOD) δ 8.14 (d, J = 15.2 Hz, 1H), 7.67 – 7.46 (m, 5H), 7.45 – 7.35 (m, 1H), 7.03 (d, J = 15.2 Hz, 1H), 4.42 (q, J = 7.2 Hz, 2H), 3.52 – 3.45 (m, 4H), 2.92 – 2.74 (m, 4H), 2.07 – 1.92 (m,4H), 1.76 (s, 6H), 1.47 (t, J = 7.2 Hz, 3H).

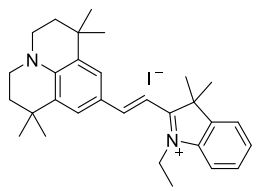

(E)-1-ethyl-3,3-dimethyl-2-(2-(1,1,7,7-tetramethyl-2,3,6,7-tetrahydro-1H,5H-pyrido[3,2,1-ij]quinolin-9-yl)vinyl)-3H-indol-1-ium (C4): Purple solid (30 mg, 46%

yield).^{1}H NMR (400 MHz, MeOD) δ 8.24 (d, J = 15.2 Hz, 1H), 7.76 (s, 2H), 7.61 (d, J = 7.4 Hz, 1H), 7.57 – 7.47 (m, 2H), 7.46 – 7.37 (m, 1H), 7.04 (d, J = 15.2 Hz, 1H), 4.47 (q, J = 7.2 Hz, 2H), 3.55 (t, J = 6.2 Hz, 4H), 1.86 – 1.80 (m, 4H), 1.79 (s, 6H), 1.49 (t, J = 7.2 Hz, 3H), 1.37 (s, 12H); HRMS (ESI) m/z Found 427.3085 M^{+}, calculated 427.3108 for $C_{30}H_{39}N_2$.

3.4 Synthesis of A5, B5, C5, and the corresponding intermediates

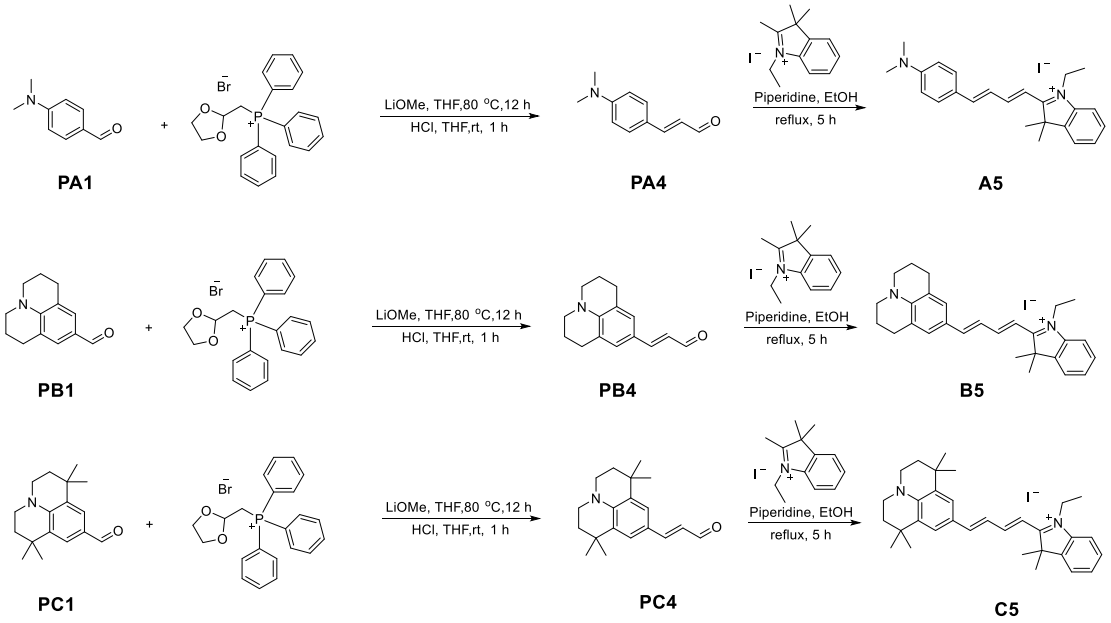

*Scheme S4. Synthesis of **A5**, **B5**, **C5,** and the corresponding intermediates.*

General Procedure 6: **Preparation of PA4, PB4, and PC4.** The following procedure for **PA4** is representative. LiOMe (56 mg, 1.48 mmol, 2.2 eq) and **PA1** (100 mg, 0.67 mmol, 1 eq) were added to a solution of (1,3-dioxolane-2-ylmethyl) triphenylphosphonium bromide (316 mg, 0.74 mmol, 1.1 eq) in THF (20 mL). The resulting mixture was stirred at 78 °C for 12 h. After cooling to room temperature, the reaction mixture was treated with saturated aqueous NH_4Cl solution and extracted with CH_2Cl_2. The combined organic layers were dried over Na_2SO_4, filtered, and concentrated under reduced pressure. The crude product was dissolved in THF (10 mL), adding 10% HCl, and stirred at room temperature for 1 h. The mixture was then

neutralized by 2N NaOH solution and extracted with CH_2Cl_2. The combined organic layers were dried over Na_2SO_4, filtered, and concentrated under reduced pressure. The residue was purified by column chromatography on silica gel (PE/DCM = 5/1) to give **PA4** (95 mg, 80.9% yield) as a yellow powder.

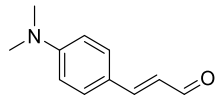

(E)-3-(4-(dimethylamino)phenyl)acrylaldehyde (PA4): Orange solid (95 mg, 80.9% yield).^{1}H NMR (700 MHz, $CDCl_3$) δ 9.52 (d, J = 7.9 Hz, 1H), 7.39 (d, J = 8.8 Hz, 2H), 7.31 (d, J = 15.6 Hz, 1H), 6.63 (d, J = 8.7 Hz, 2H), 6.48 (dd, J = 15.6, 7.9 Hz, 1H), 2.98 (s, 6H).

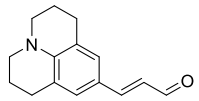

(E)-3-(2,3,6,7-tetrahydro-1H,5H-pyrido[3,2,1-ij]quinolin-9-yl)acrylaldehyde (PB4): Orange solid (79 mg, 70%).^{1}H NMR (400 MHz, $CDCl_3$) δ 9.54 (d, J = 8.0 Hz, 1H), 7.27 (d, J = 15.5 Hz, 1H), 7.01 (s, 2H), 6.47 (dd, J = 15.5, 8.0 Hz, 1H), 3.29 – 3.22 (m, 4H), 2.74 (t, J = 6.3 Hz, 4H), 1.96 (td, J = 11.6, 6.1 Hz, 4H).

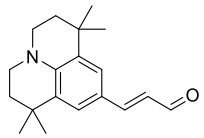

(E)-3-(1,1,7,7-tetramethyl-2,3,6,7-tetrahydro-1H,5H-pyrido[3,2,1-ij]quinolin-9-yl)acrylaldehyde (PC4): Orange solid (56 mg, 51%).^{1}H NMR (400 MHz, CDCl3) δ 9.56 (d, J = 8.0 Hz, 1H), 7.34 (d, J = 15.5 Hz, 1H), 7.26 (s, 2H), 6.52 (dd, J = 15.5, 8.0 Hz, 1H), 3.32 – 3.21 (m, 4H), 1.76 – 1.62 (m, 4H), 1.29 (s, 12H).

General Procedure 7: **Preparation of A5 B5, and C5.** The following procedure for **A5** is representative. Compound **PA4** (50 mg, 0.29 mmol, 1 eq), indole salt (99 mg, 0.31 mmol, 1.1 eq) and piperidine (catalyst, 10 drops) were dissolved in ethanol (15

mL). The mixture was refluxed for 5 h under an inert nitrogen environment. After cooling to room temperature, the solvent was evaporated under reduced pressure. The residue was purified by column chromatography (silica gel, DCM/MeOH = 20/1) to give the product **A5** (32 mg, 23.7% yield) as a dark blue solid.

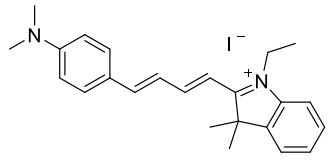

2-((1E,3E)-4-(4-(dimethylamino)phenyl)buta-1,3-dien-1-yl)-1-ethyl-3,3-dimethyl-3H-indol-1-ium (A5): Dark blue solid (32 mg, 23.7% yield).^{1}H NMR (400 MHz, MeOD) δ 8.30 (dd, J = 14.4, 11.6 Hz, 1H), 7.65 (dd, J = 13.9, 5.2 Hz, 5H), 7.56 (t, J = 7.4 Hz, 1H), 7.50 (t, J = 7.3 Hz, 1H), 7.31 (dd, J = 14.5, 11.5 Hz, 1H), 6.94 (d, J = 14.7 Hz, 1H), 6.82 (d, J = 8.7 Hz, 2H), 4.45 (q, J = 7.2 Hz, 2H), 3.13 (s, 6H), 1.77 (s, 6H), 1.50 (t, J = 7.2 Hz, 3H).

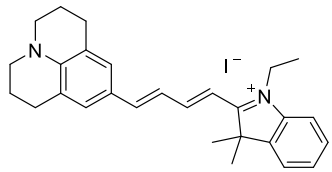

1-ethyl-3,3-dimethyl-2-((1E,3E)-4-(2,3,6,7-tetrahydro-1H,5H-pyrido[3,2,1-ij]quinolin-9-yl)buta-1,3-dien-1-yl)-3H-indol-1-ium (B5): Dark blue solid (30 mg 26% yield).^{1}H NMR (400 MHz, MeOD) δ 8.22 (dd, J = 14.2, 11.8 Hz, 1H), 7.61 (d, J = 7.5 Hz, 1H), 7.57 – 7.47 (m, 3H), 7.46 – 7.39 (m, 1H), 7.25 (s, 2H), 7.19 (dd, J = 14.0, 12.0 Hz, 1H), 6.72 (d, J = 14.4 Hz, 1H), 4.34 (q, J = 7.2 Hz, 2H), 3.42 (t, J = 5.7 Hz, 4H), 2.77 (t, J = 6.1 Hz, 4H), 2.02 – 1.92 (m, 4H), 1.74 (s, 6H), 1.46 (t, J = 7.2 Hz, 3H); HRMS (ESI) m/z Found 397.2631 M^{+}, calculated 397.2638 for $C_{28}H_{33}N_{2}$.

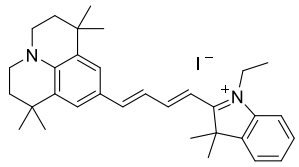

1-ethyl-3,3-dimethyl-2-((1E,3E)-4-(1,1,7,7-tetramethyl-2,3,6,7-tetrahydro-1H,5H-pyrido[3,2,1-ij]quinolin-9-yl)buta-1,3-dien-1-yl)-3H-indol-1-ium (C5): Dark blue solid (13 mg 12.7% yield). ^{1}H NMR (400 MHz, MeOD) δ 8.24 (dd, J = 14.2, 11.8 Hz, 1H), 7.62 (s, 1H), 7.60 (d, J = 5.1 Hz, 1H), 7.54 – 7.46 (m, 4H), 7.46 – 7.38 (m, 1H), 7.27 (dd, J = 14.2, 11.7 Hz, 1H), 6.80 (d, J = 14.4 Hz, 1H), 4.35 (q, J = 7.2 Hz, 2H), 3.48 (t, J = 6.1 Hz, 4H), 1.81 – 1.76 (m, 4H), 1.75 (s, 6H), 1.46 (t, J = 7.2 Hz, 3H), 1.33 (s, 12H); HRMS (ESI) m/z Found 453.3226 M^{+}, calculated 453.3264 for $C_{32}H_{41}N_2$.

3.5 ^{1}H-NMR, ^{13}C-NMR and HRMS spectra

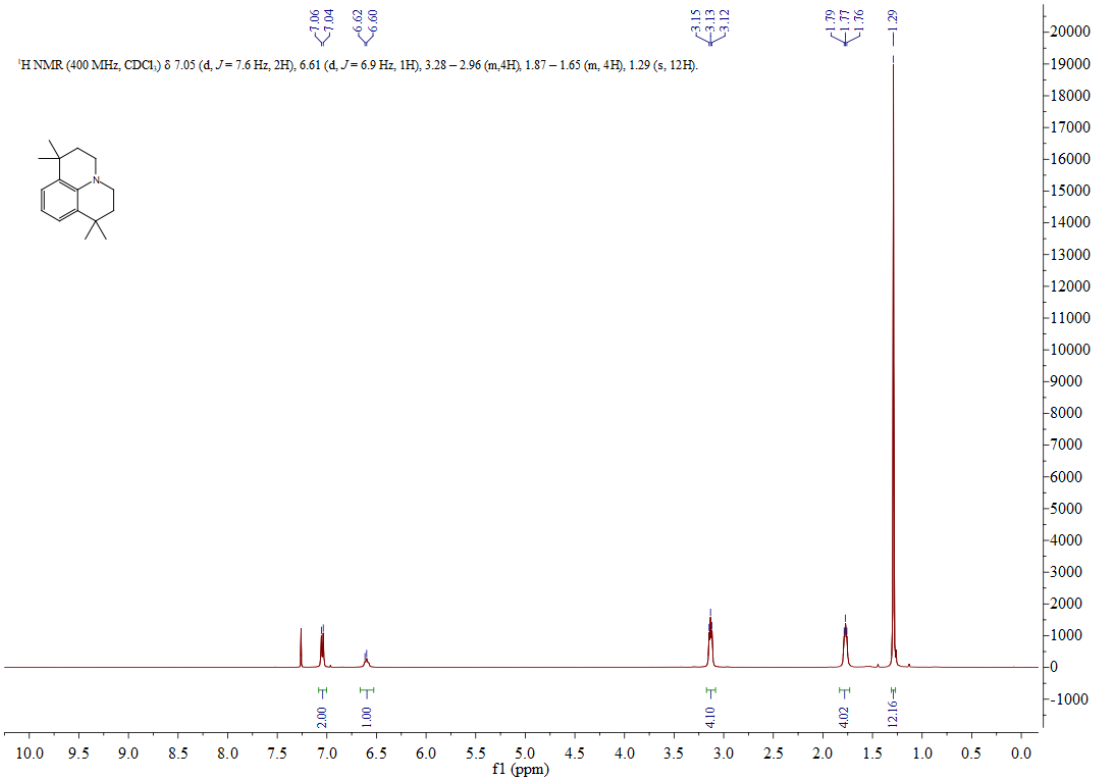

*Figure S15. ^{1}H-NMR spectra of **S1** in $CDCl_3$.*

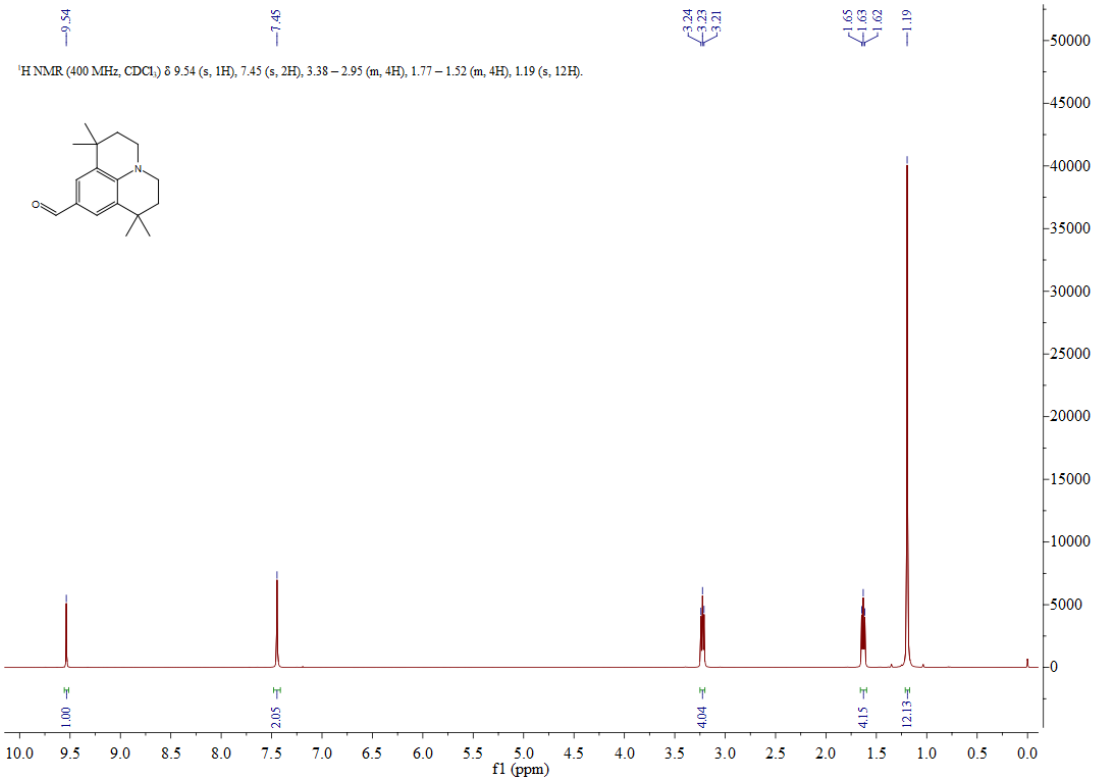

*Figure S16. ^{1}H-NMR spectrum of **PC1** in $CDCl_3$.*

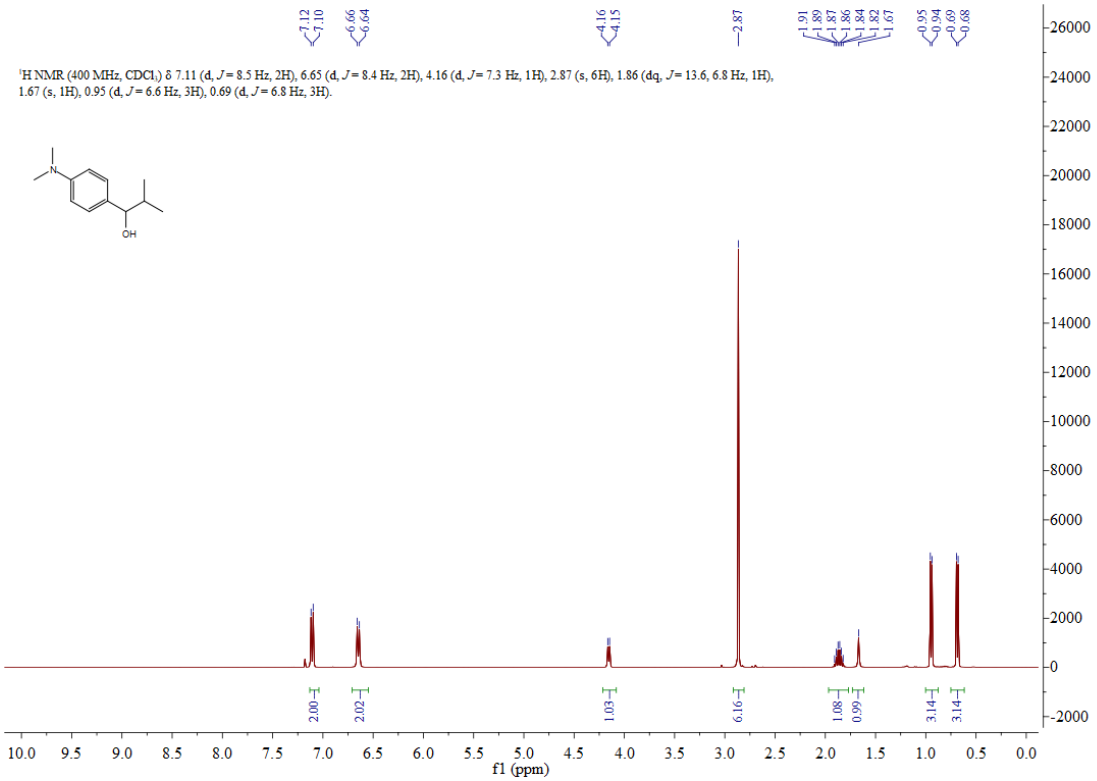

*Figure S17. ¹H-NMR spectrum of **PA2** in $CDCl_3$.*

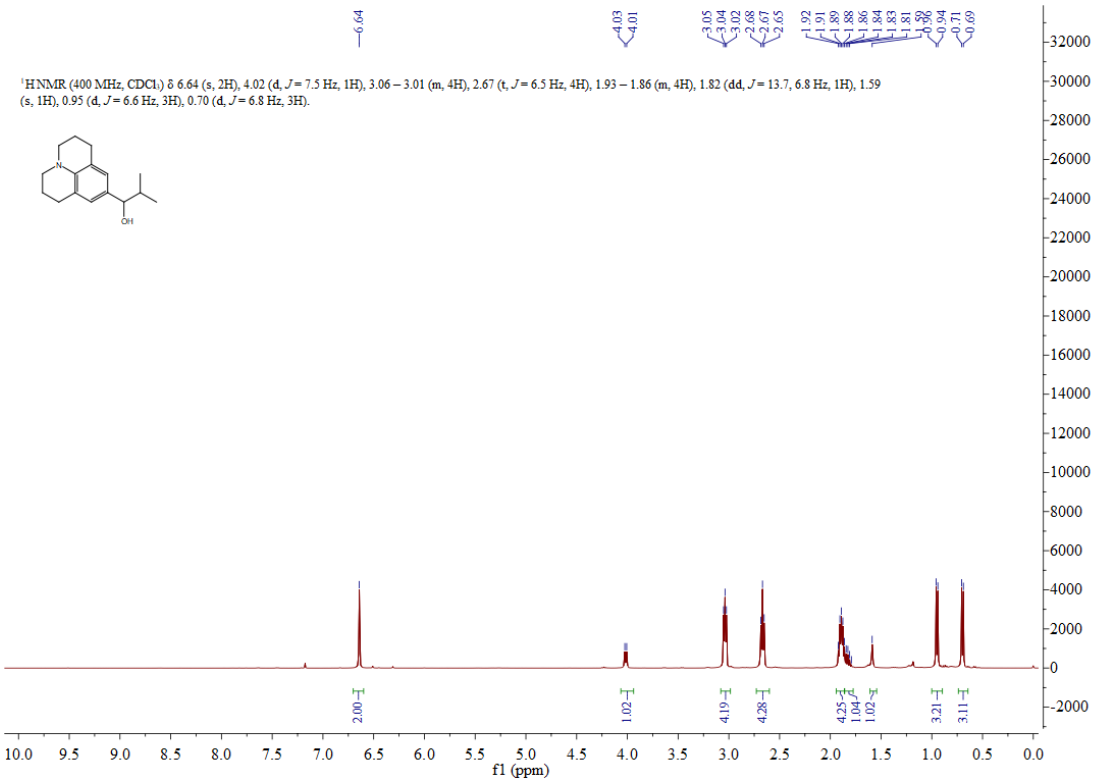

*Figure S18. ¹H-NMR spectrum of **PB2** in $CDCl_3$.*

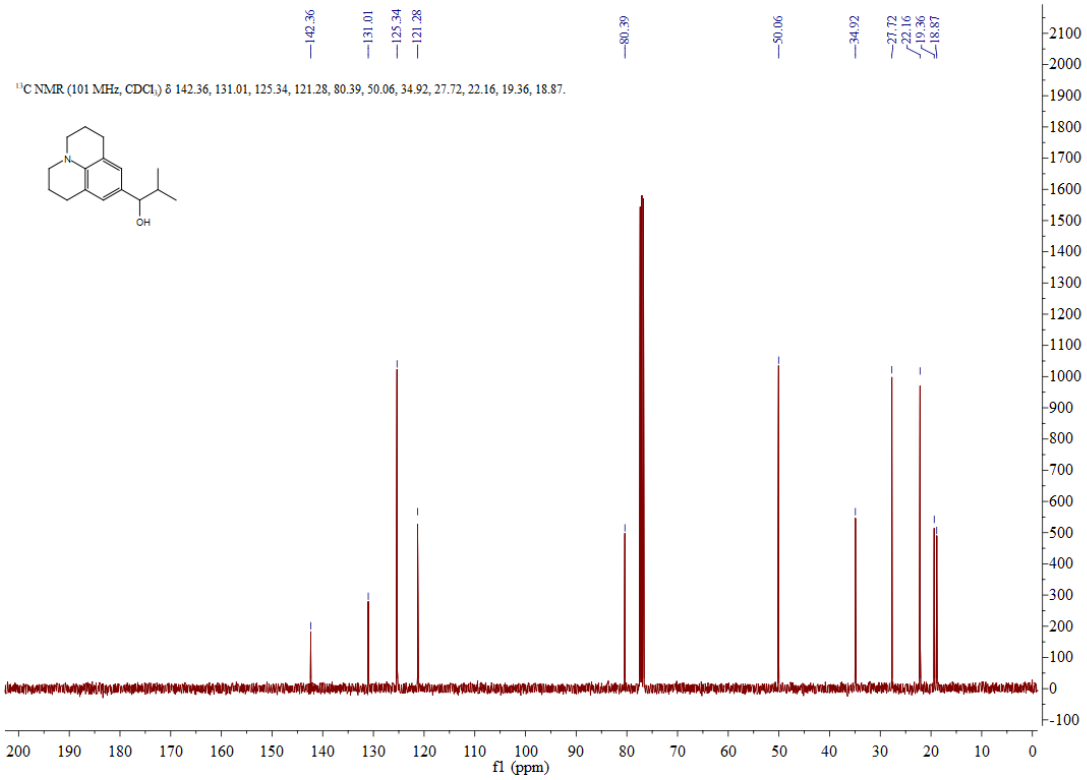

*Figure S19. ^{13}C-NMR spectrum of **PB2** in $CDCl_3$.*

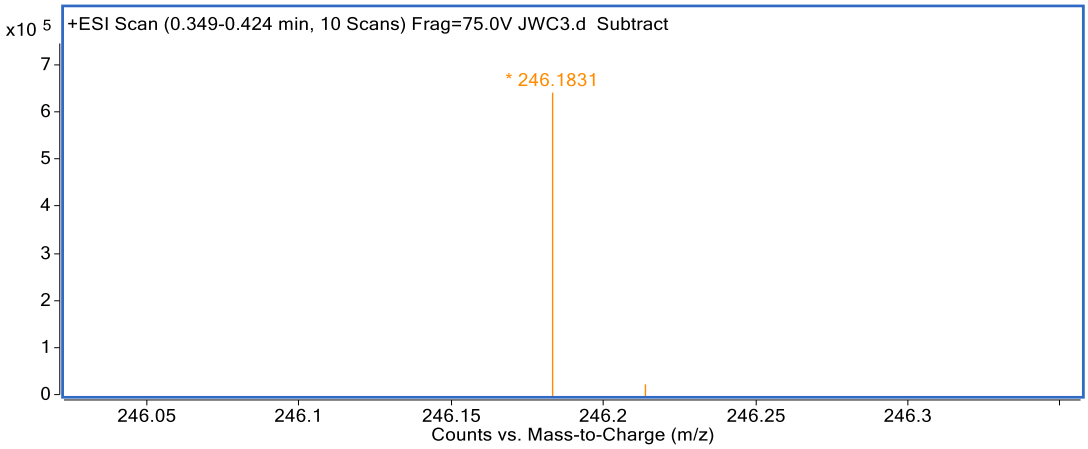

*Figure S20. HRMS spectrum of **PB2**.*

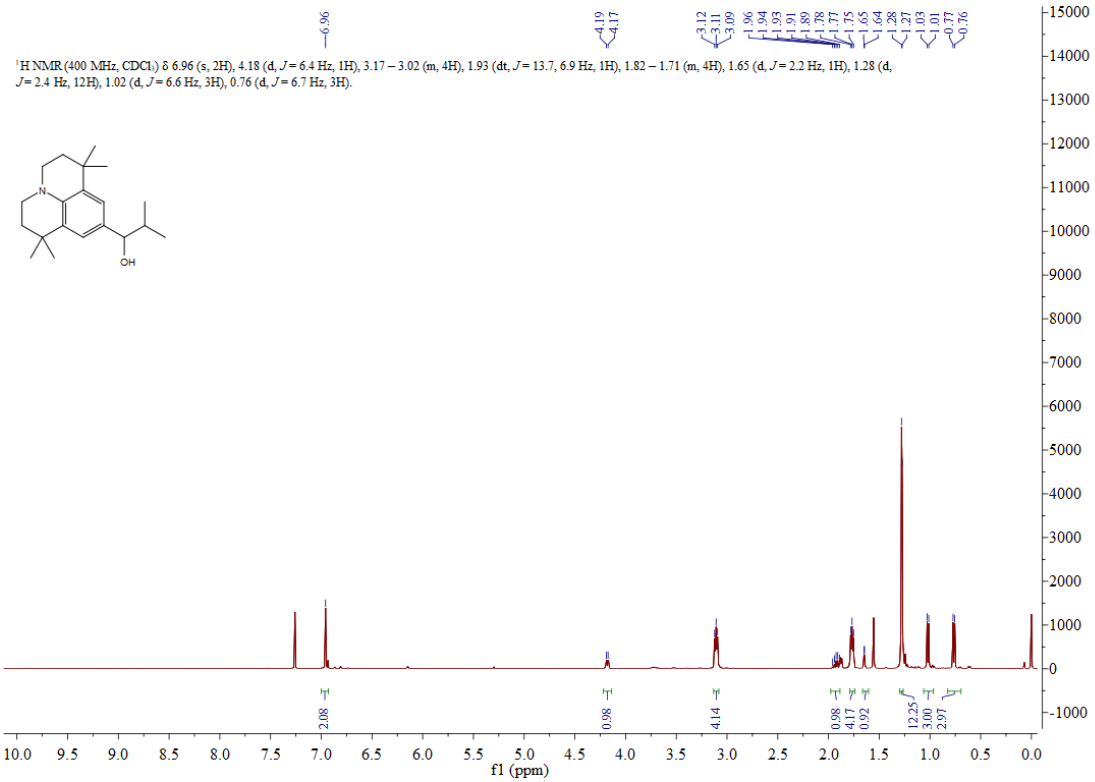

*Figure S21. ^{1}H-NMR spectrum of **PC2** in CDCl$_3$.*

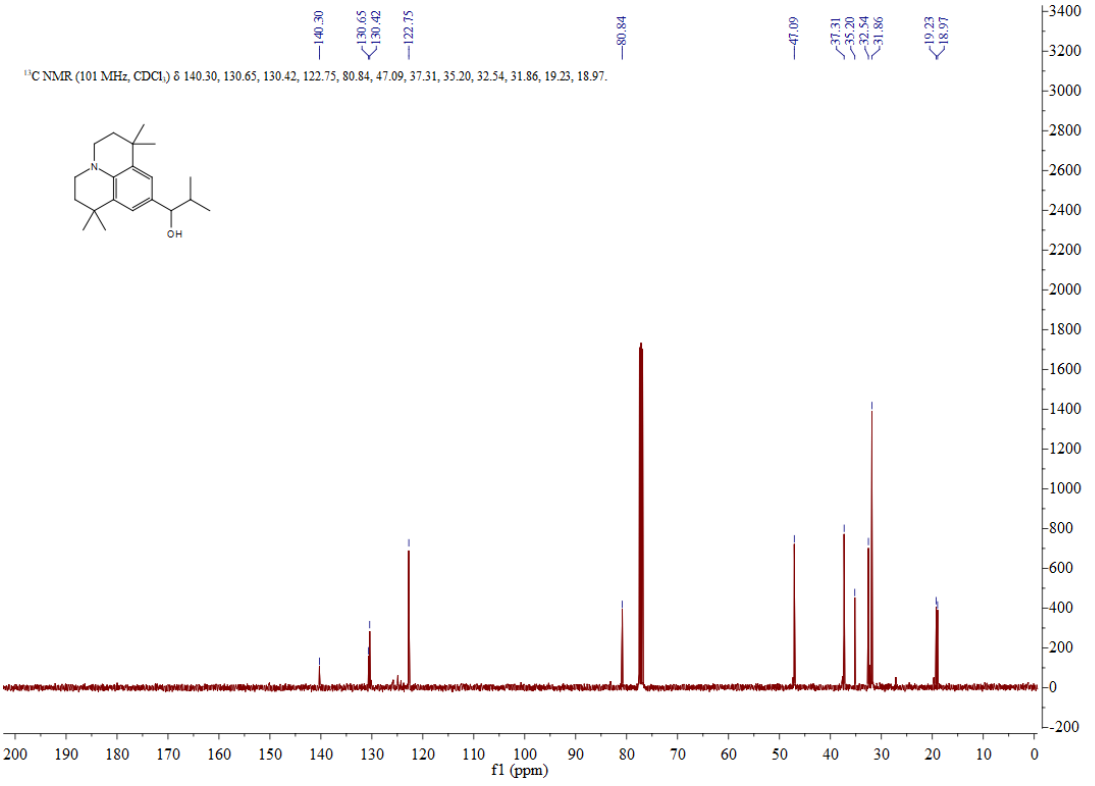

*Figure S22. ^{13}C-NMR spectrum of **PC2** in CDCl$_3$.*

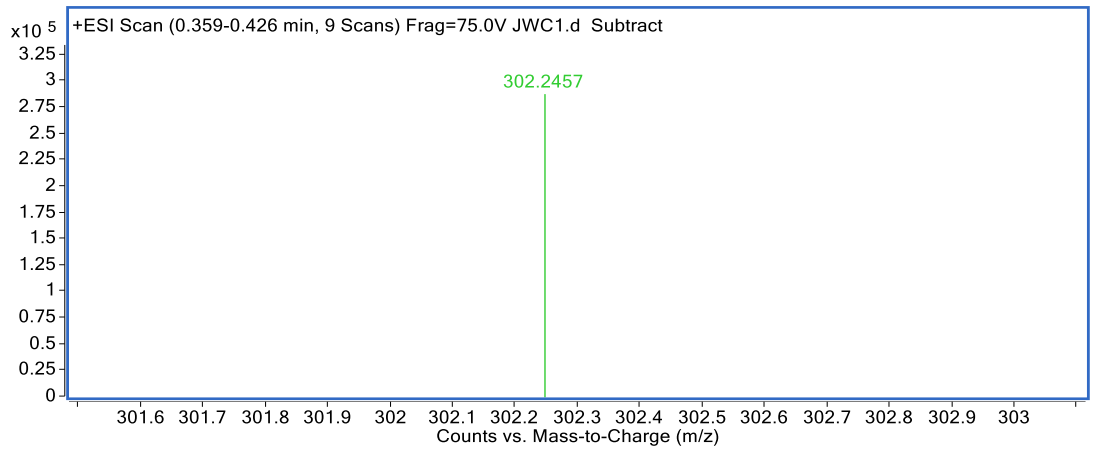

*Figure S23. HRMS spectrum of **PC2**.*

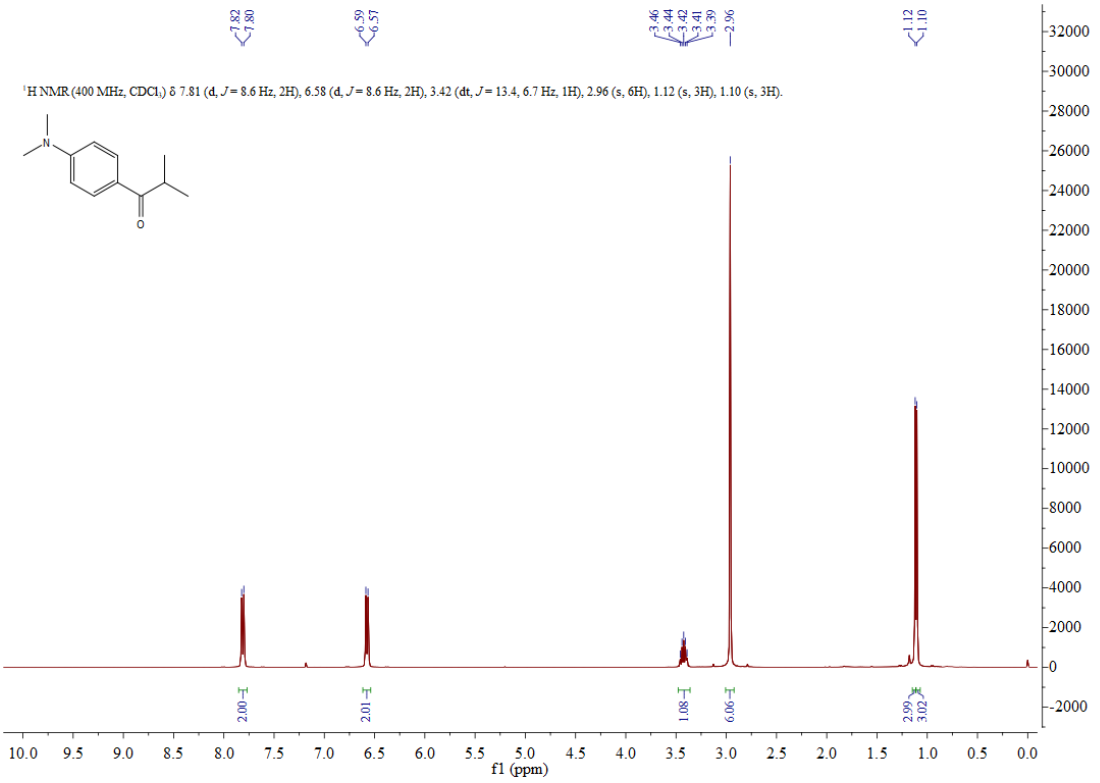

*Figure S24. ^{1}H-NMR spectrum of **PA3** in $CDCl_3$.*

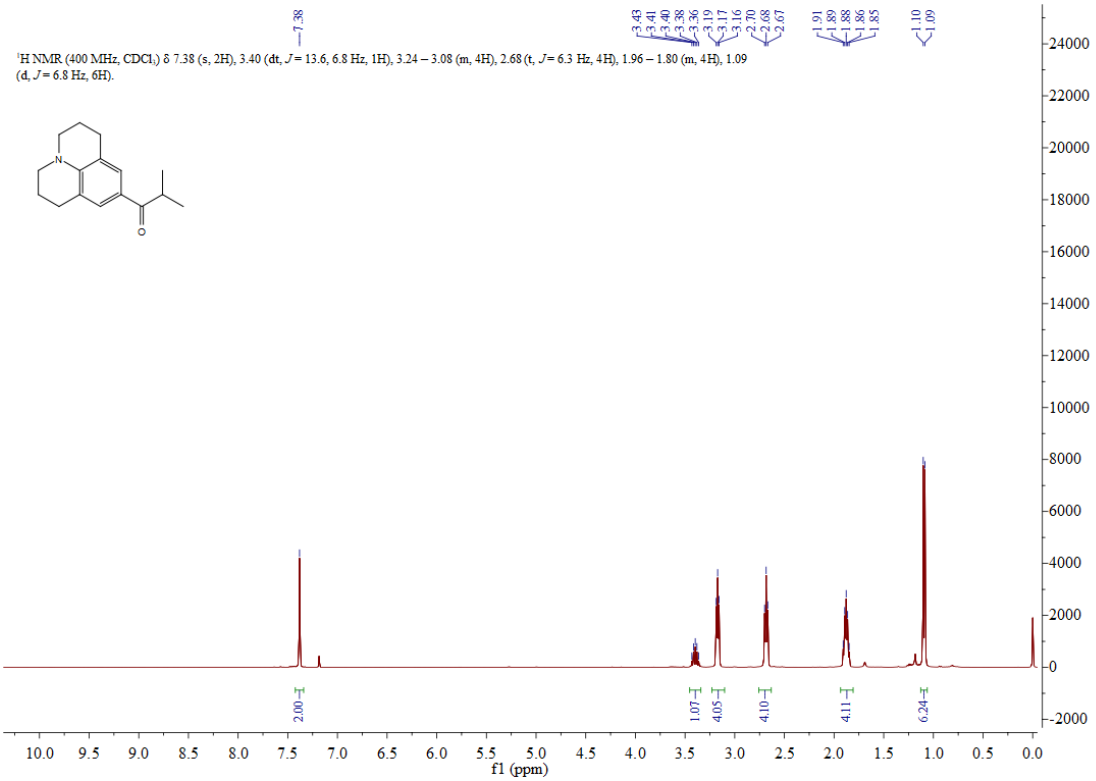

*Figure S25. ^{1}H-NMR spectrum of **PB3** in $CDCl_3$.*

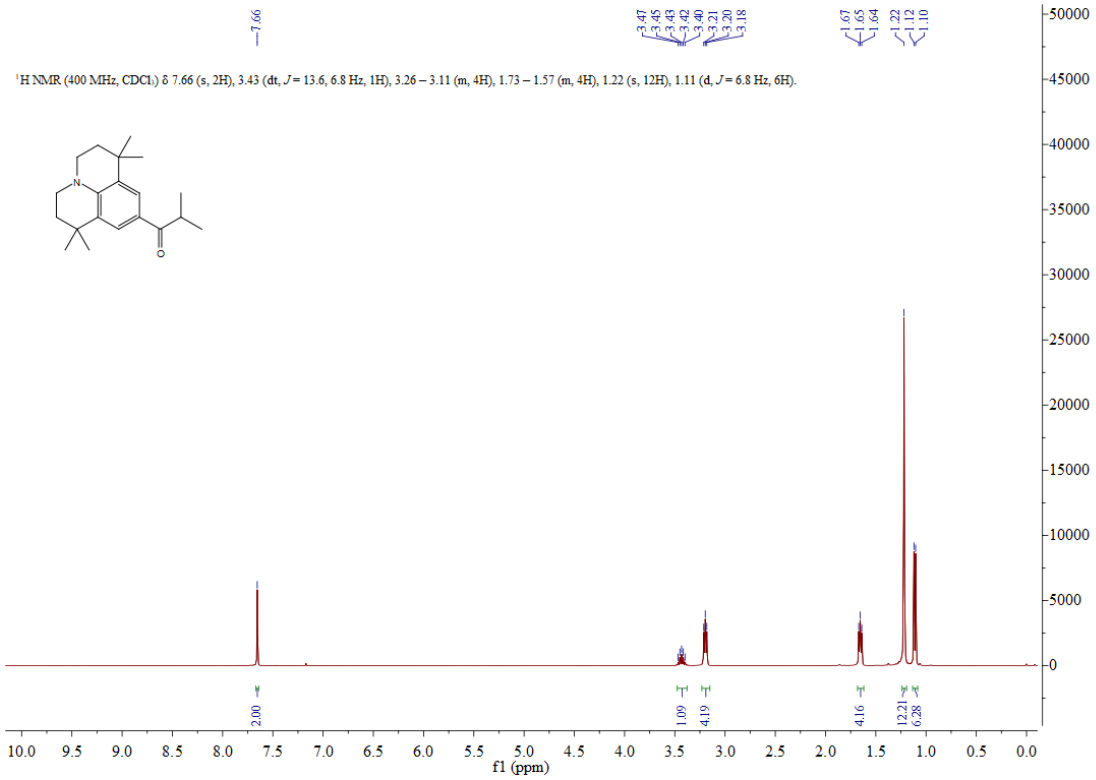

*Figure S26. ^{1}H-NMR spectrum of **PC3** in $CDCl_3$.*

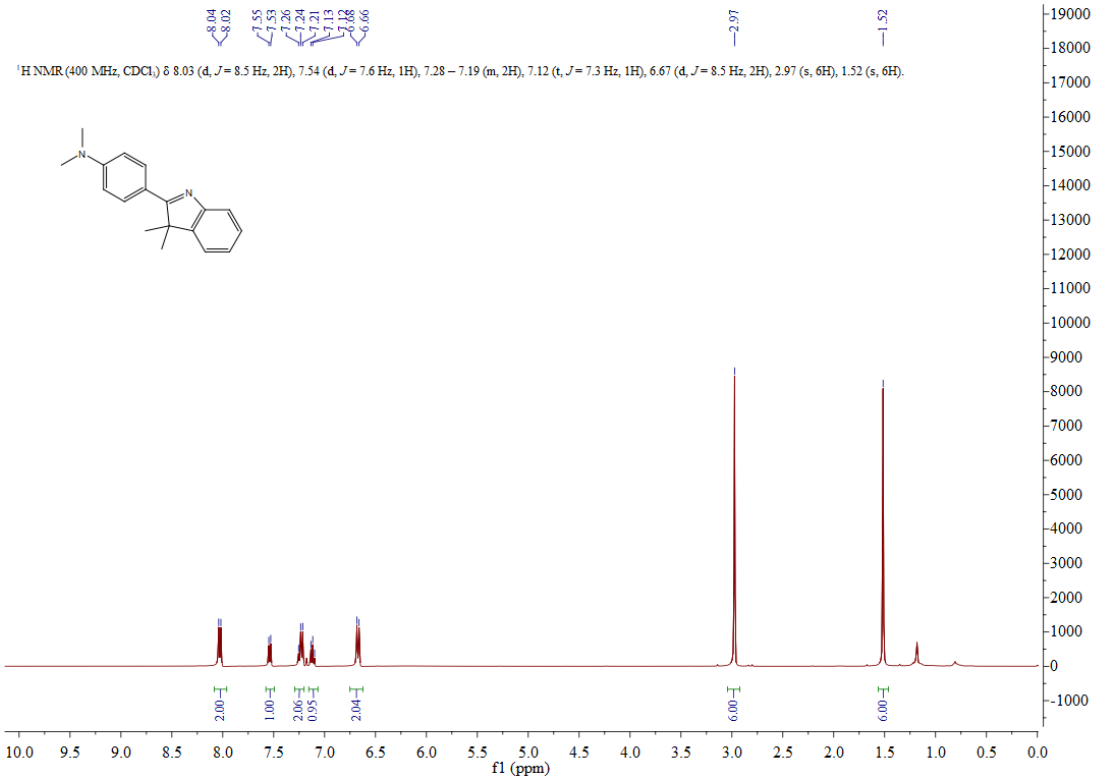

*Figure S27. ^{1}H-NMR spectrum of **A1** in $CDCl_3$.*

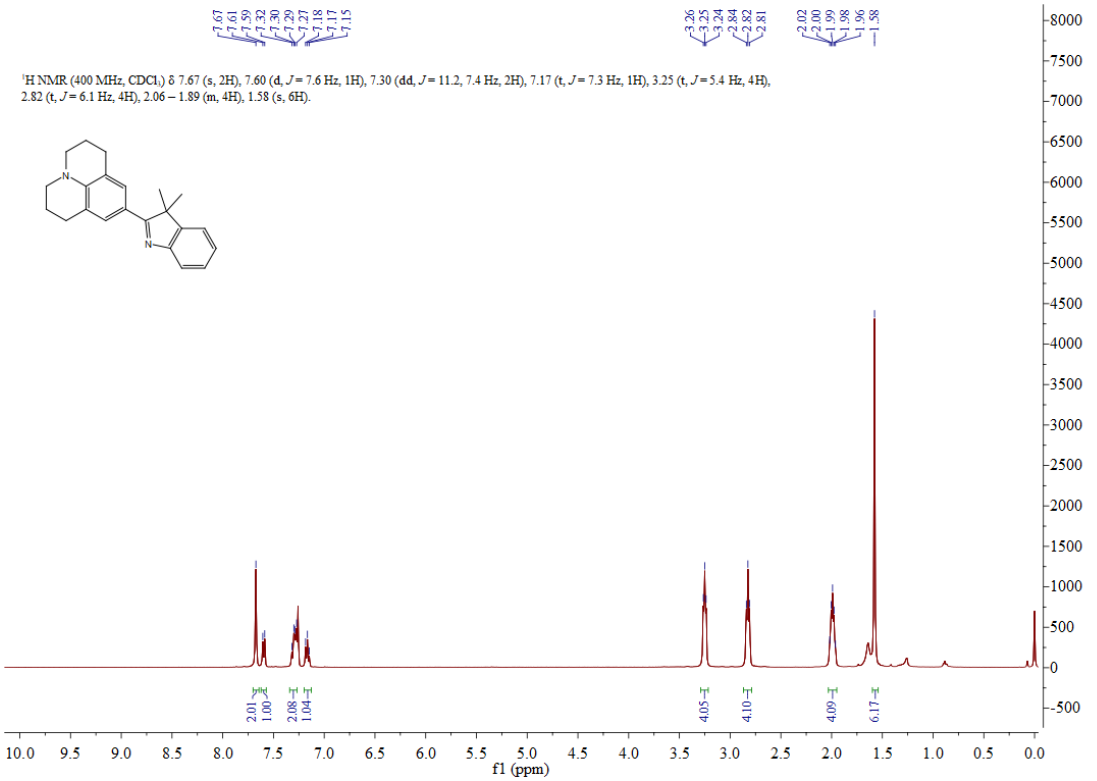

*Figure S28. ^{1}H-NMR spectrum of **B1** in $CDCl_3$.*

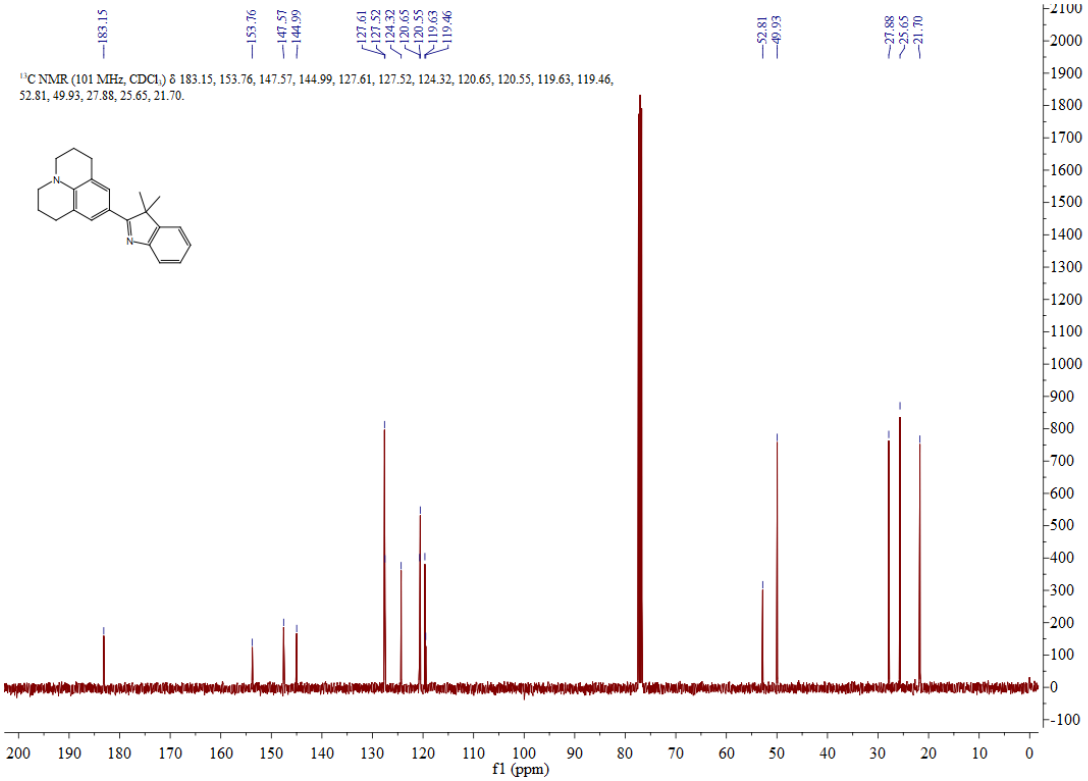

*Figure S29. ^{13}C-NMR spectrum of **B1** in $CDCl_3$.*

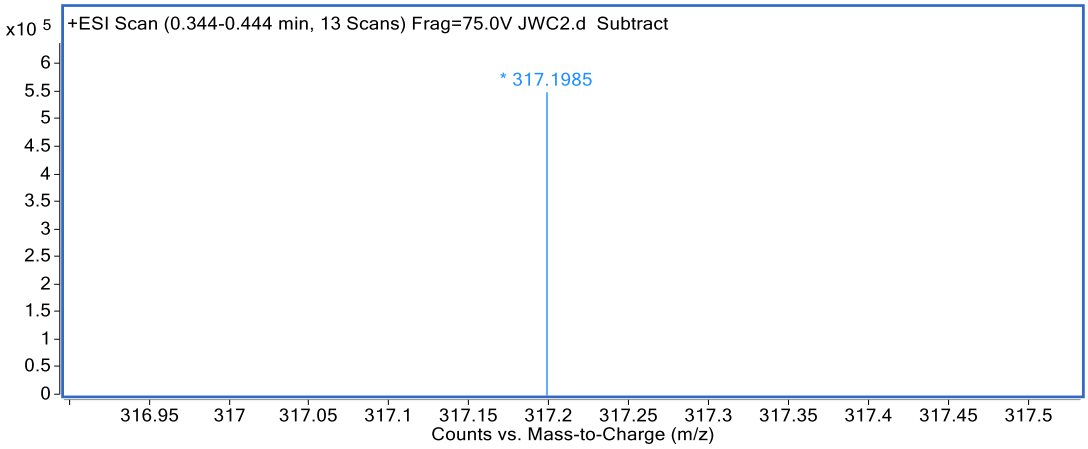

*Figure S30. HRMS spectrum of **B1**.*

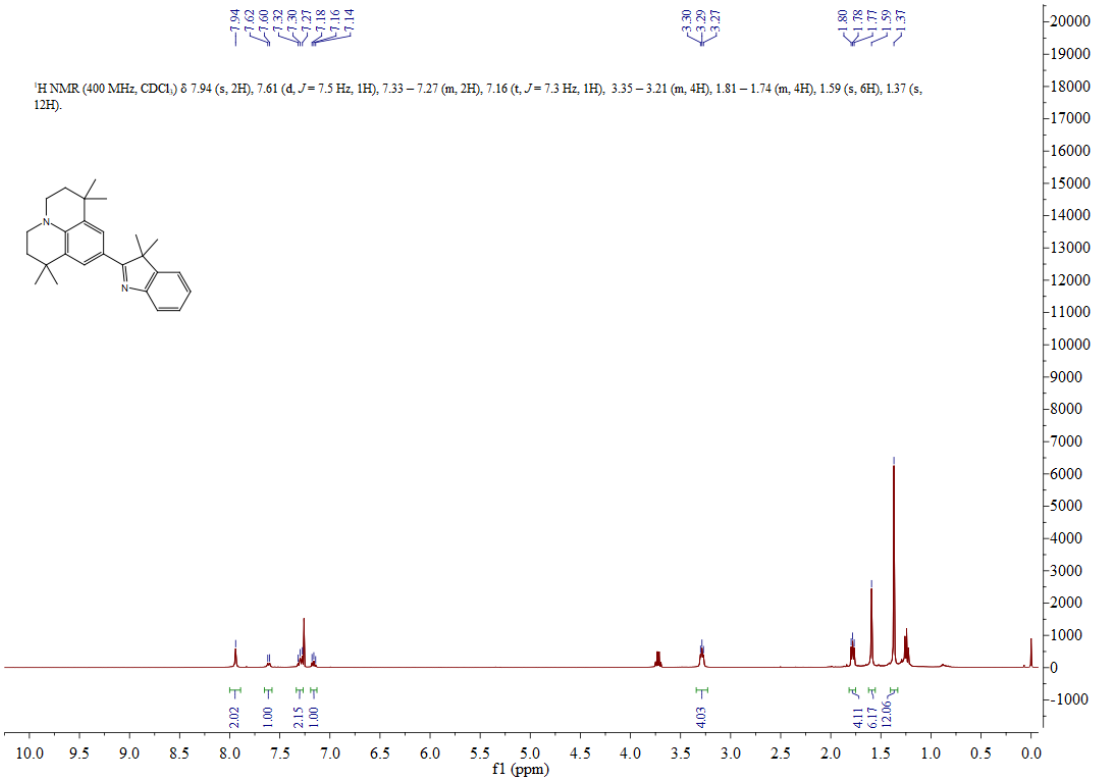

*Figure S31. [1]H-NMR spectrum of **C1** in $CDCl_3$.*

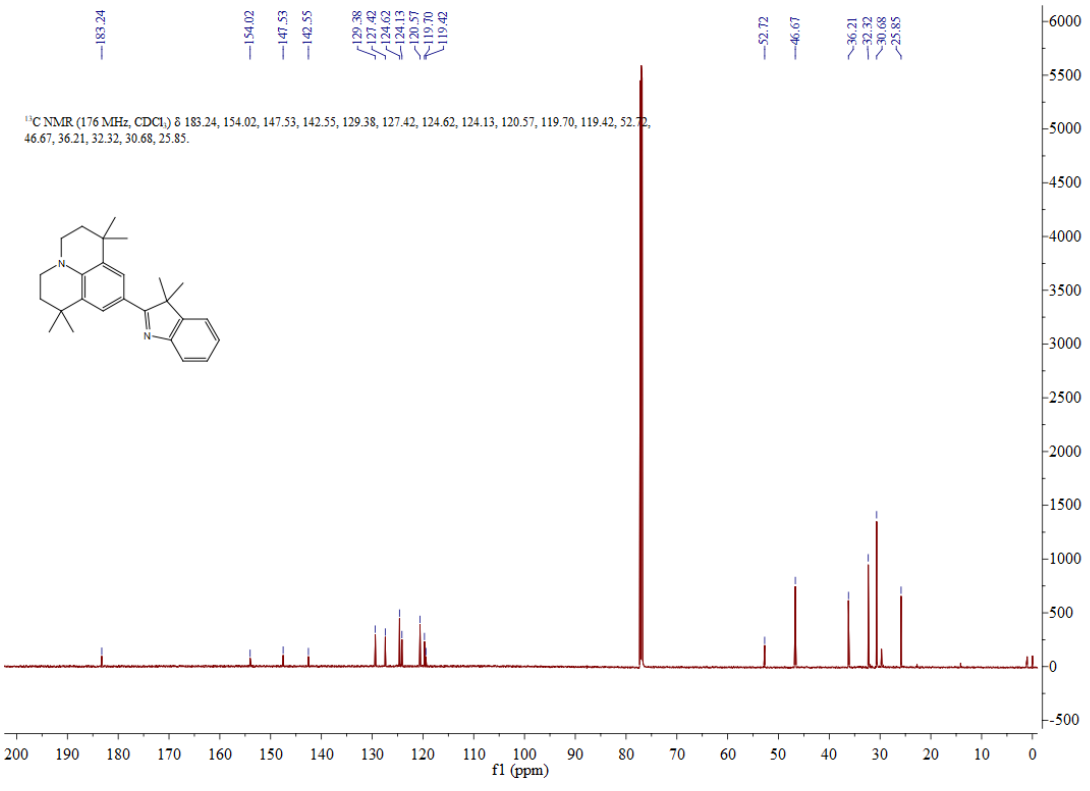

*Figure S32. [13]C-NMR spectrum of **C1** in $CDCl_3$.*

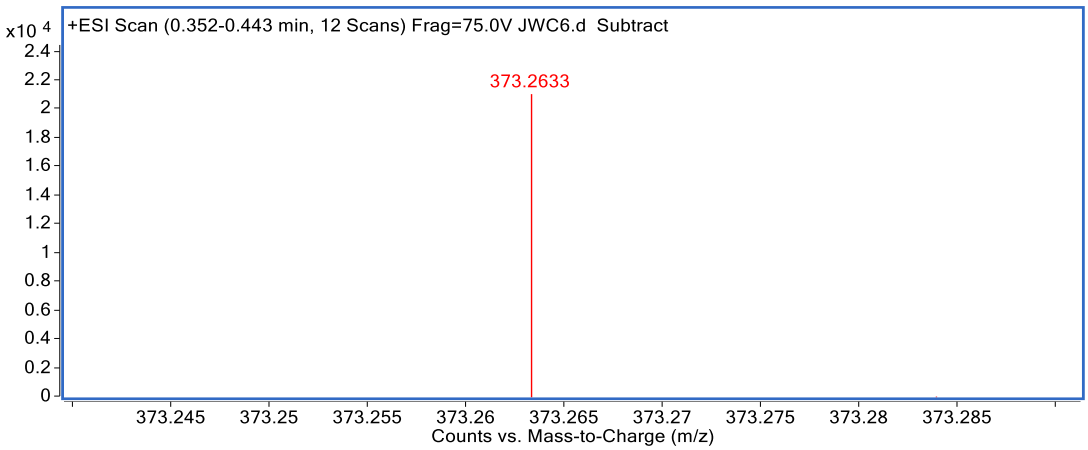

*Figure S33. HRMS spectrum of **C1**.*

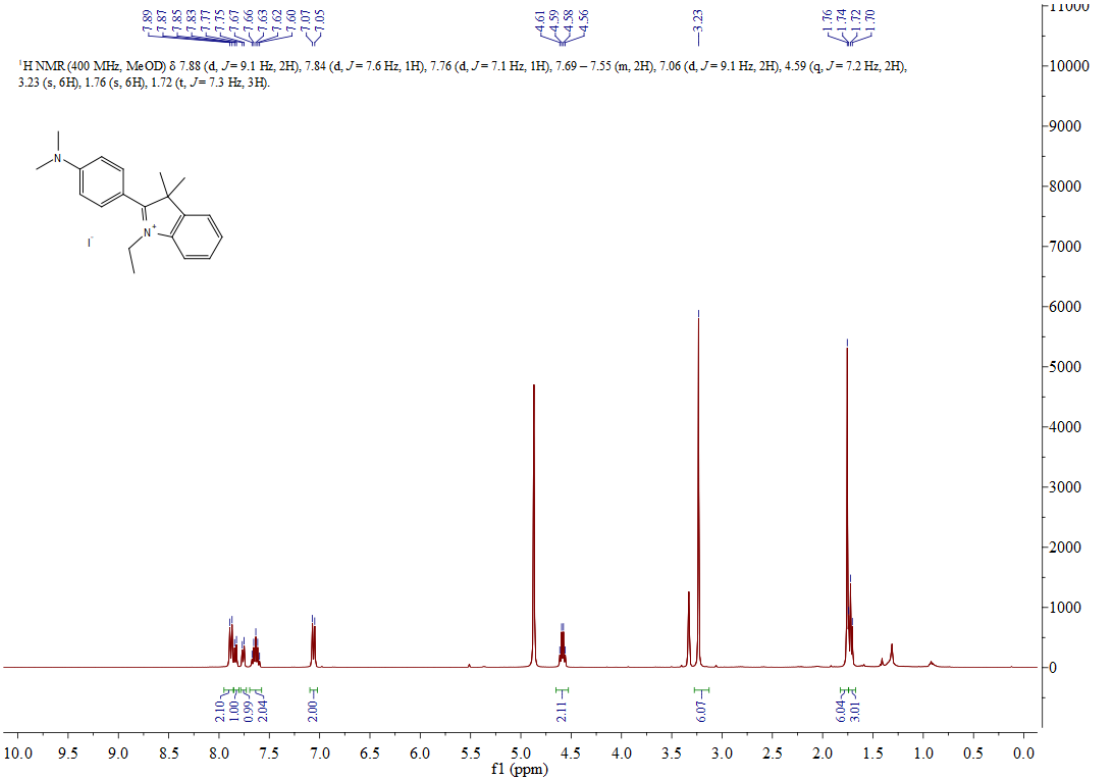

*Figure S34. ^{1}H-NMR spectrum of **A3** in $CDCl_3$.*

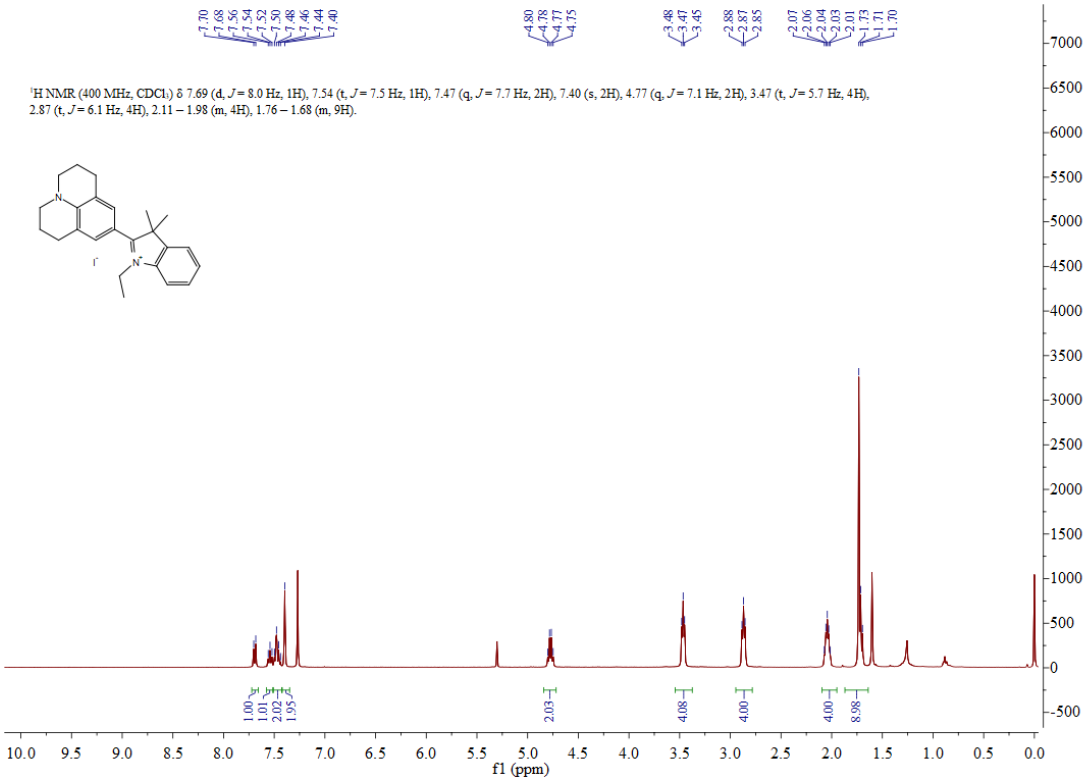

*Figure S35. [1]H-NMR spectrum of **B3** in $CDCl_3$.*

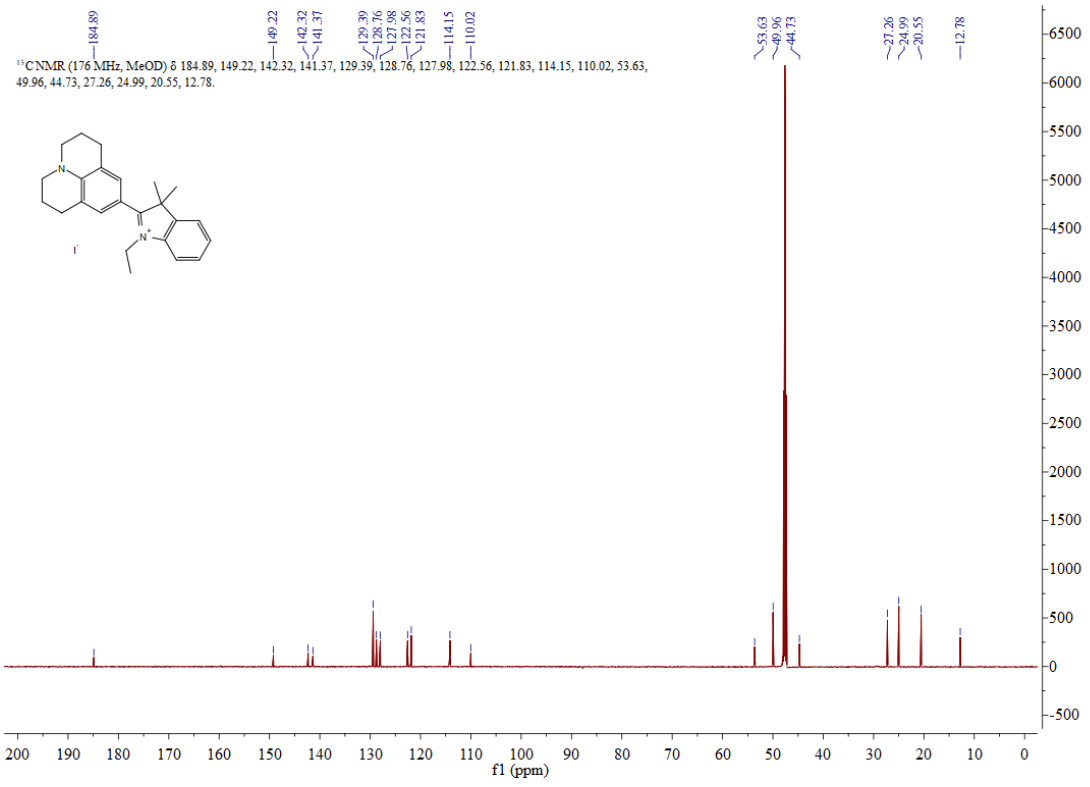

*Figure S36. [13]C-NMR spectrum of **B3** in MeOD.*

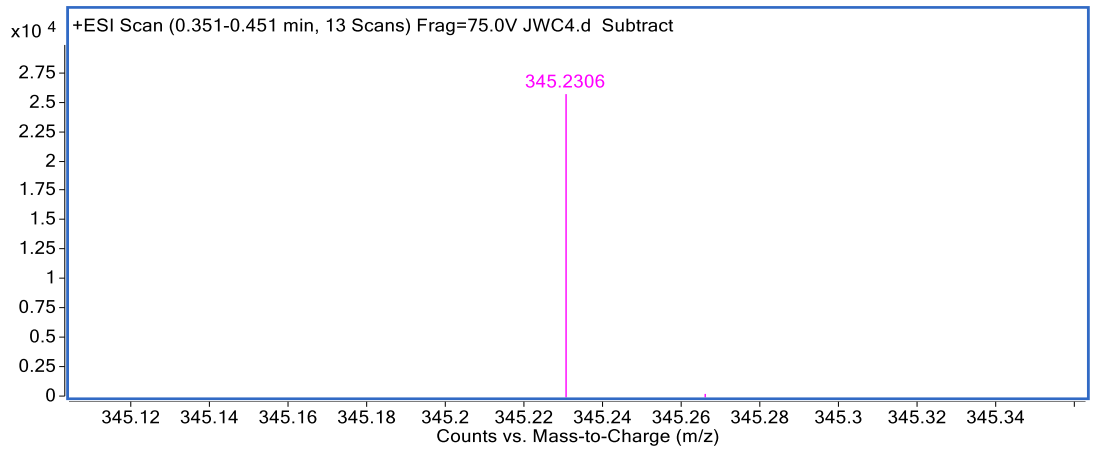

*Figure S37. HRMS spectrum of **B3**.*

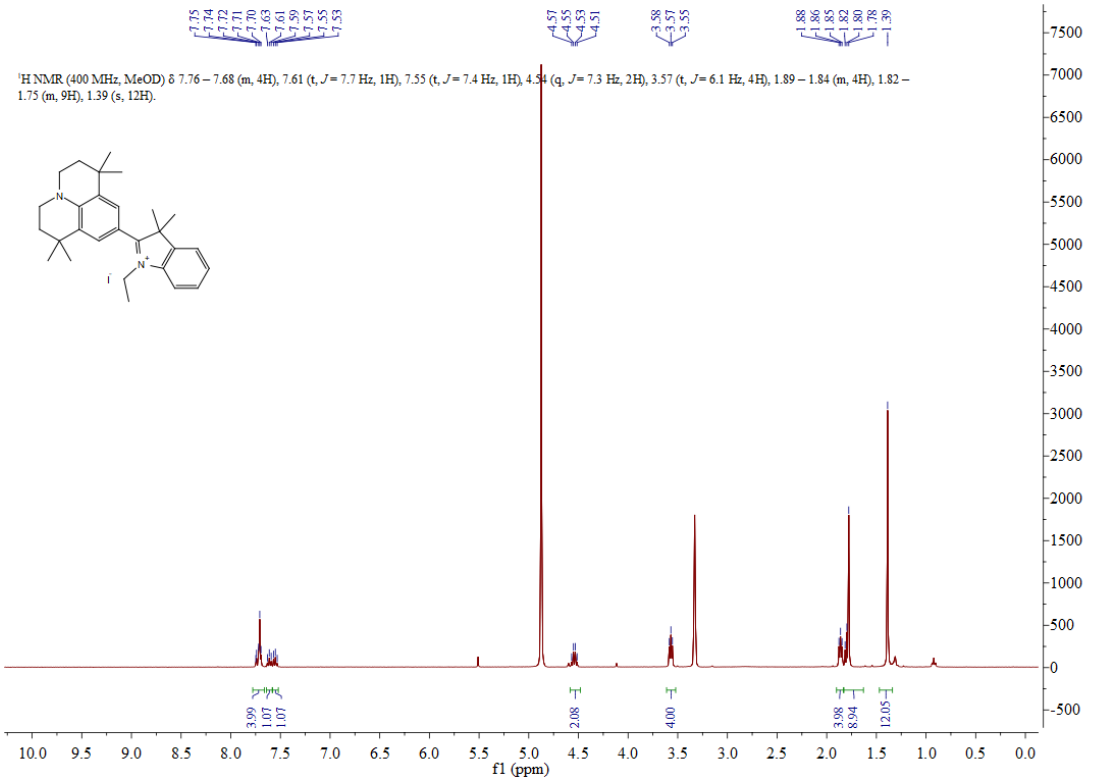

*Figure S38. ^{1}H-NMR spectrum of **C3** in MeOD*

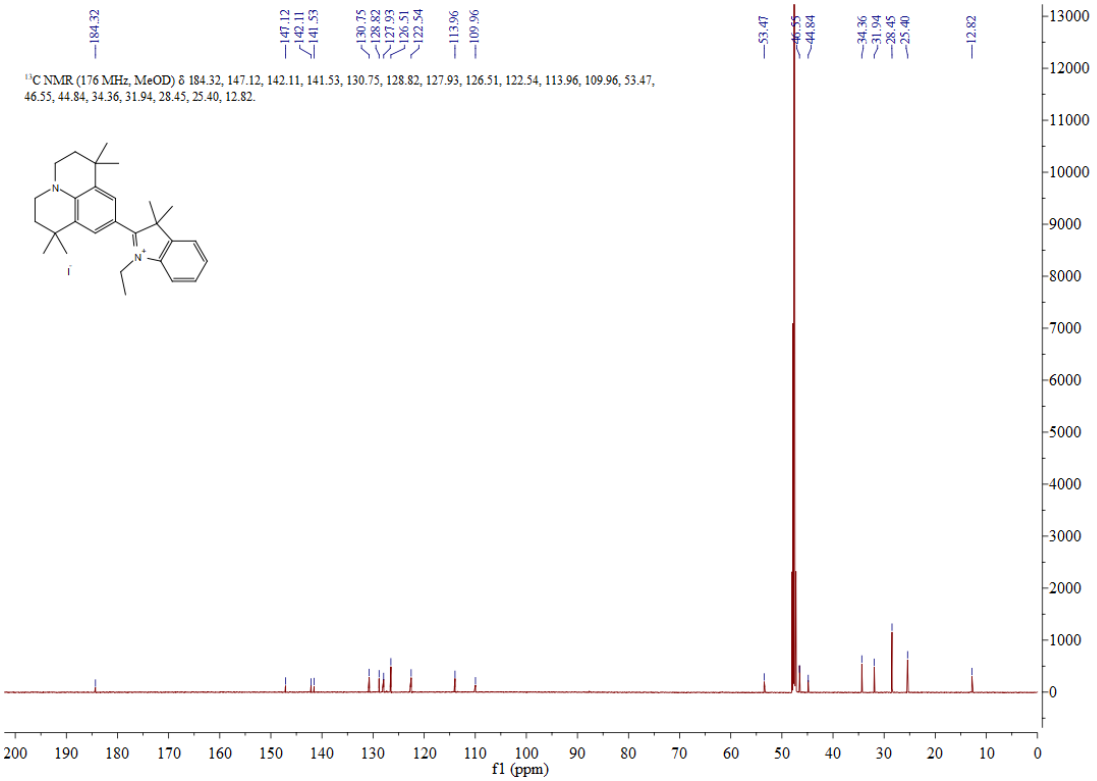

*Figure S39. ^{13}C-NMR spectrum of **C3** in MeOD*

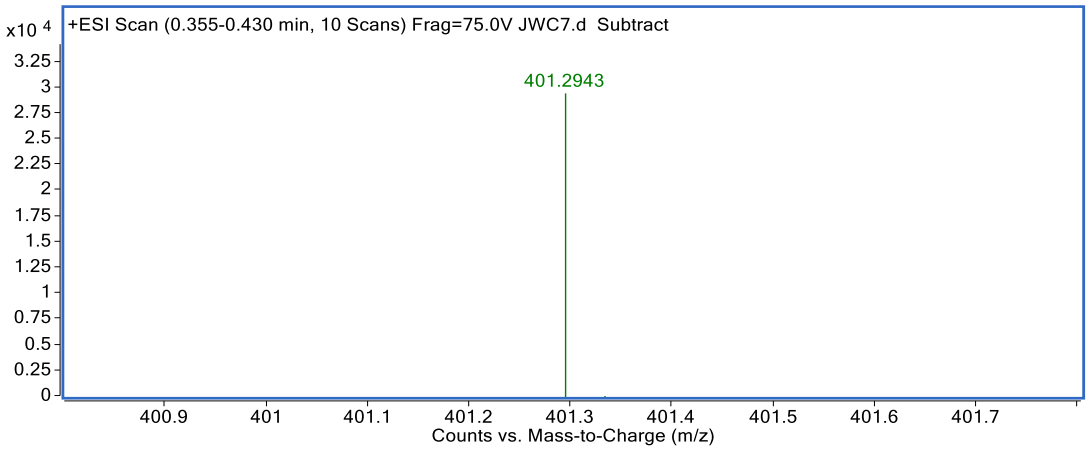

*Figure S40. HRMS spectrum of **C3**.*

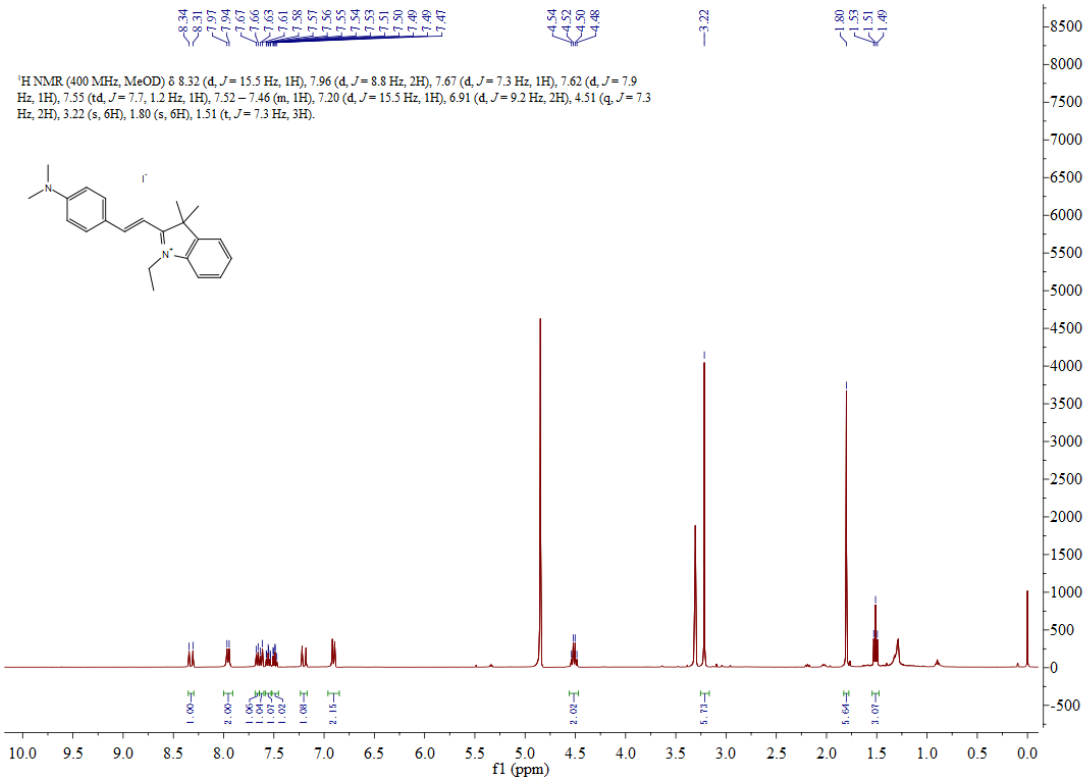

*Figure S41. [1]H-NMR spectrum of **A4** in MeOD.*

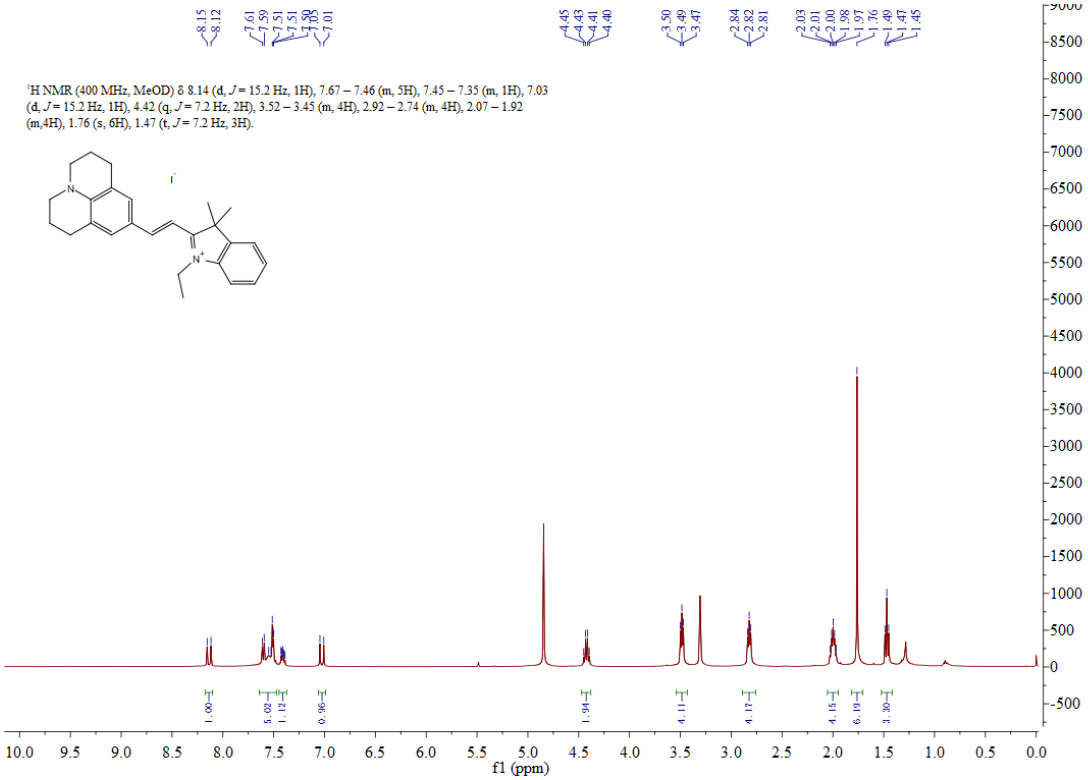

*Figure S42. [1]H-NMR spectrum of **B4** in MeOD.*

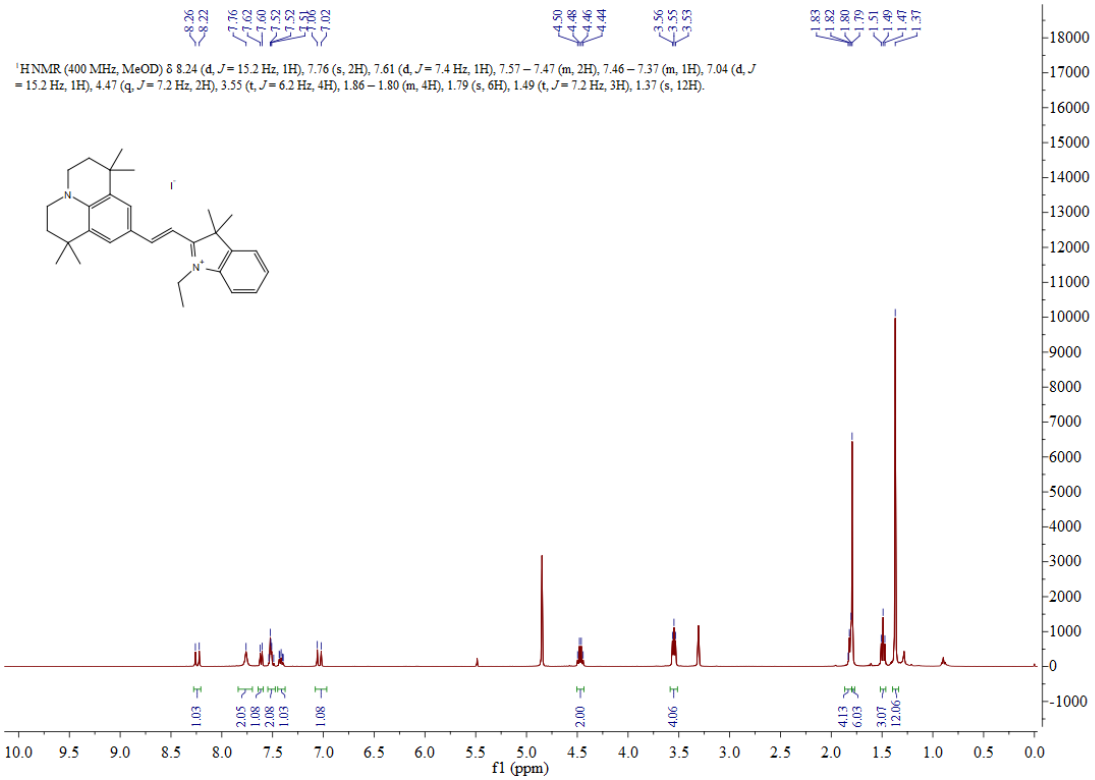

*Figure S43. [1]H-NMR spectrum of **C4** in MeOD.*

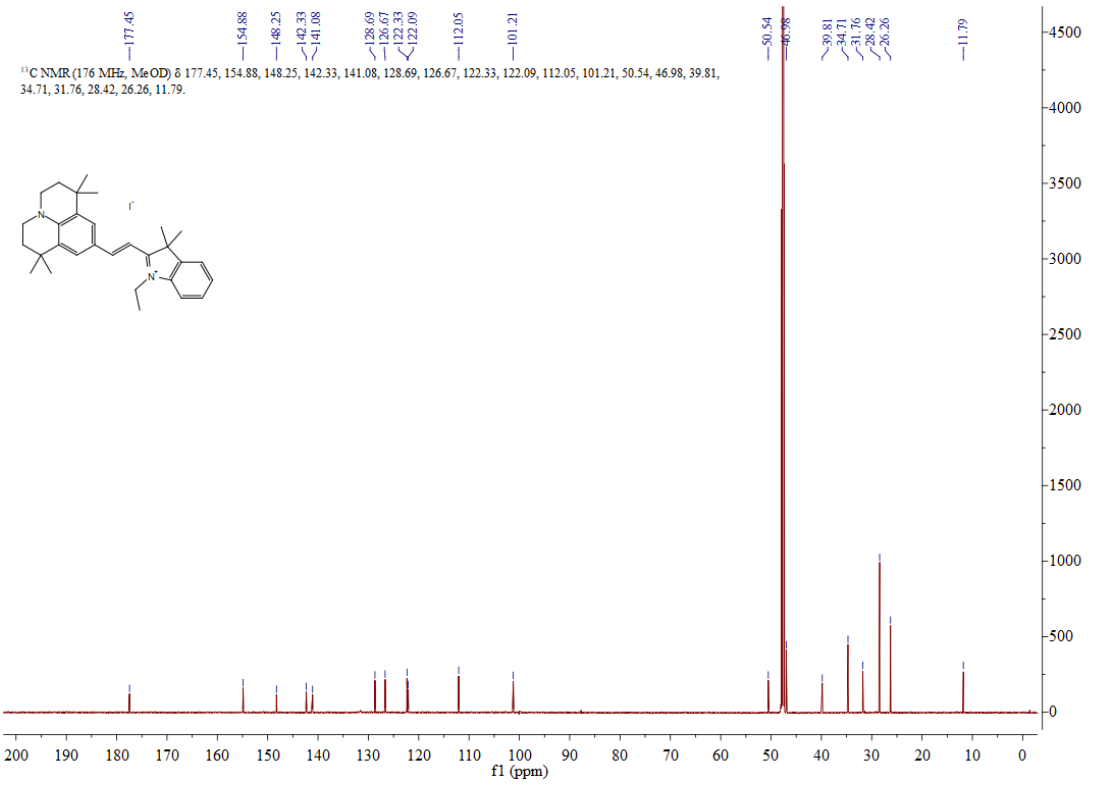

*Figure S44. [13]C-NMR spectrum of **C4** in MeOD.*

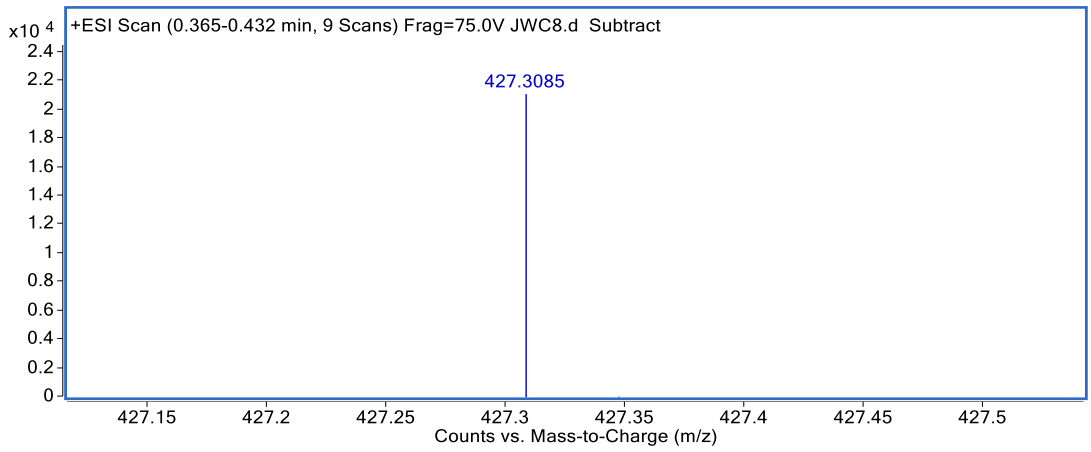

*Figure S45. HRMS spectrum of **C4**.*

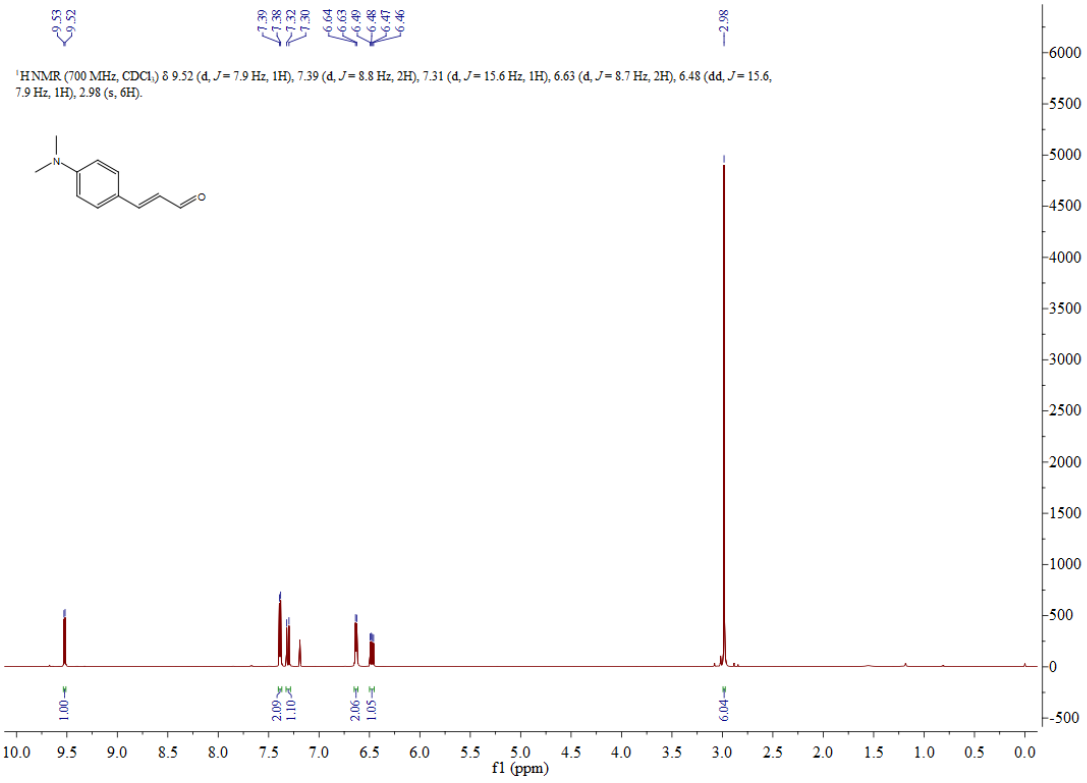

*Figure S46. ^{1}H-NMR spectrum of **PA4** in $CDCl_3$.*

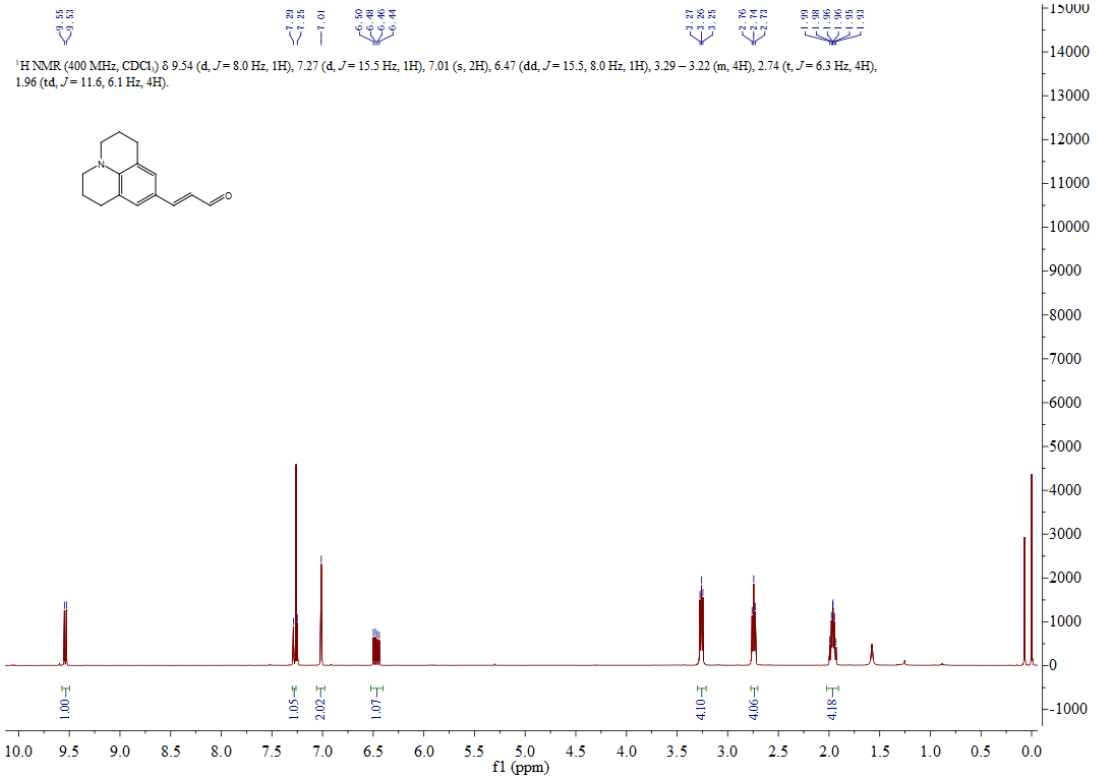

*Figure S47. ¹H-NMR spectrum of **PB4** in $CDCl_3$.*

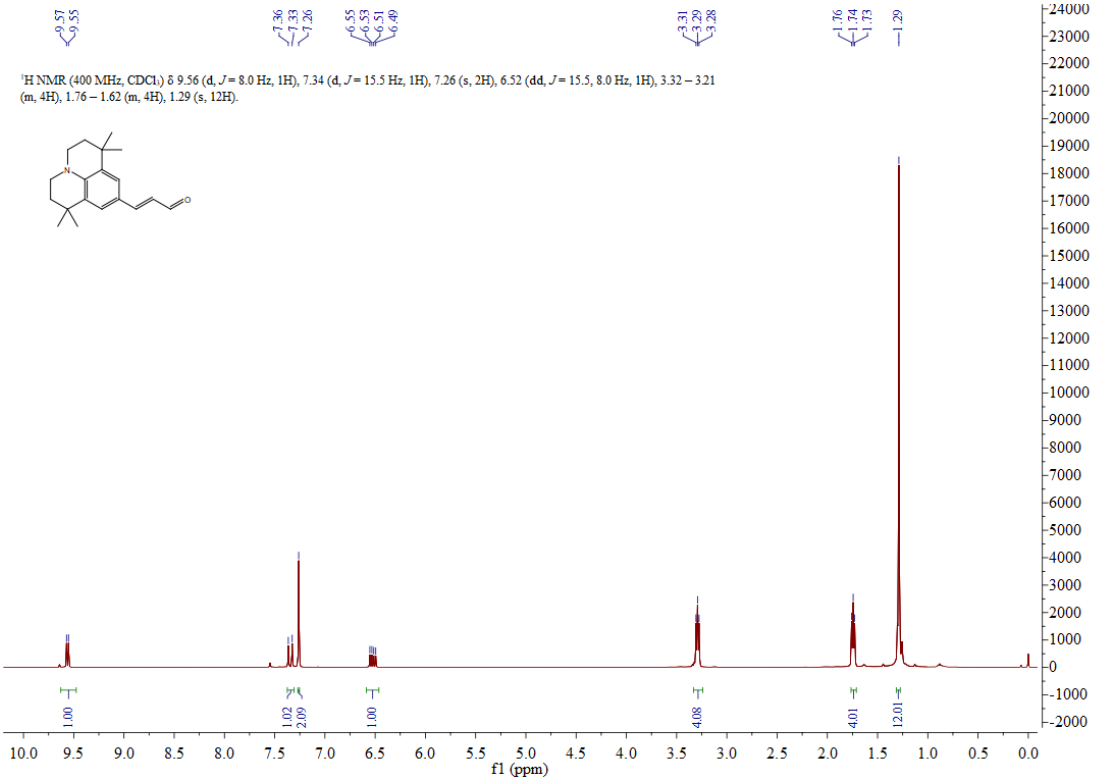

*Figure S48. ¹H-NMR spectrum of **PC4** in $CDCl_3$.*

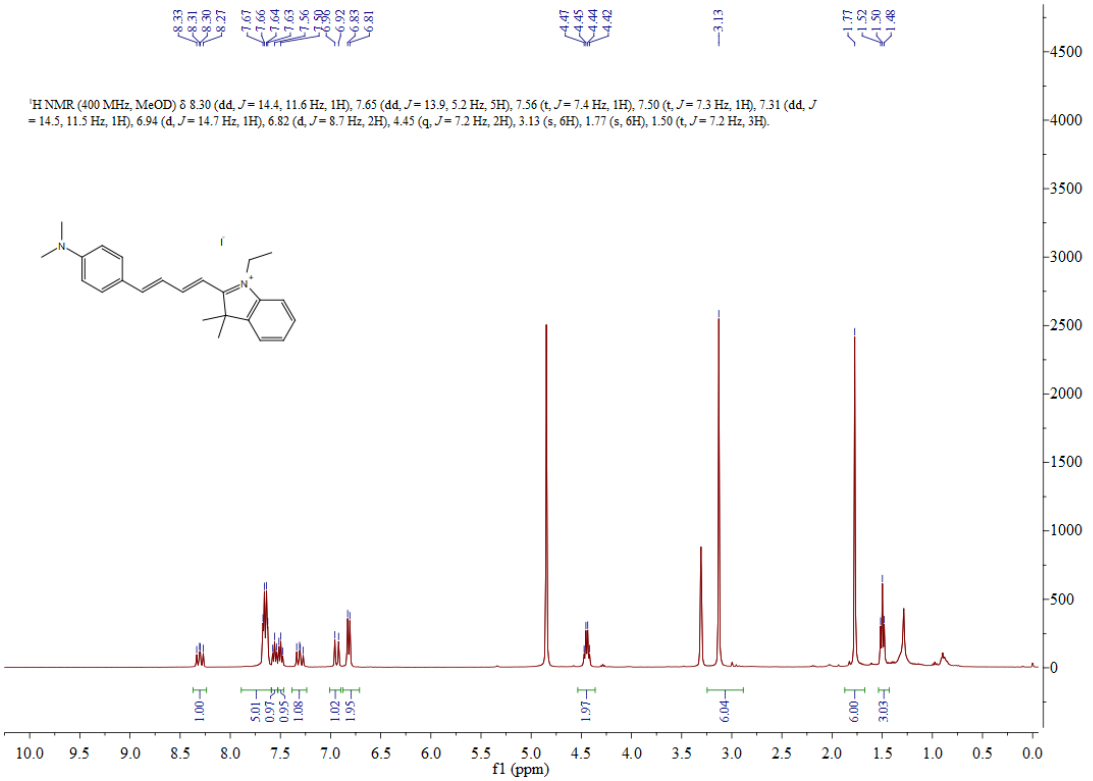

*Figure S49. [1]H-NMR spectrum of **A5** in MeOD.*

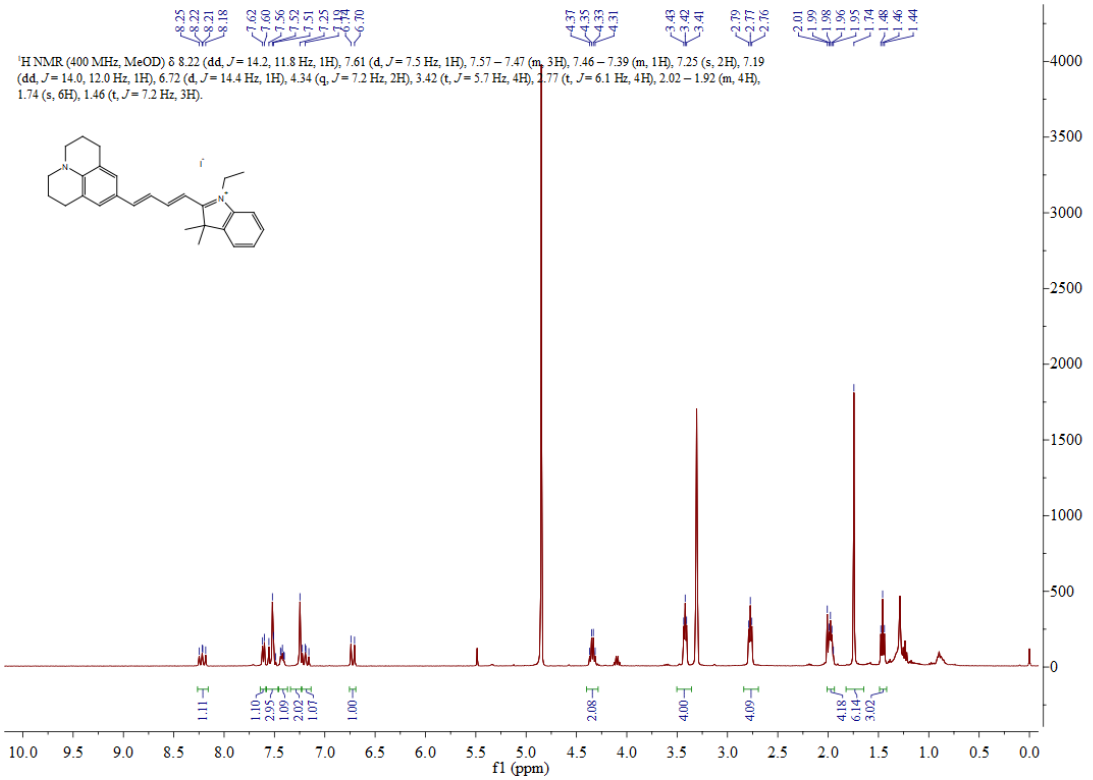

*Figure S50. [1]H-NMR spectrum of **B5** in MeOD.*

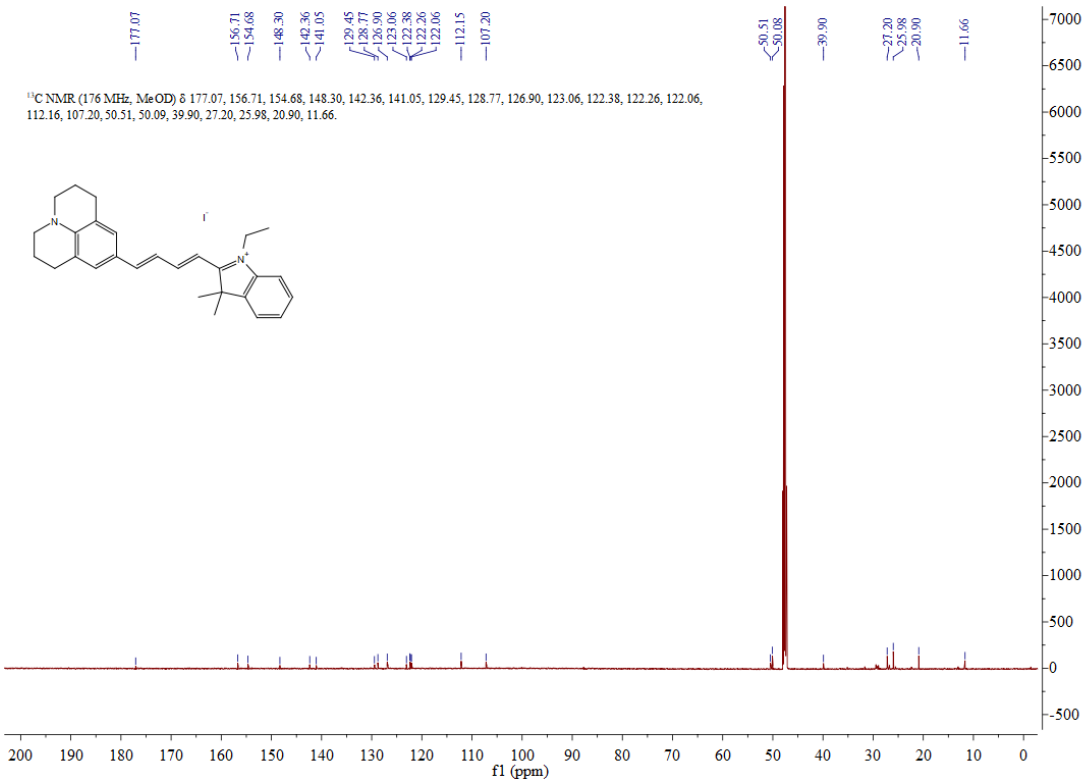

*Figure S51. ^{13}C-NMR spectrum of **B5** in MeOD.*

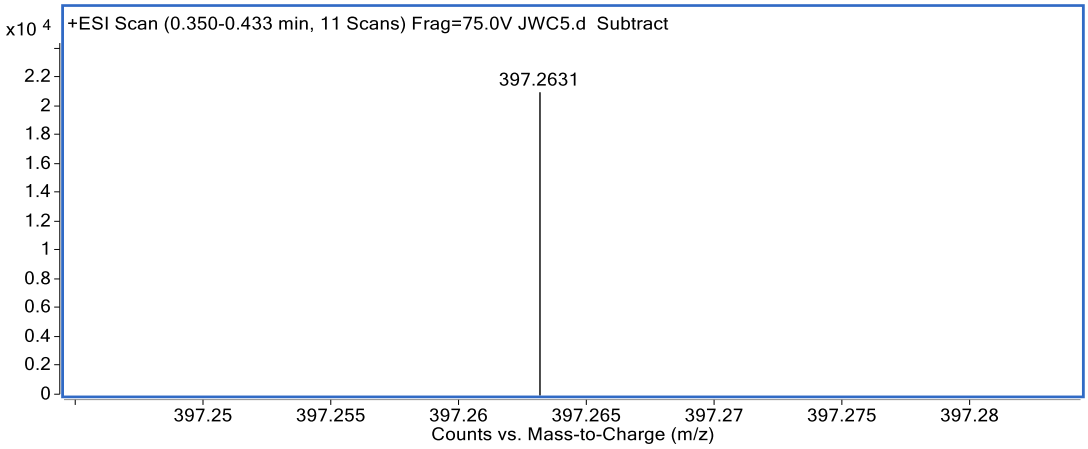

*Figure S52. HRMS spectrum of **B5**.*

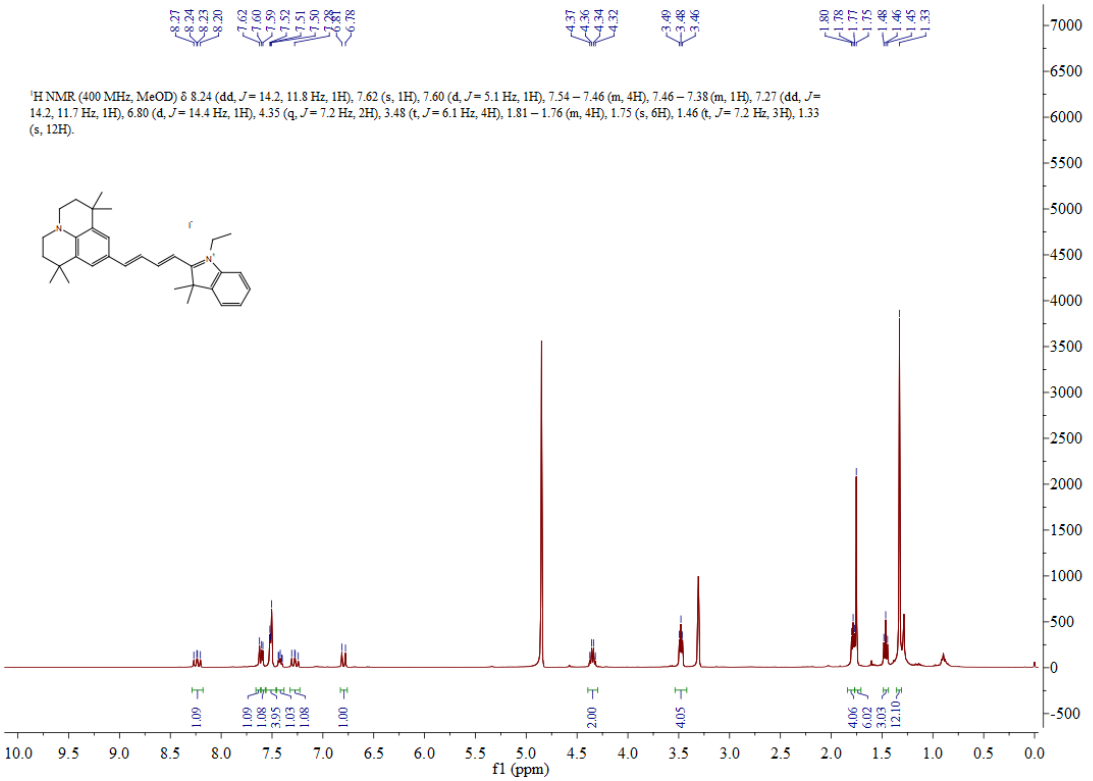

*Figure S53. [1]H-NMR spectrum of **C5** in MeOD.*

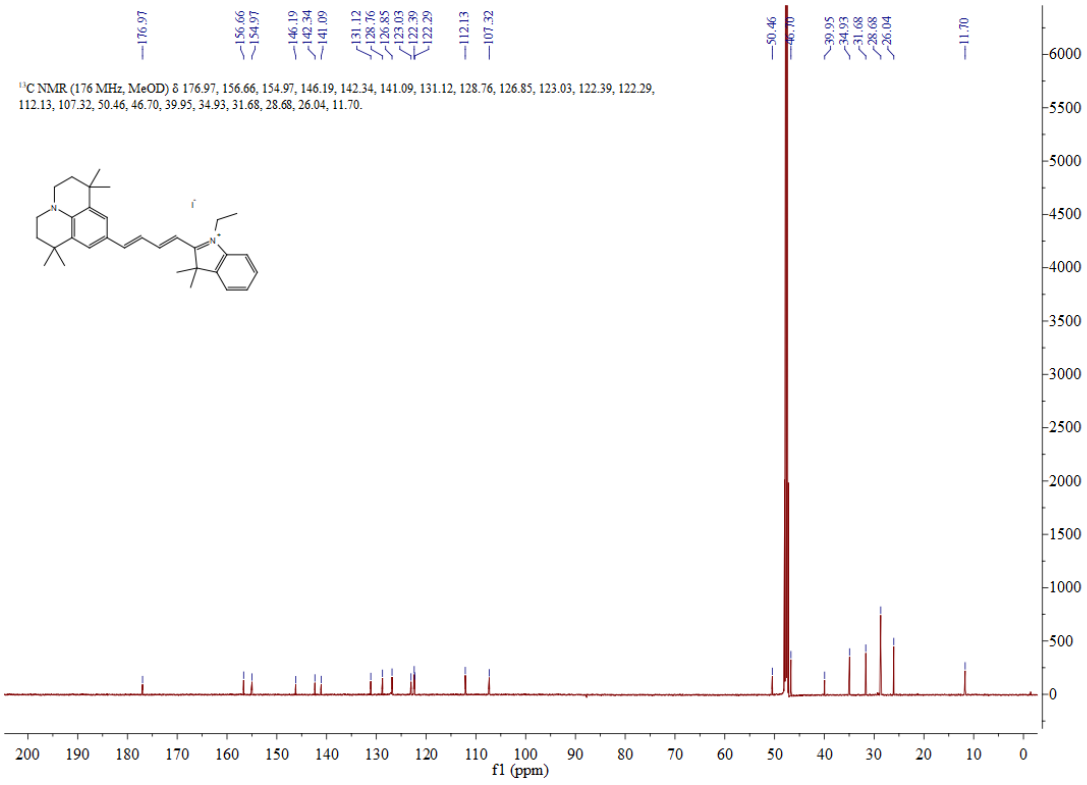

*Figure S54. [13]C-NMR spectrum of **C5** in MeOD.*

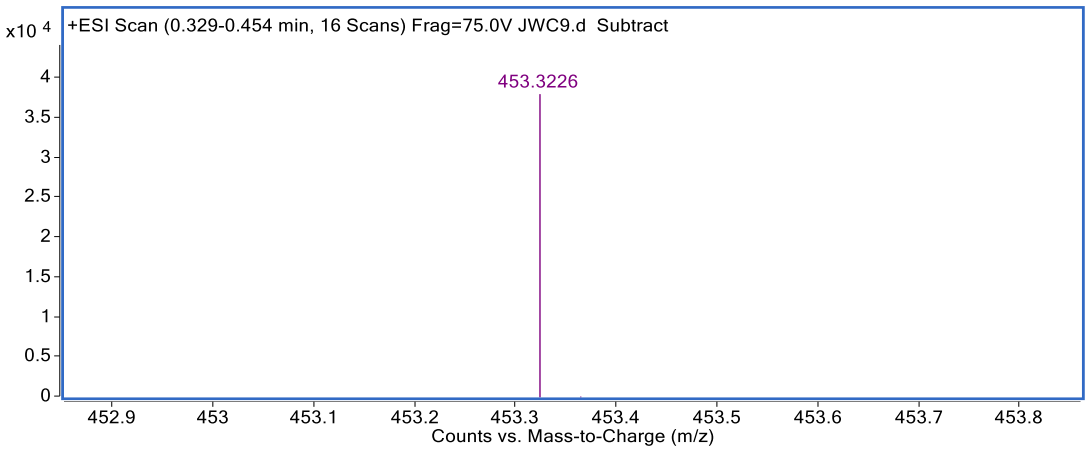

*Figure S55. HRMS spectrum of **C5**.*

4. Additional Spectroscopic Data of Hemi-Cyanine Derivatives

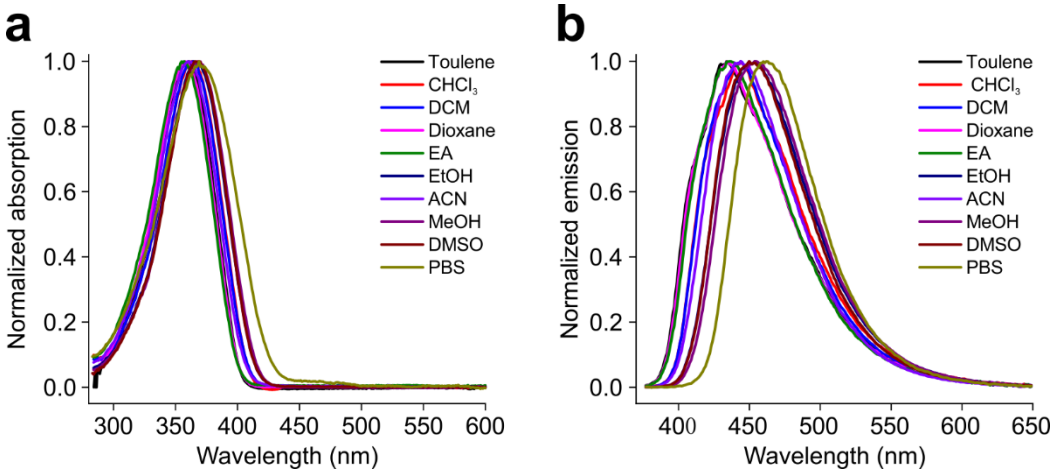

*Figure S56. Normalized UV-vis absorption and emission spectra of **A1** in various solvents.*

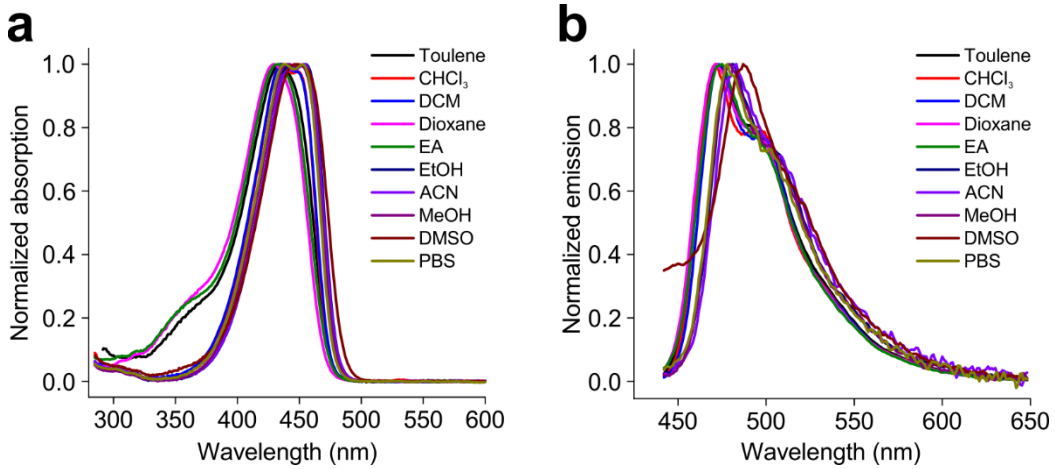

*Figure S57. Normalized UV-vis absorption and emission spectra of **A2** in various solvents.*

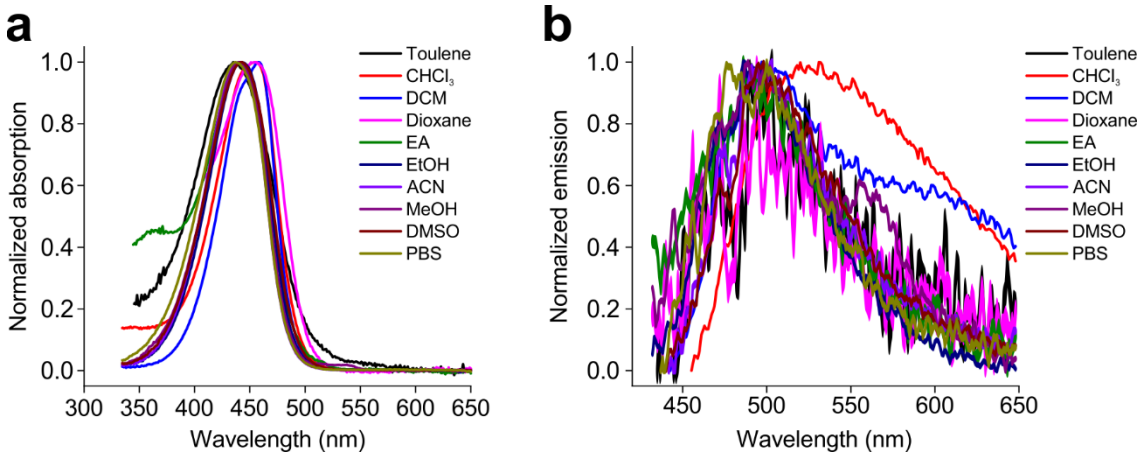

*Figure S58. Normalized UV-vis absorption and emission spectra of **A3** in various solvents.*

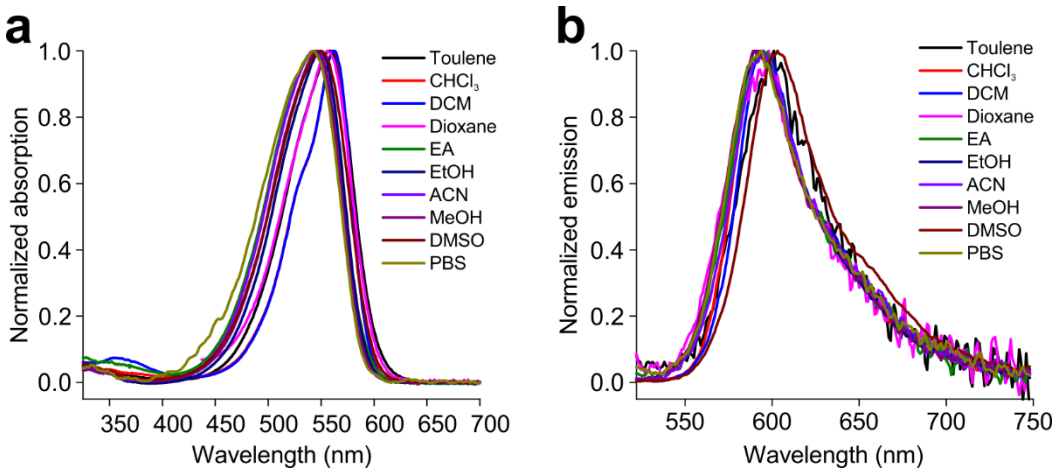

*Figure S59. Normalized UV-vis absorption and emission spectra of **A4** in various solvents.*

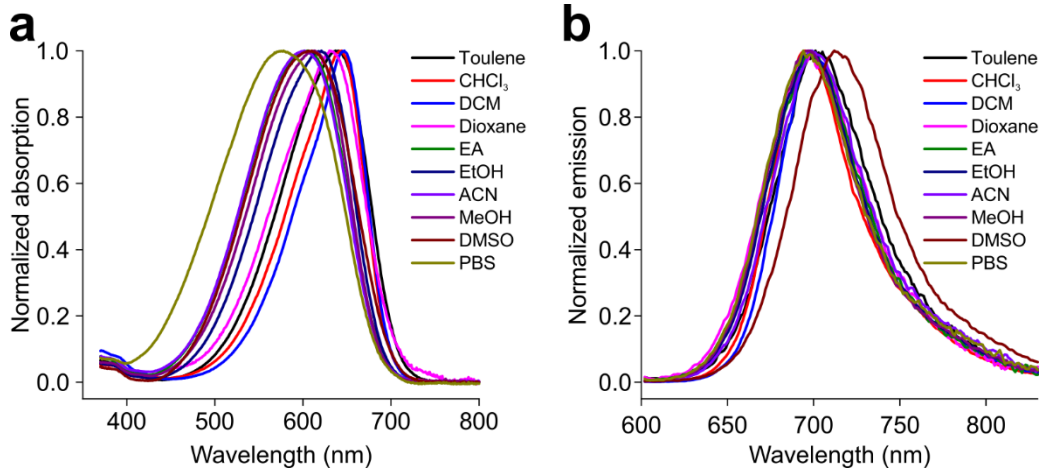

*Figure S60. Normalized UV-vis absorption and emission spectra of **A5** in various solvents.*

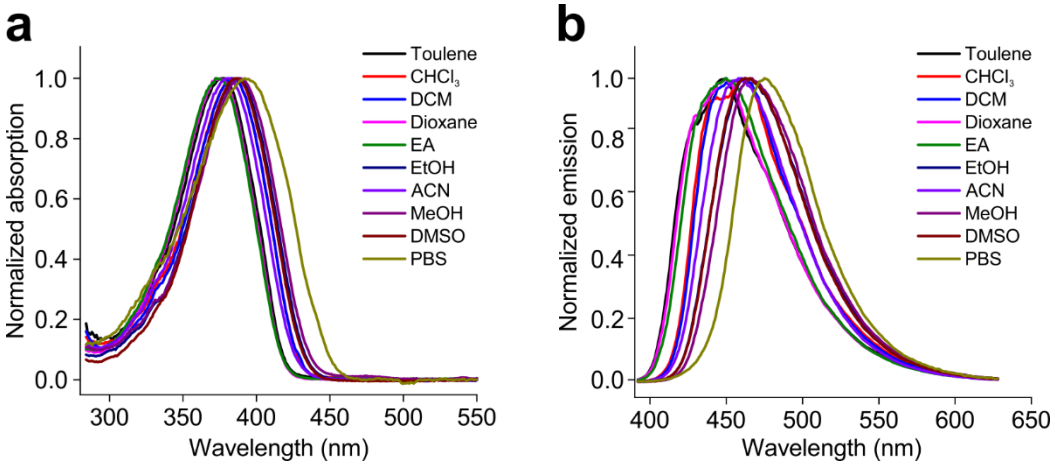

*Figure S61. Normalized UV-vis absorption and emission spectra of **B1** in various solvents.*

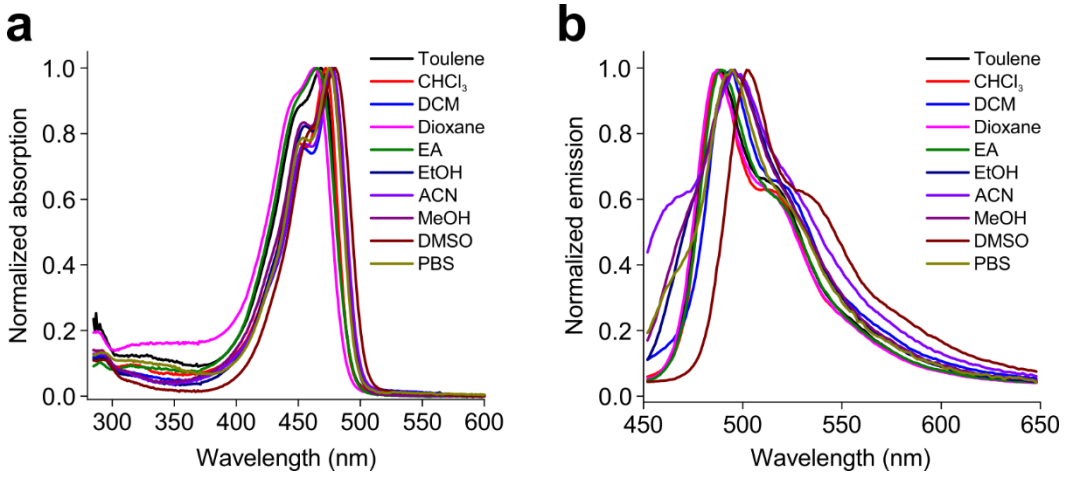

*Figure S62. Normalized UV-vis absorption and emission spectra of **B2** in various solvents.*

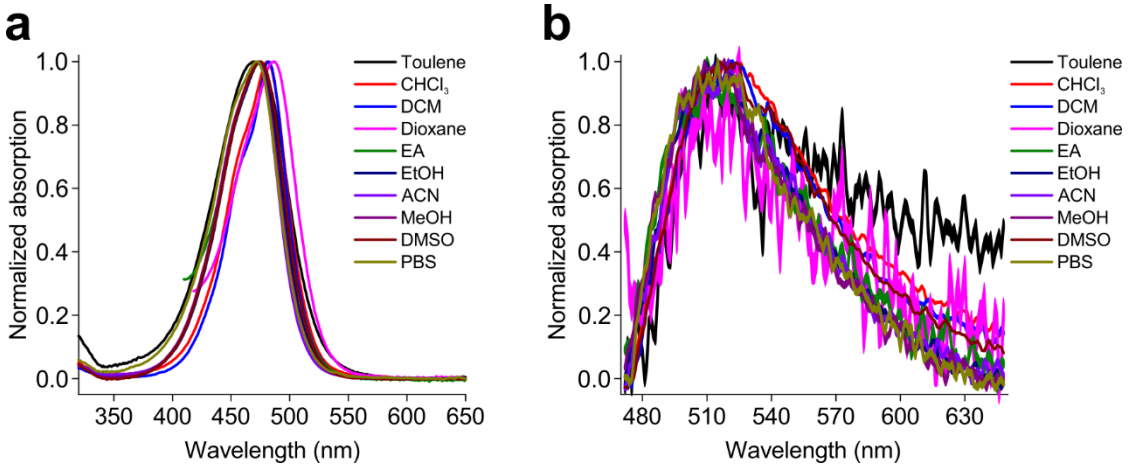

*Figure S63. Normalized UV-vis absorption and emission spectra of **B3** in various solvents.*

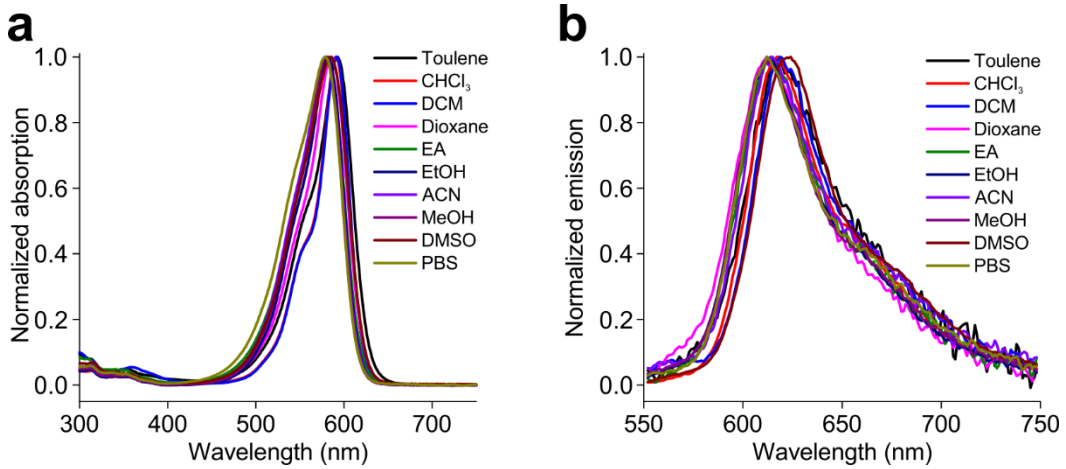

*Figure S64. Normalized UV-vis absorption and emission spectra of **B4** in various solvents.*

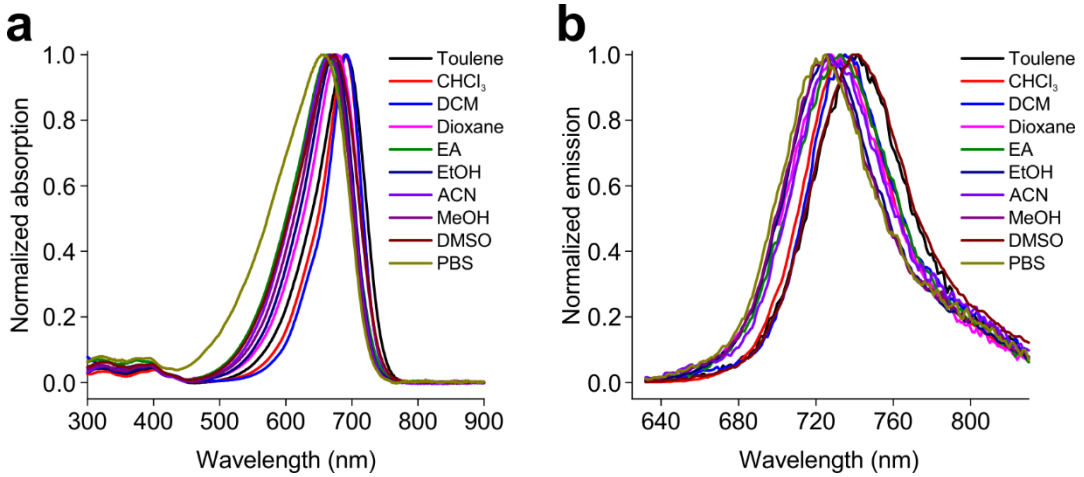

*Figure S65. Normalized UV-vis absorption and emission spectra of **B5** in various solvents.*

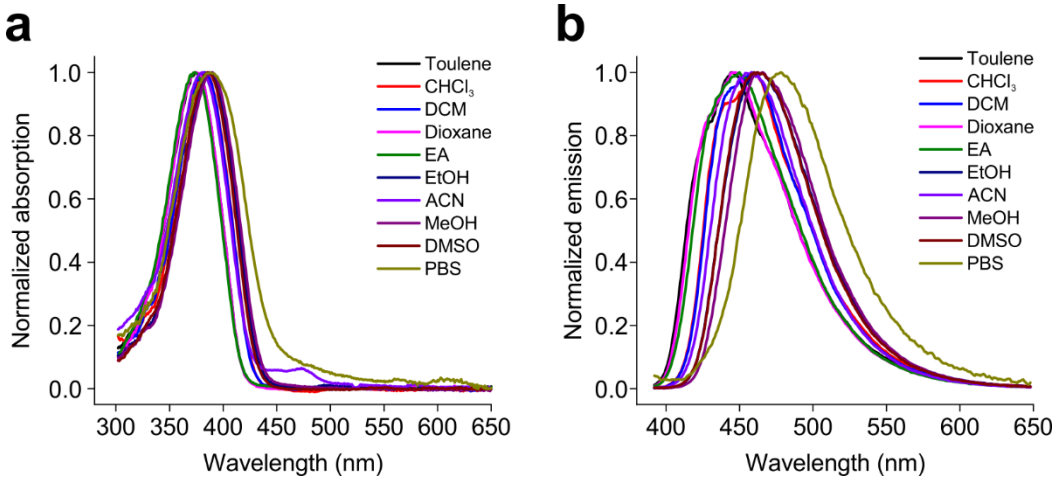

*Figure S66. Normalized UV-vis absorption and emission spectra of **C1** in various solvents.*

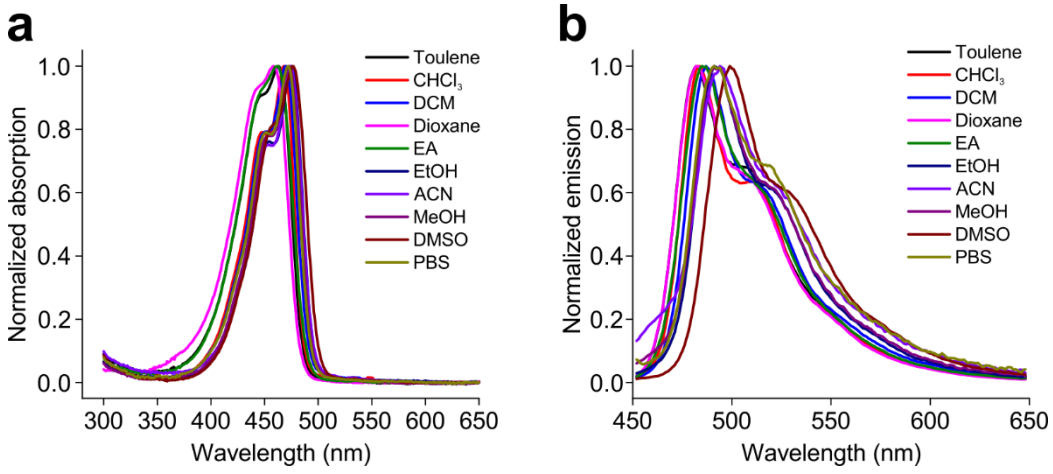

*Figure S67. Normalized UV-vis absorption and emission spectra of **C2** in various solvents.*

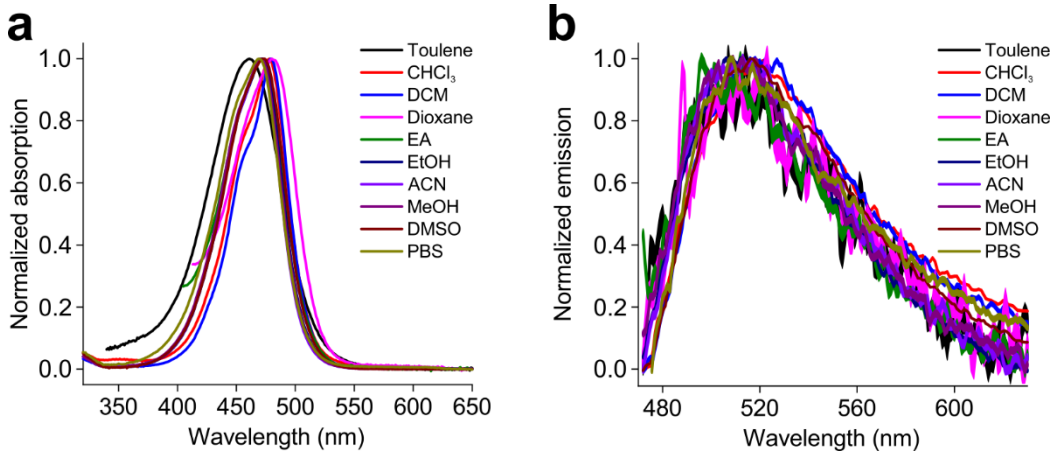

*Figure S68. Normalized UV-vis absorption and emission spectra of **C3** in various solvents.*

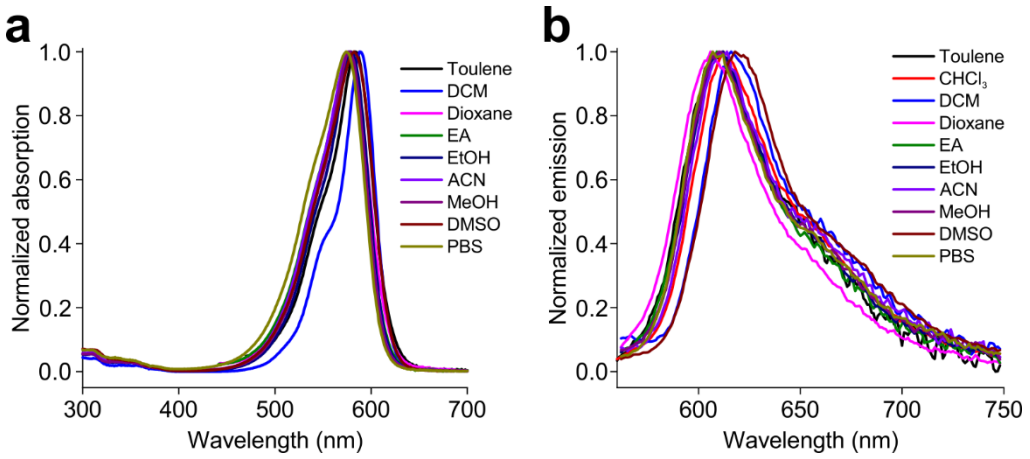

*Figure S69. Normalized UV-vis absorption and emission spectra of **C4** in various solvents.*

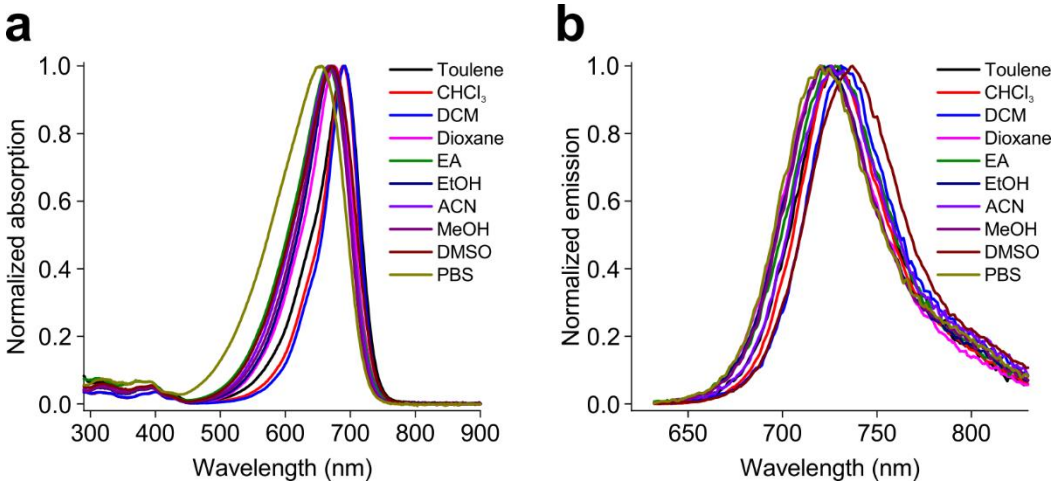

*Figure S70. Normalized UV-vis absorption and emission spectra of **C5** in various solvents.*

5. Additional Computational Results of Hemi-Cyanine Derivatives

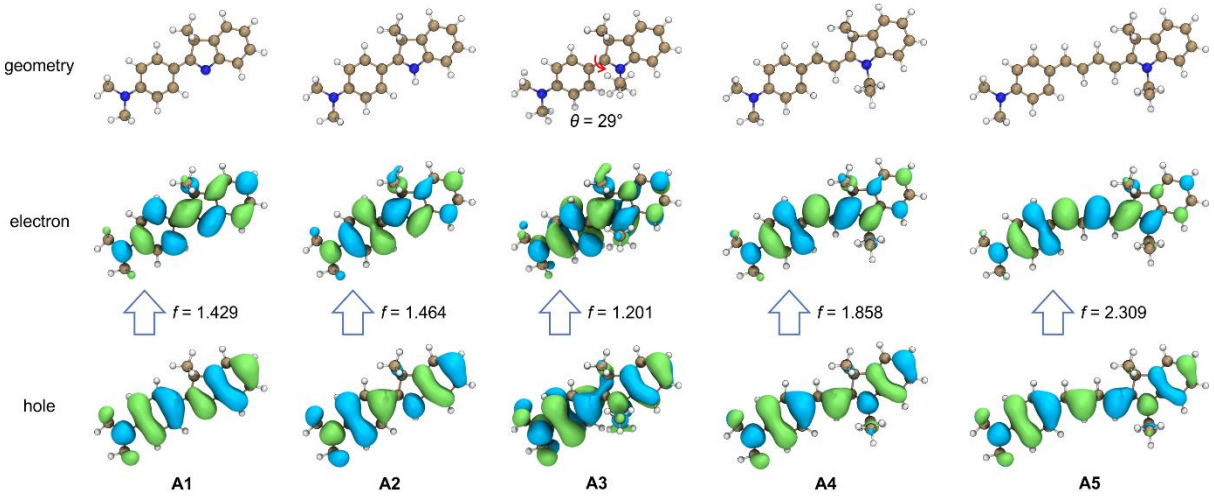

*Figure S71. NTOs of LE state of **A1** – **A5** optimized at the ωB97XD/Def2SVP level in the water. The corresponding oscillator strength (f) is labeled in the inset.*

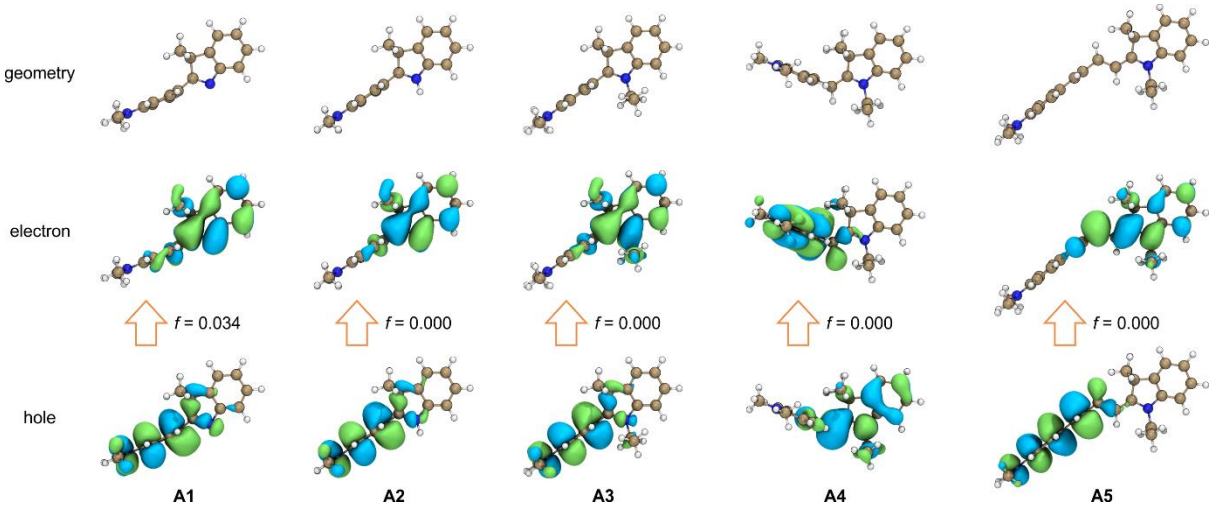

*Figure S72. NTOs of TICT state of **A1** – **A5** optimized at the ωB97XD/Def2SVP level in the water. The corresponding oscillator strength (f) is labeled in the inset.*

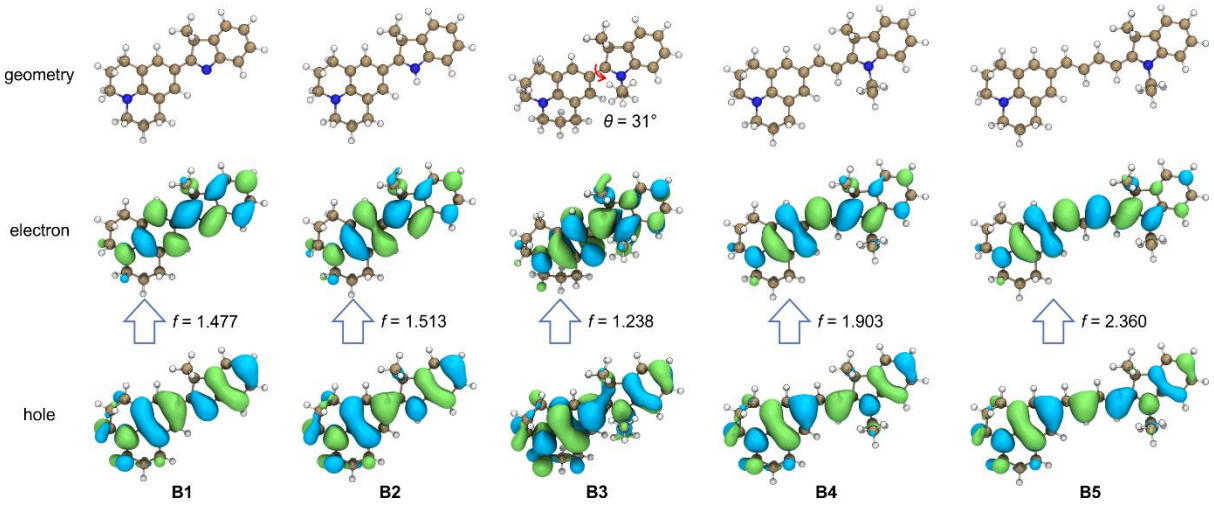

*Figure S73. NTOs of LE state of **B1** – **B5** optimized at the ωB97XD/Def2SVP level in the water. The corresponding oscillator strength (f) is labeled in the inset.*

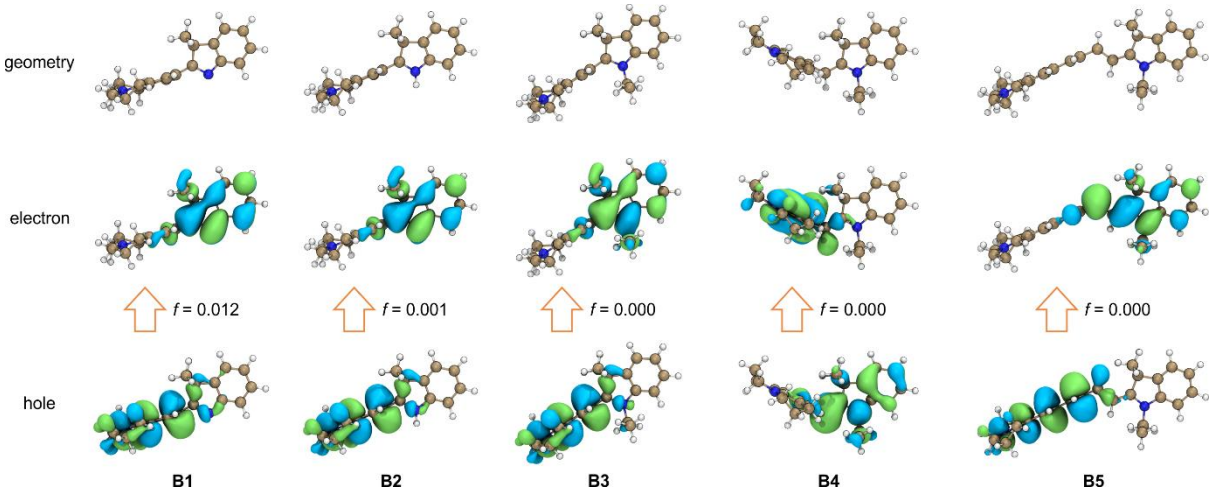

*Figure S74. NTOs of TICT state of **B1** – **B5** optimized at the ωB97XD/Def2SVP level in the water. The corresponding oscillator strength (f) is labeled in the inset.*

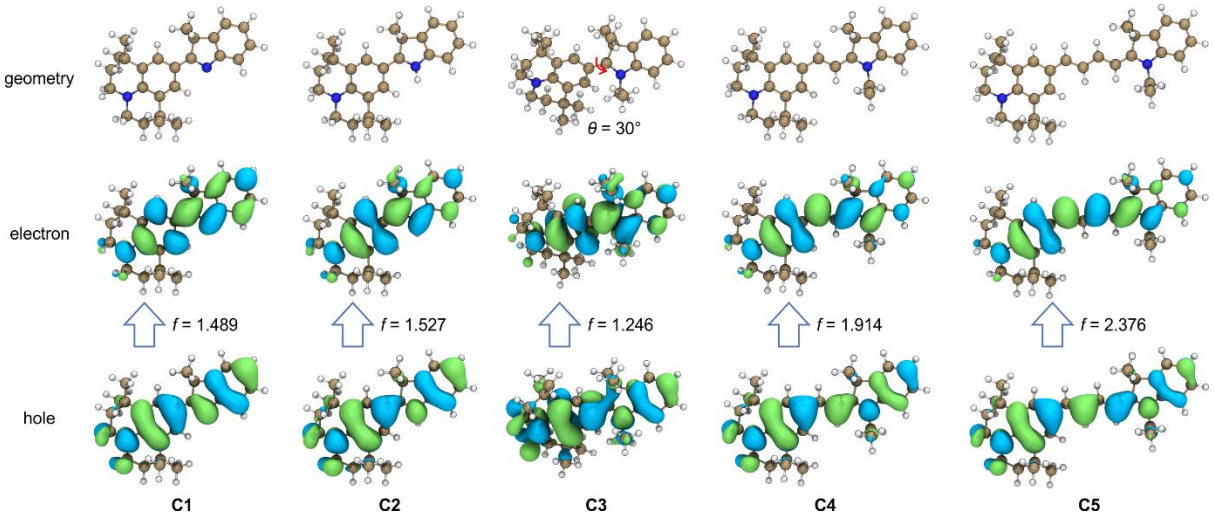

*Figure S75. NTOs of LE state of **C1** – **C5** optimized at the ωB97XD/Def2SVP level in the water. The corresponding oscillator strength (f) is labeled in the inset.*

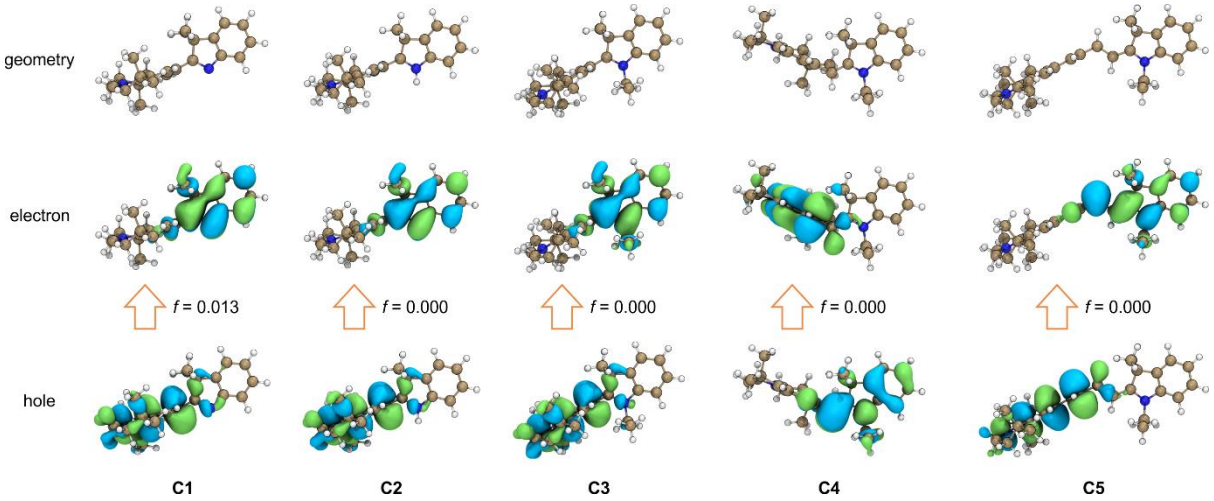

*Figure S76. NTOs of TICT state of **C1** – **C5** optimized at the ωB97XD/Def2SVP level in the water. The corresponding oscillator strength (f) is labeled in the inset.*

6. TICT Formation and Viscosity Response of Hemi-Cyanines (A and C series)

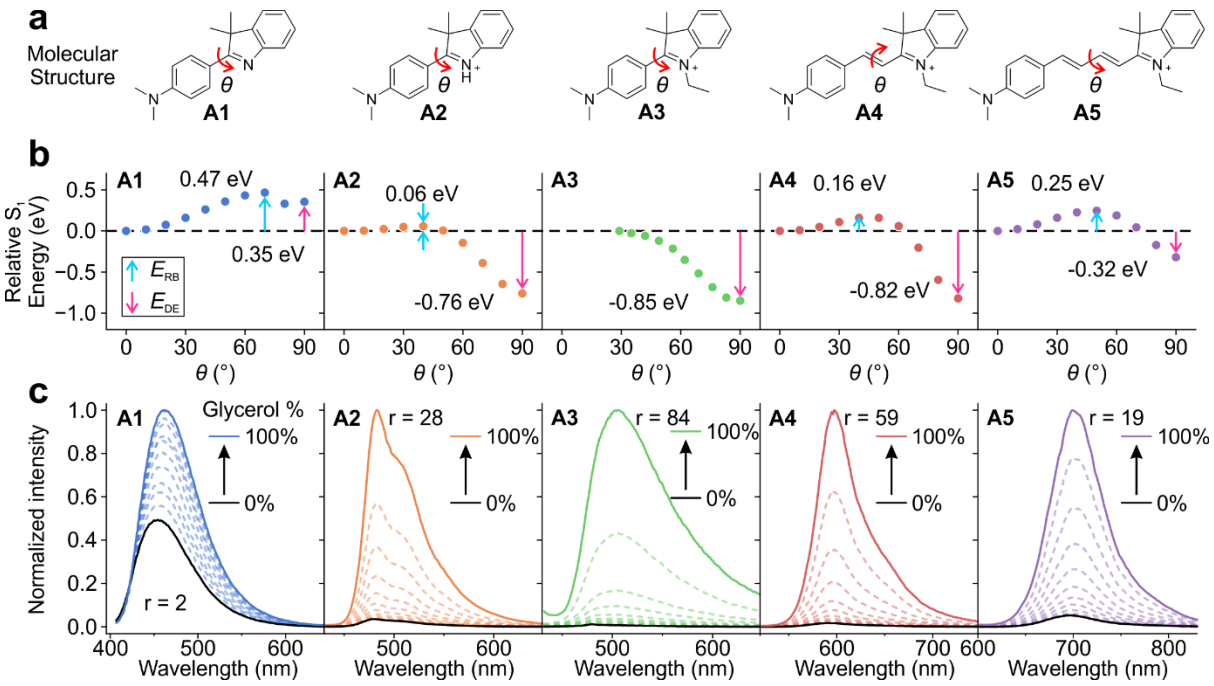

*Figure S77. (a) Chemical structures, (b) Calculated S_1 PES for TICT at the ωB97XD/Def2SVP/cLR-PCM level in the water, and (c) viscosity response of **A1**-**A5**.*

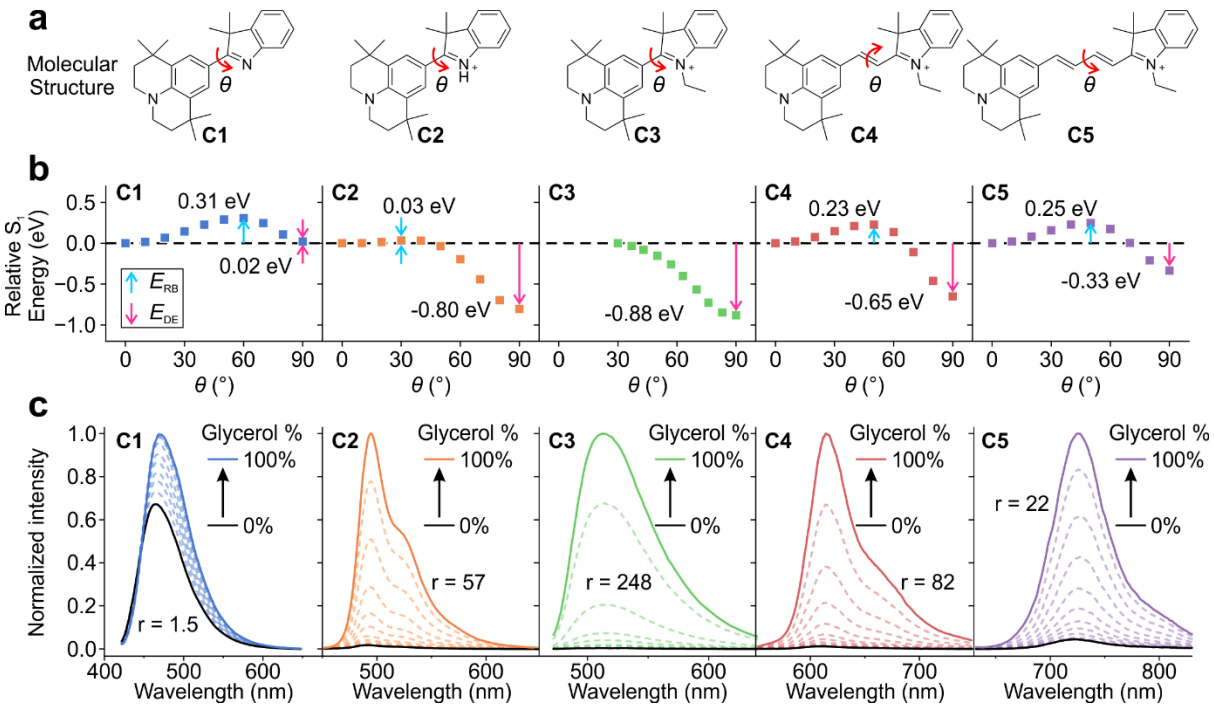

*Figure S78. (a) Chemical structures, (b) Calculated S_1 PES for TICT at the ωB97XD/Def2SVP/cLR-PCM level in the water, and (c) viscosity response of **C1**-**C5**.*

7. Distance Project Maps of Hemi-Cyanine Derivatives

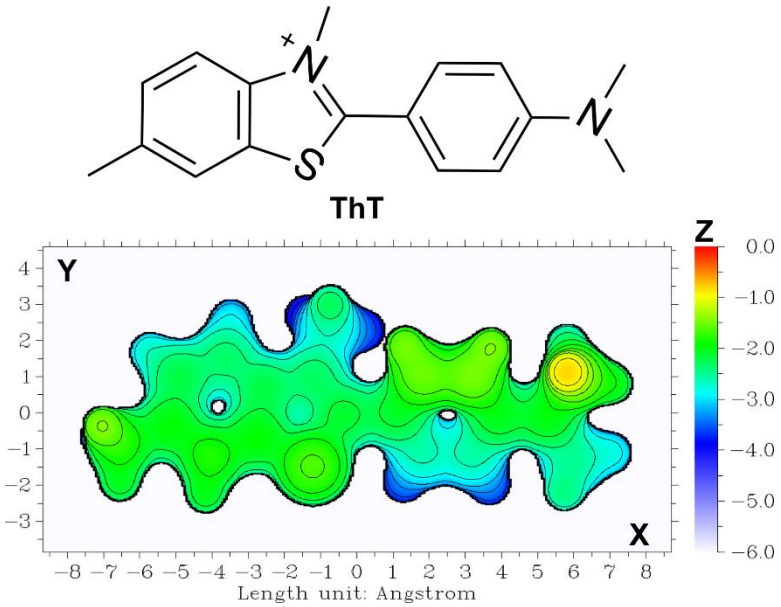

*Figure S79. The chemical structure and distance projection map of **ThT** calculated at the ωB97XD/Def2SVP level in the water.*

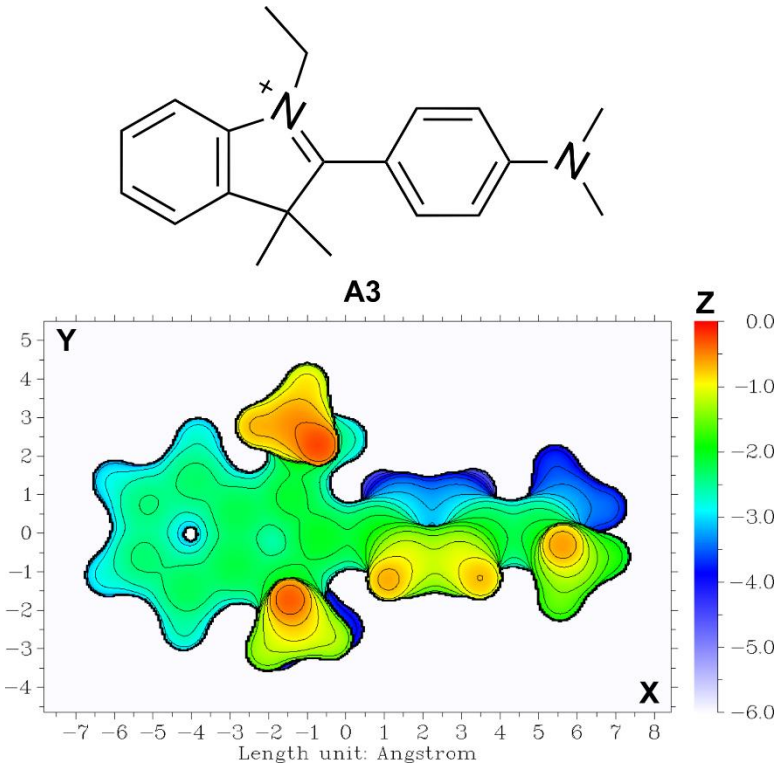

*Figure S80. The chemical structure and distance projection map of **A3** calculated at the ωB97XD/Def2SVP level in the water.*

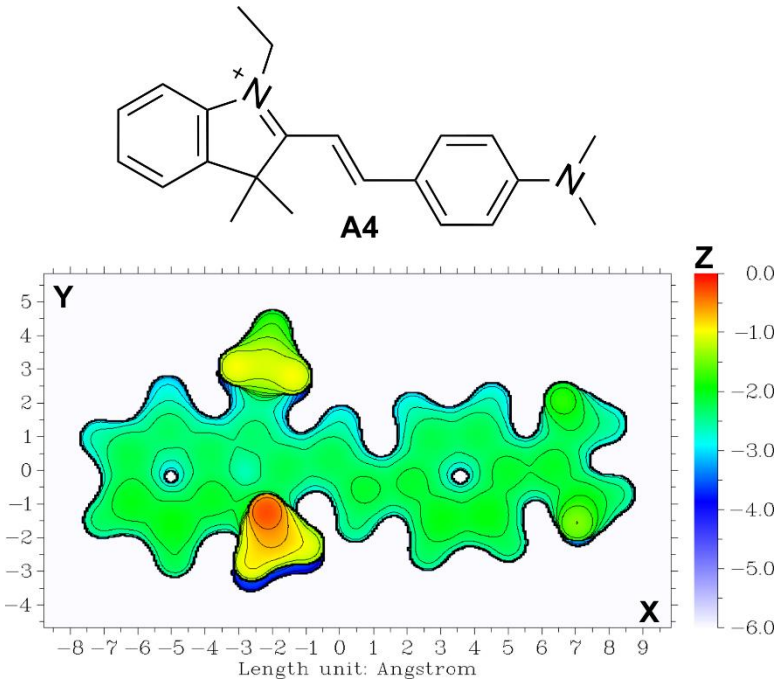

*Figure S81. The chemical structure and distance projection map of **A4** calculated at the ωB97XD/Def2SVP level in the water.*

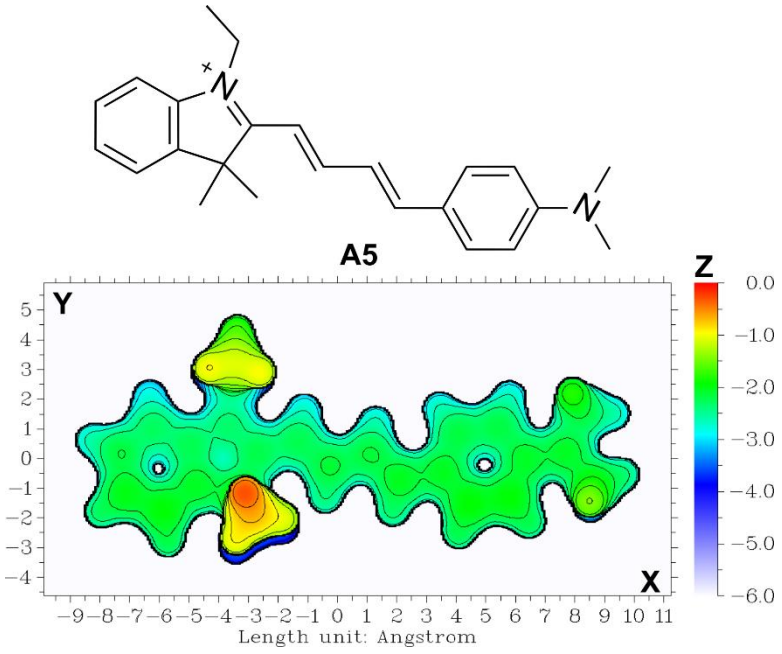

*Figure S 82. The chemical structure and distance projection map of **A5** calculated at the ωB97XD/Def2SVP level in the water.*

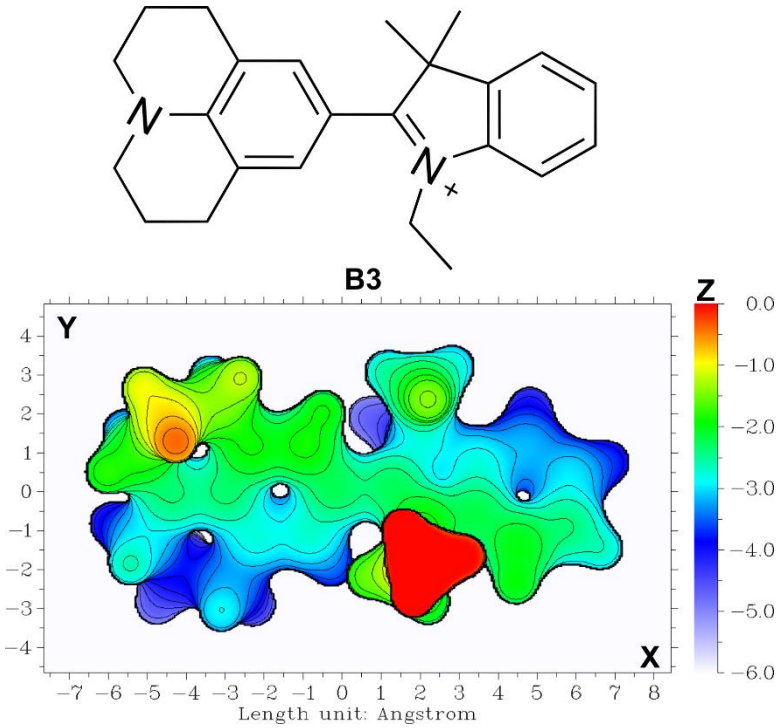

*Figure S83. The chemical structure and distance projection map of **B3** calculated at the ωB97XD/Def2SVP level in the water.*

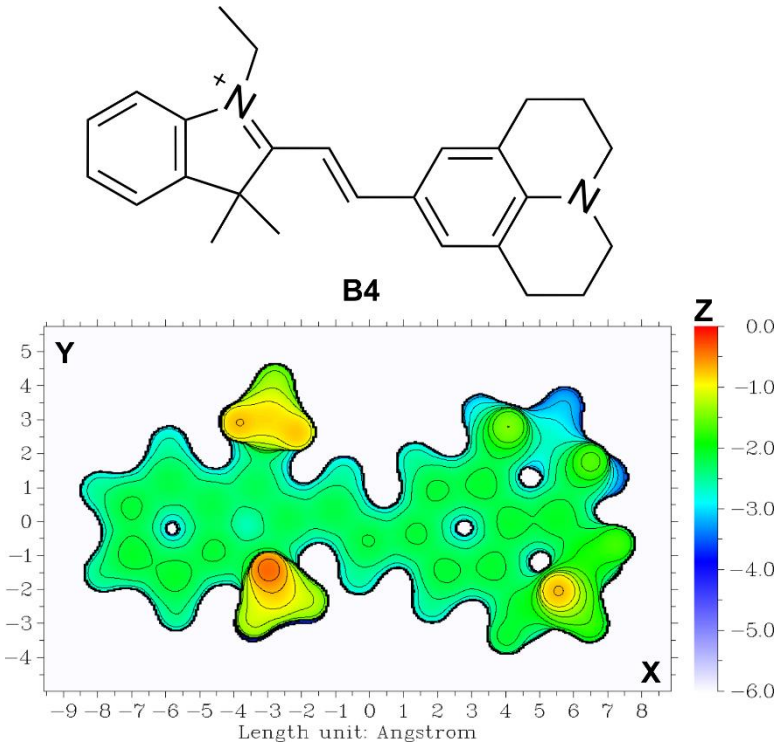

*Figure S84. The chemical structure and distance projection map of **A4** calculated at the ωB97XD/Def2SVP level in the water.*

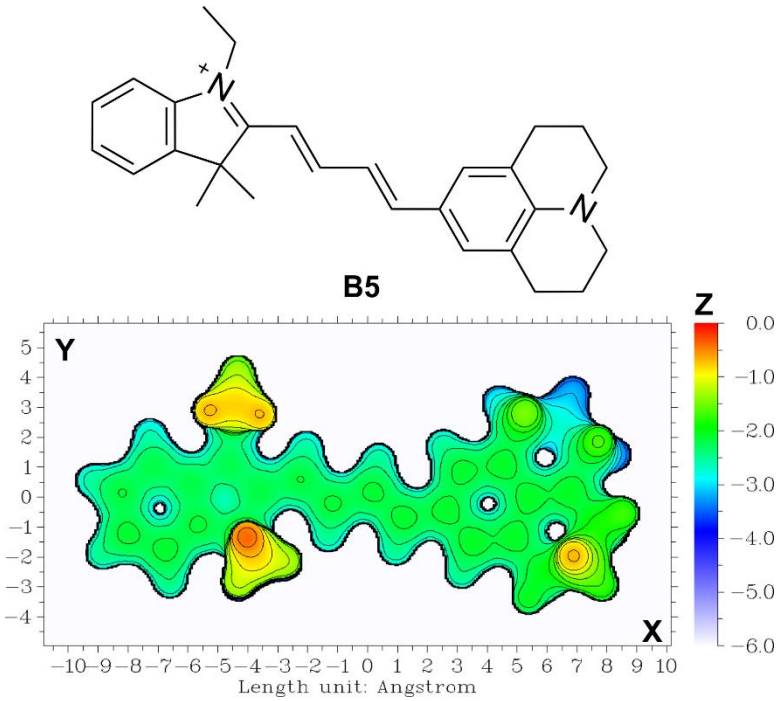

*Figure S85. The chemical structure and distance projection map of **B5** calculated at the ωB97XD/Def2SVP level in the water.*

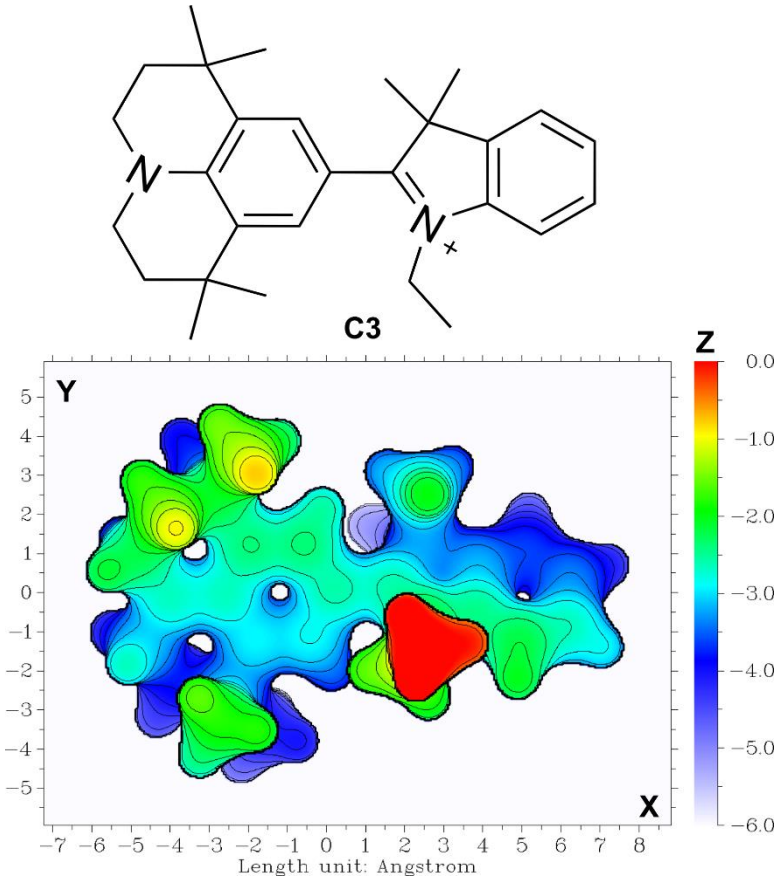

*Figure S86. The chemical structure and distance projection map of **C3** calculated at the ωB97XD/Def2SVP level in the water.*

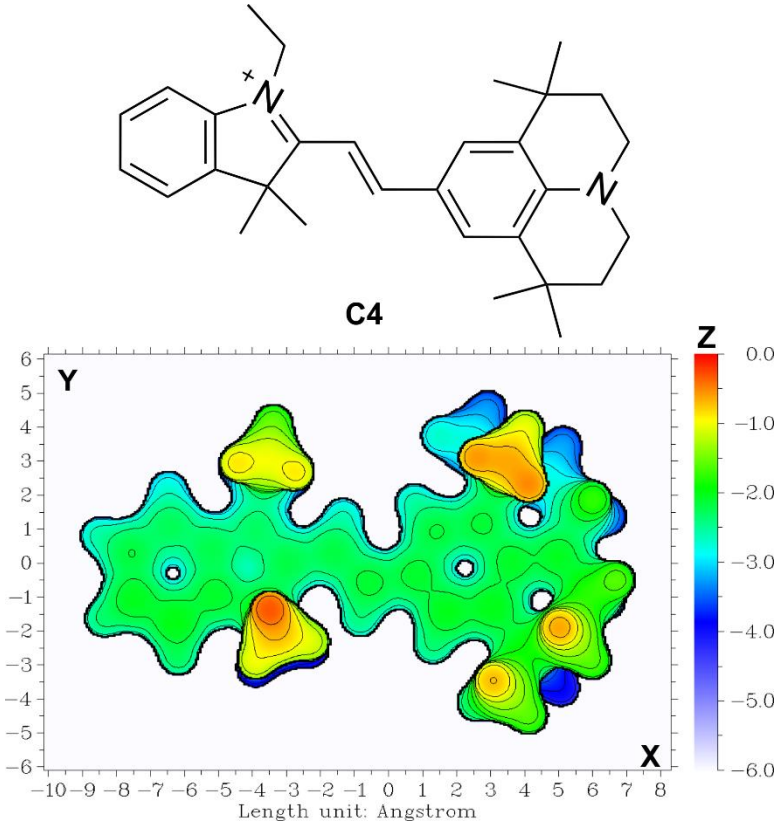

*Figure S87. The chemical structure and distance projection map of **C4** calculated at the ωB97XD/Def2SVP level in the water.*

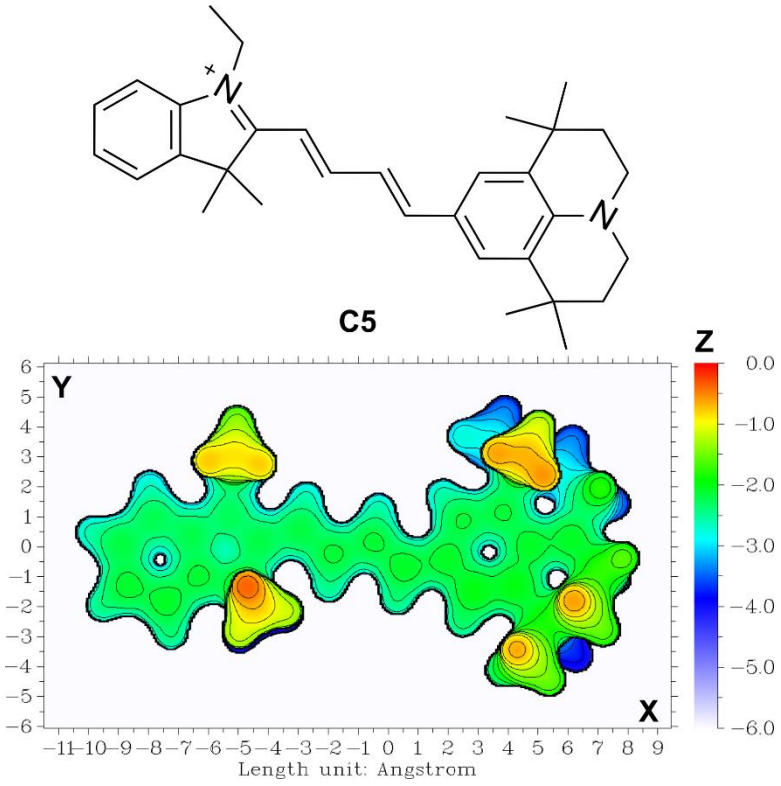

*Figure S88. The chemical structure and distance projection map of **A3** calculated at the ωB97XD/Def2SVP level in the water.*

8. Confocal Imaging of A*β* Fibrils Using A4, B3, and C3

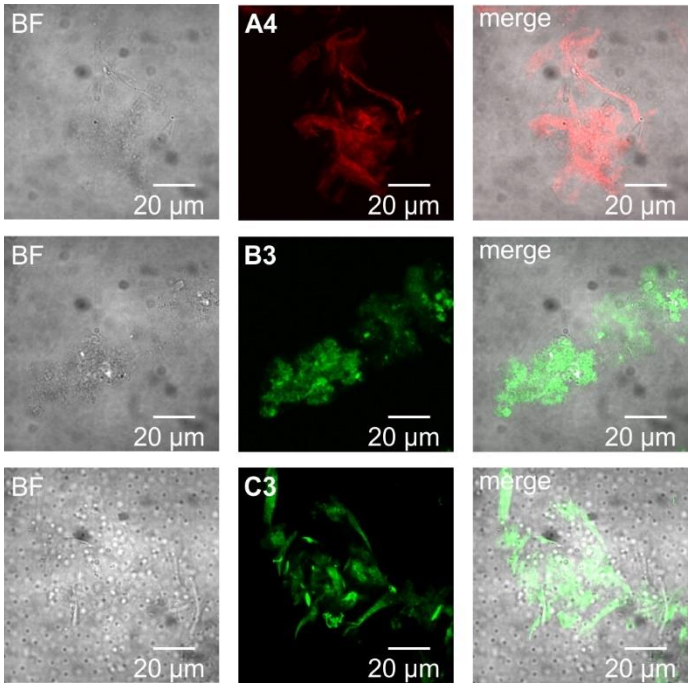

*Figure S89. Confocal imaging of Aβ fibrils using **A4**, **B3**, and **C3**. BF stands for the bright field.*

9. Detection of aggregate species at different stages of A*β* aggregation and the effect of dyes on the kinetics of Aβ aggregation using ThT, C3 and A4

The central issues of our study regarded the detection of aggregate species at different stages of Aβ aggregation and the effect of dyes on the kinetics of Aβ aggregation. However, the process of protein aggregate growth is inherently complex and subject to various factors, such as culture conditions and different batches of Aβ proteins, which can affect the outcomes of experiments.

Our initial attempts to isolate individual aggregate species proved challenging as the transition state species before fibrils were unstable and susceptible to environmental conditions such as shaking and the addition of solvents during the introduction of dyes.

To overcome this obstacle, we developed a different strategy that involved modifying the growth conditions and introducing dyes at different stages of the protein aggregation process. This approach allowed us to observe the dynamic process of aggregate growth and track the behavior of different species.

Our experiments demonstrated that A4 and C3 dyes were more effective than ThT at recognizing the earlier species of protein aggregates. Importantly, all three dyes were able to track the dynamic process of aggregate growth, providing valuable insights into the mechanisms of protein aggregation. The detailed experiments and results are as follows.

To investigate the effect of dyes on the aggregation kinetics of Aβ40, we monitored the aggregation process of 25 μM Aβ40 monomer samples with the addition of 20 μM dye (1 μL from a stock solution of 2 mM to a total volume of 100 μL per well) at different time points (0 h, 12 h, and 38 h) using ThT, C3, and A4 dyes(Figure S90a). Fluorescence data were recorded using a Synergy™ H1M Multifunctional Microplate Reader with a bottom-reading mode in 96-well flat bottom plates sealed with a platemax film. Plates were shaken for 2 s before recording fluorescent data every 10 min. Each experiment was conducted in triplicates in a 96-well plate, and fluorescence intensities were measured at Ex = 450 nm/Em = 510 nm for ThT and C3 and Ex = 560 nm/Em = 610 nm for A4.

As illustrated in Figure S90b-d, the addition of dyes at various time points did not lead to significant changes in the aggregation kinetics of Aβ for each dye. The fluorescence intensity of C3 (Figure S90c) and A4 (Figure S90d) began to increase significantly at around 18 hours and stabilized after approximately 30 hours of growth. However, due to environmental factors, the fluorescence intensity exhibited substantial fluctuations at the moment of dye addition (12 hours, 38 hours). Given that the addition of dyes (C3 and A4) at different time points (0 hour vs 12 hours) results in similar fluorescence intensity profiles, we conclude that C3 and A4 do not affect the protein aggregation process.

In contrast, the fluorescence intensity of ThT increased in multiple stages (Figure S90b), and we were unable to identify the inflection point at which ThT fluorescence began to increase rapidly. We observed that the fluorescence intensity of ThT

continued to increase after adding the dye at 38 hours, whereas the fluorescence intensity of C3 or A4 remained stable (Figure S90b-d). These differences suggest that C3 and A4 monitor the protein aggregation process differently from ThT.

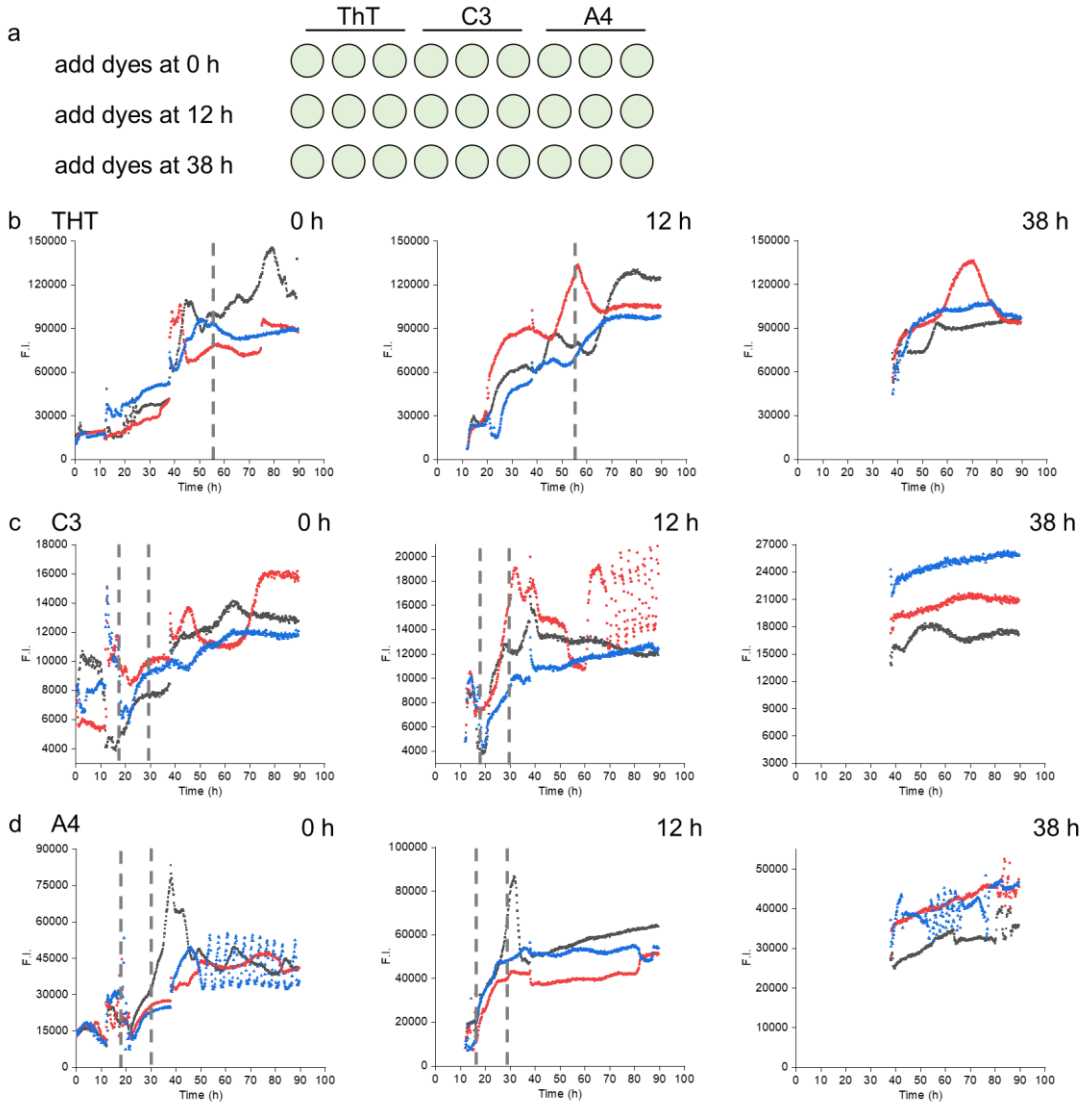

Figure S90. Schematic illustration of experimental designs to assess the effects of dyes on the aggregation kinetics. First, 100 μL of proteins are added to the test wells simultaneously, followed by the addition of dyes at different time points (0 h, 12 h, 38 h) during the aggregation process to monitor the fluorescence intensity in real time (a). Fluorescence intensity (F.I.) of ThT (b), C3 (c), and A4 (d) as a function of time during the aggregation of the Aβ protein. The dyes were added at different time points (0 h, 12 h, 38 h) in the aggregation process to monitor the fluorescence intensities in real time.

When comparing the smooth kinetic curve acquired by continuously placing the sample in the instrument (Fig. 5c and Fig. 6e) to the curve with significantly increased fluctuations when the dye is introduced midway (Figure S90), the overall protein aggregation trend remains similar. These experimental phenomena demonstrate that protein aggregation is a highly dynamic process. Moreover, co-incubating the dye with the protein enables sensitive monitoring of the protein aggregation process via changes in fluorescence intensities.

To further validate the accuracy and reproducibility of our prior data, we conducted additional dye-protein co-incubation aggregation kinetics experiments. While there

were some differences compared to the initial aggregation kinetic curve (probably because we used different batches of proteins), the fluorescence response times for C3 (33 h) and A4 (35 h) remained consistently earlier than that of ThT (48 h) (Figure S91), corroborating our earlier results (Fig. 5c, Fig. 6e).

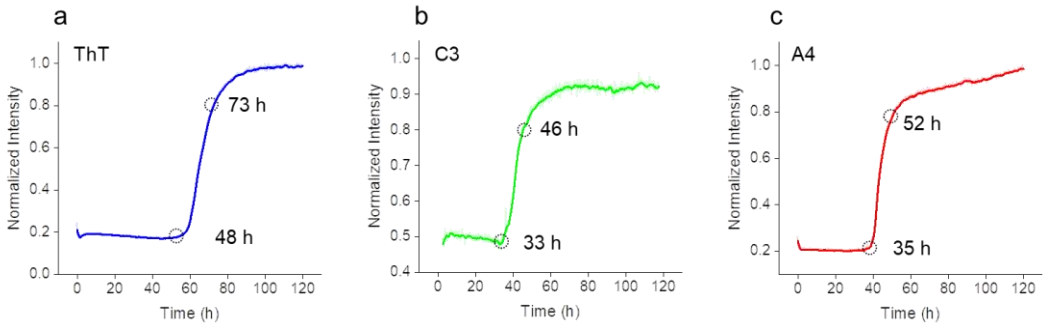

Figure S91. Normalized fluorescence intensity of ThT (a), C3 (b), and A4 (c) as a function of time during the aggregation of the Aβ protein in the co-incubation aggregation kinetics experiments.

The experiments presented consistently demonstrate that C3 or A4 responds to the aggregation process earlier than ThT. Since the three dyes do not affect protein aggregation processes, the different onset time show that the species detected by C3/A4 differ from those detected by ThT, potentially representing precursor structures to the species identified by ThT.

To further investigate this hypothesis, based on the referee's suggestion, a competition experiment between A4 and ThT was conducted (in parallel with the previous experiment depicted in Figure S90). Three sample groups were prepared, containing only ThT, only A4, or equal concentrations of A4 and ThT. The kinetic curves for samples with ThT or A4 alone (Figure S92b, c) resemble those in Figure S90b, d.

In the mixed sample, the relative changes in fluorescence signals of A4 and ThT (collected from their respective channels) over time were found to be identical (Figure S92d, e). Furthermore, the kinetic curves of mixed A4 and ThT samples were the same as those of A4 alone. However, the intensity of ThT was one order of magnitude lower than the signal generated by A4. These findings suggest that A4 effectively binds to earlier aggregated species during protein aggregation, leaving fewer binding sites for ThT. Consequently, the fluorescence signals of ThT were significantly weaker. These observations support our claims that C3/A4 responds to precursor structures more effectively than ThT does.

Although we were unable to obtain the intermediate species to which A4 and C3 respond, Aβ fibrils were produced after incubating for 30 hours with continuous shaking at 250 rpm at 37 °C. All three dyes (ThT, C3, A4) were able to detect Aβ fibrils.

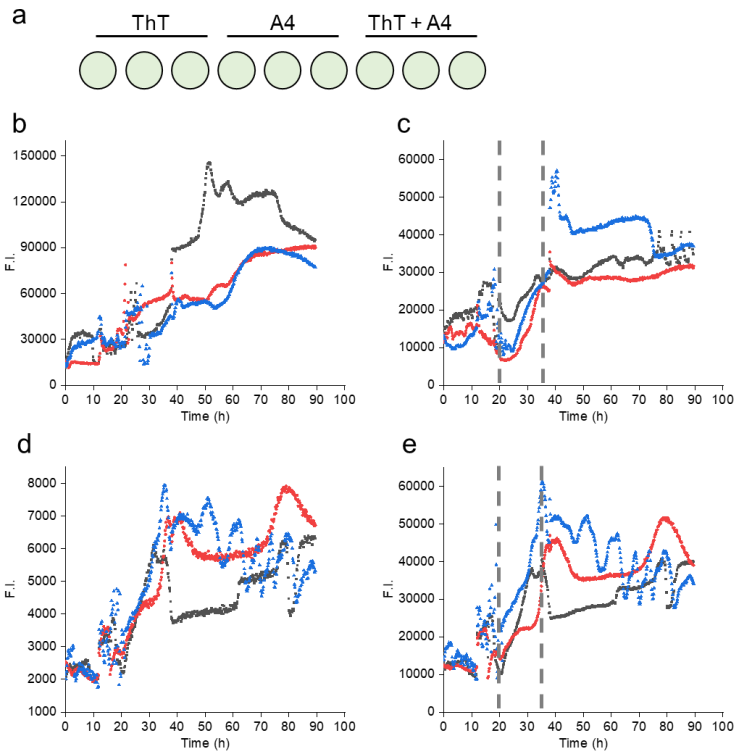

Figure S92. Schematic illustration of experimental designs to evaluate the effects of dyes (ThT, A4, mixed ThT and A4 at equal concentrations) on the aggregation kinetics (a). Fluorescence intensity (F.I.) of dyes as a function of time during the aggregation of the Aβ protein. Only ThT, measured at Ex = 450 nm/Em = 510 nm (b). Only A4, measured at Ex = 560 nm/Em = 610 nm (c). ThT and A4 at equal concentrations measured at Ex = 450 nm/Em = 510 nm (d). ThT and A4 at equal concentrations measured at Ex = 560 nm/Em = 610 nm (e).

Additionally, binding kinetic experiments between the collected fibrils and the three dyes revealed that ThT exhibits a slightly faster binding rate than A4 and C3 (Figure S93). Given ThT's dominant binding ability to aggregates, weak ThT signals in the mixed A4 and ThT sample would only occur if ThT-bound species formed later than A4-bound species. These results and analyses provide direct evidence supporting that A4 could detect intermediate species more effectively than ThT does.

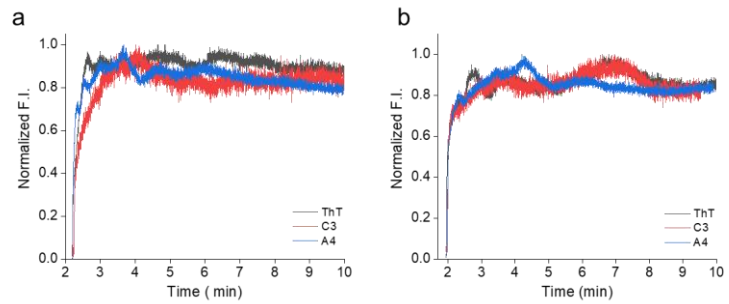

Figure S93. Binding kinetics of the three dyes (ThT, C3, A4) with different concentrations of Aβ40 fibrils (a.50 μL, b.100 μL, F.I., fluorescence intensity)

We further modified the culture conditions to investigate the protein aggregation process. By accelerating aggregation through continuous shaking at 250 rpm at 37 °C, we incubated 25 μM Aβ40 monomer samples to obtain proteins at various time points (0 h, 2.3 h, 4.3 h, 5.8 h, 6.3 h, 6.8 h, 7.3 h, 16.6 h). We then measured the fluorescence intensity of dye-protein complexes (1 μL from a stock solution of 2 mM dye to a total volume of 100 μL proteins per well) at different incubation times. The response trends of the three dyes were nearly identical (Figure S94a). Since previous results demonstrated that dyes do not affect protein aggregation kinetics and A4/C3 binds earlier species than ThT, the synchronous response curves of the three dyes shown in Figure S94a suggest that the protein aggregates' growth from oligomers to protofibrils is very susceptible to environmental conditions (i.e., shaking; Figure S95). The shaking process significantly accelerated the transition from oligomers to protofibrils, making the process indistinguishable between the three dyes.

Additionally, under the “same” experimental conditions (continuous shaking at 250 rpm at 37 °C, incubating 25 μM Aβ40 monomer samples to obtain proteins at different time points 0 h, 5.17 h, 11.1 h, 20 h, 24 h, 26 h, 30 h, 34 h, 46 h), we obtained similar time-evolution profile of fluorescent intensities. However, the onset time (t2 = ~20 hr) is considerably different from the previous experiment (t1 = ~4 hr). This inconsistent data again shows that the aggregation process is highly sensitive to external environmental perturbations and difficult to control.

We also closely examined the fluorescence changes of the three dyes after the fluorescence intensity reached saturation levels and observed that the intensity slightly decreased over time (Figure S94b). This likely represents the transformation process from protofibrils to fibrils (Figure S95). As fibrils form, the distance between the dyes dispersed in the aggregates diminishes, leading to some fluorescence quenching. This aggregation-induced fluorescence quenching is an intrinsic property of fluorescent dyes.

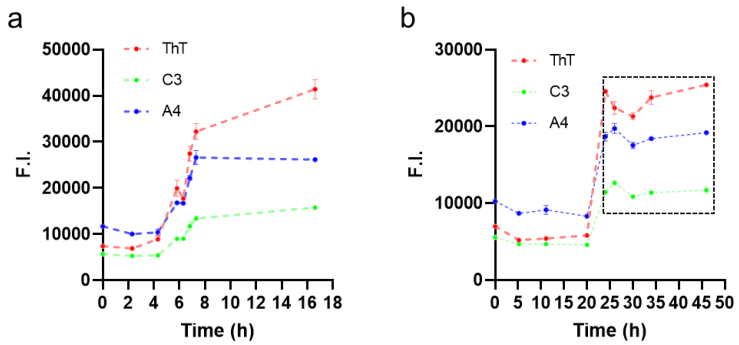

Figure S94. Time-dependent fibril formation of Aβ monitored by ThT, C3, and A4 (continuous shaking at 250 rpm at 37 ℃; dyes are incubated with 25 μM of Aβ40). (a) Experiment I; fluorescence intensity data were collected at 0 h, 2.3 h, 4.3 h, 5.8 h, 6.3 h, 6.8 h, 7.3 h, and 16.6 h, respectively. (b) Experiment II; fluorescence intensity data were collected at 0 h, 5.17 h, 11.1 h, 20 h, 24 h, 26 h, 30 h, 34 h, and 46 h, respectively. Although both experiments were conducted under the "same" conditions, the different onset times (t1 = ~4 hr in Experiment I and t2 = ~20 hr in Experiment II) demonstrate that the aggregation process is highly sensitive to external environmental perturbations and difficult to control.

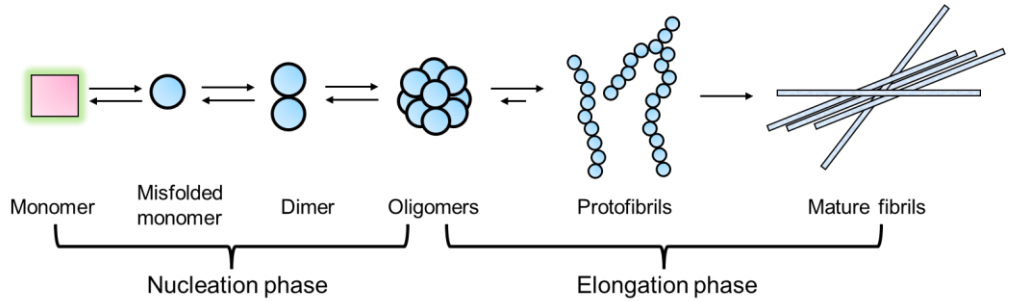

Figure S95. Schematic illustration of the Aβ aggregation process.

In summary, by adding dyes at various time points and monitoring the protein aggregation kinetics, we have demonstrated that the addition of dyes does not significantly impact the protein aggregation kinetics. Under our experimental conditions, the overall time-dependent response trends of the three dyes were similar. However, repeated experiments of real-time monitoring of protein aggregation kinetics through co-incubation of dyes and proteins revealed that the fluorescence response times for C3 and A4 were earlier than that of ThT, indicating that the aggregation progression monitored by C3 and A4 differs from that of ThT. We attempted to obtain intermediates by incubating proteins for different durations; however, their highly unstable nature and limited quantity hindered our ability to do so.

The experimental results presented thus far reveal that A4 and C3 can elucidate the dynamic growth process of protein aggregation. Moreover, these findings indicate that this dynamic process is characterized by species diversity and is highly sensitive to environmental factors, which complicates the isolation of species in the intermediate state of the aggregation process. We anticipate that utilizing in situ super-resolution fluorescence imaging within microfluidic devices will provide valuable insights into the protein aggregation process. By allowing both in situ tracking of the studied sample and improved imaging resolution, this technique can help overcome the challenges posed by the unstable nature and limited quantity of intermediate protein samples. This work is currently ongoing.

10. Additional Photophysical Properties of Hemi-Cyanine Derivatives

*Table S1. Photophysical properties, including peak UV-vis absorption wavelength (λ_{abs}), peak emission wavelength (λ_{em}), Stokes' shift ($\Delta\lambda$), maximum molecular absorption coefficient (ε), and quantum yield (φ) of **A1** in various solvents.*

Solvent	λ_{abs} (nm)	λ_{em} (nm)	$\Delta\lambda$ (nm)	ε (M^{-1} cm^{-1})	φ
Toluene	361	434	73	35568	0.181
$CHCl_3$	363	444	81	35496	0.363
DCM	364	444	80	36506	0.392
Dioxane	358	434	76	36202	0.224

EA	357	437	80	35392	0.185
EtOH	365	454	89	34652	0.795
MeCN	360	444	84	37642	0.406
MeOH	368	454	86	36200	0.455
DMSO	366	450	84	34498	0.699
PBS 7.4	369	462	93	26326	0.384

*Table S2. Photophysical properties, including peak UV-vis absorption wavelength (λ_{abs}), peak emission wavelength (λ_{em}), Stokes' shift ($\Delta\lambda$), maximum molecular absorption coefficient (ε), and quantum yield (φ) of **A2** in various solvents.*

Solvent	λ_{abs} (nm)	λ_{em} (nm)	$\Delta\lambda$ (nm)	ε (M^{-1} cm^{-1})	φ
Toluene	434	472	38	40708	0.255
$CHCl_3$	436	471	35	58716	0.191
DCM	436	473	37	59842	0.092
Dioxane	429	471	42	40638	0.107
EA	433	475	42	40184	0.028
EtOH	455	481	26	58310	0.008
MeCN	454	483	29	63618	0.003
MeOH	440	479	39	61978	0.004
DMSO	446	487	41	51582	0.015
PBS 7.4	438	478	40	53402	0.003

*Table S3. Photophysical properties, including peak UV-vis absorption wavelength (λ_{abs}), peak emission wavelength (λ_{em}), Stokes' shift ($\Delta\lambda$), maximum molecular absorption coefficient (ε), and quantum yield (φ) of **A3** in various solvents. NA refers to not applicable due to the vanishing fluorescence signal.*

Solvent	λ_{abs} (nm)	λ_{em} (nm)	$\Delta\lambda$ (nm)	ε (M^{-1} cm^{-1})	φ
Toluene	447	NA	NA	18737	0.000
$CHCl_3$	455	NA	NA	22654	0.000
DCM	458	NA	NA	36625	0.000
Dioxane	444	NA	NA	25102	0.000

EA	441	NA	NA	23263	0.000
EtOH	442	NA	NA	18090	0.000
MeCN	440	NA	NA	28798	0.000
MeOH	440	NA	NA	22858	0.000
DMSO	442	NA	NA	22880	0.000
PBS 7.4	437	NA	NA	23886	0.000

*Table S4. Photophysical properties, including peak UV-vis absorption wavelength (λ_{abs}), peak emission wavelength (λ_{em}), Stokes' shift ($\Delta\lambda$), maximum molecular absorption coefficient (ε), and quantum yield (φ) of **A4** in various solvents.*

Solvent	λ_{abs} (nm)	λ_{em} (nm)	$\Delta\lambda$ (nm)	ε (M^{-1} cm^{-1})	φ
Toluene	559	601	42	55054	0.001
$CHCl_3$	562	592	30	74452	0.011
DCM	561	595	34	85420	0.009
Dioxane	556	598	42	22432	0.003
EA	545	595	50	47622	0.002
EtOH	549	590	41	64162	0.006
MeCN	544	595	51	62528	0.002
MeOH	546	589	43	65340	0.003
DMSO	550	603	53	56726	0.013
PBS 7.4	543	594	51	55836	0.002

*Table S5. Photophysical properties, including peak UV-vis absorption wavelength (λ_{abs}), peak emission wavelength (λ_{em}), Stokes' shift ($\Delta\lambda$), maximum molecular absorption coefficient (ε), and quantum yield (φ) of **A5** in various solvents.*

Solvent	λ_{abs} (nm)	λ_{em} (nm)	$\Delta\lambda$ (nm)	ε (M^{-1} cm^{-1})	φ
Toluene	637	701	64	63806	0.009
$CHCl_3$	644	697	53	87024	0.077
DCM	647	699	52	98498	0.069
Dioxane	630	699	69	20052	0.019

EA	605	699	94	56604	0.008
EtOH	621	698	77	74500	0.023
MeCN	602	699	97	60098	0.008
MeOH	613	697	84	66160	0.011
DMSO	610	712	102	55176	0.031
PBS 7.4	578	694	116	45328	0.007

*Table S6. Photophysical properties, including peak UV-vis absorption wavelength (λ_{abs}), peak emission wavelength (λ_{em}), Stokes' shift ($\Delta\lambda$), maximum molecular absorption coefficient (ε), and quantum yield (φ) of **B1** in various solvents.*

Solvent	λ_{abs} (nm)	λ_{em} (nm)	$\Delta\lambda$ (nm)	ε (M^{-1} cm^{-1})	φ
Toluene	377	450	73	32078	0.546
$CHCl_3$	384	462	78	29062	0.648
DCM	383	460	77	33862	0.760
Dioxane	372	450	78	32308	0.645
EA	373	450	77	30814	0.597
EtOH	387	463	76	31722	0.716
MeCN	380	458	78	32390	0.711
MeOH	389	466	77	31012	0.477
DMSO	386	465	79	33376	0.810
PBS 7.4	392	475	83	18120	0.302

*Table S7. Photophysical properties, including peak UV-vis absorption wavelength (λ_{abs}), peak emission wavelength (λ_{em}), Stokes' shift ($\Delta\lambda$), maximum molecular absorption coefficient (ε), and quantum yield (φ) of **B2** in various solvents.*

Solvent	λ_{abs} (nm)	λ_{em} (nm)	$\Delta\lambda$ (nm)	ε (M^{-1} cm^{-1})	φ
Toluene	468	487	19	42296	0.050
$CHCl_3$	472	487	15	55422	0.041
DCM	477	494	17	56534	0.018
Dioxane	463	487	24	37282	0.043

EA	465	489	24	40288	0.017
EtOH	477	496	19	56008	0.016
MeCN	477	496	19	56358	0.011
MeOH	475	496	21	54462	0.008
DMSO	479	502	23	52342	0.021
PBS 7.4	475	494	19	46514	0.005

*Table S8. Photophysical properties, including peak UV-vis absorption wavelength (λ_{abs}), peak emission wavelength (λ_{em}), Stokes' shift ($\Delta\lambda$), maximum molecular absorption coefficient (ε), and quantum yield (φ) of **B3** in various solvents.*

Solvent	λ_{abs} (nm)	λ_{em} (nm)	$\Delta\lambda$ (nm)	ε (M^{-1} cm^{-1})	φ
Toluene	470	514	44	20540	0.000
$CHCl_3$	481	525	44	43839	0.000
DCM	482	522	40	54706	0.000
Dioxane	487	525	38	9748	0.000
EA	475	510	35	11778	0.000
EtOH	475	514	39	42387	0.000
MeCN	473	520	47	45562	0.000
MeOH	473	518	45	37450	0.000
DMSO	475	516	41	39138	0.000
PBS 7.4	472	515	43	37241	0.000

*Table S9. Photophysical properties, including peak UV-vis absorption wavelength (λ_{abs}), peak emission wavelength (λ_{em}), Stokes' shift ($\Delta\lambda$), maximum molecular absorption coefficient (ε), and quantum yield (φ) of **B4** in various solvents.*

Solvent	λ_{abs} (nm)	λ_{em} (nm)	$\Delta\lambda$ (nm)	ε (M^{-1} cm^{-1})	φ
Toluene	593	618	25	102024	0.001
$CHCl_3$	591	617	26	133184	0.009
DCM	592	619	27	143672	0.003
Dioxane	586	612	26	68832	0.003

EA	581	614	33	90590	0.002
EtOH	582	612	30	117234	0.004
MeCN	580	615	35	107200	0.002
MeOH	580	612	32	115184	0.002
DMSO	585	624	39	98724	0.010
PBS 7.4	578	612	34	96666	0.002

*Table S10. Photophysical properties, including peak UV-vis absorption wavelength (λ_{abs}), peak emission wavelength (λ_{em}), Stokes' shift ($\Delta\lambda$), maximum molecular absorption coefficient (ε), and quantum yield (φ) of **B5** in various solvents.*

Solvent	λ_{abs} (nm)	λ_{em} (nm)	$\Delta\lambda$ (nm)	ε (M^{-1} cm^{-1})	φ
Toluene	692	742	50	102808	0.005
$CHCl_3$	690	735	45	136968	0.035
DCM	692	735	43	160600	0.007
Dioxane	677	728	51	51102	0.012
EA	664	733	69	81276	0.004
EtOH	674	727	53	112730	0.008
MeCN	667	727	60	100652	0.003
MeOH	668	726	58	113866	0.004
DMSO	672	739	67	85222	0.014
PBS 7.4	654	725	71	67632	0.003

*Table S11. Photophysical properties, including peak UV-vis absorption wavelength (λ_{abs}), peak emission wavelength (λ_{em}), Stokes' shift ($\Delta\lambda$), maximum molecular absorption coefficient (ε), and quantum yield (φ) of **C1** in various solvents.*

Solvent	λ_{abs} (nm)	λ_{em} (nm)	$\Delta\lambda$ (nm)	ε (M^{-1} cm^{-1})	φ
Toluene	373	445	72	22306	0.568
$CHCl_3$	383	460	77	22652	0.657
DCM	382	458	76	23798	0.810
Dioxane	374	447	73	23196	0.700

EA	374	450	76	23976	0.619
EtOH	386	462	76	22760	0.780
MeCN	381	458	77	24078	0.692
MeOH	390	466	76	23478	0.633
DMSO	385	462	77	23378	0.862
PBS 7.4	388	478	90	12910	0.180

*Table S12. Photophysical properties, including peak UV-vis absorption wavelength (λ_{abs}), peak emission wavelength (λ_{em}), Stokes' shift ($\Delta\lambda$), maximum molecular absorption coefficient (ε), and quantum yield (φ) of **C2** in various solvents.*

Solvent	λ_{abs} (nm)	λ_{em} (nm)	$\Delta\lambda$ (nm)	ε (M^{-1} cm^{-1})	φ
Toluene	463	482	19	35684	0.153
$CHCl_3$	468	483	15	46552	0.087
DCM	470	487	17	49716	0.030
Dioxane	458	482	24	33876	0.118
EA	462	485	23	39404	0.030
EtOH	475	491	16	48896	0.014
MeCN	474	494	20	50656	0.005
MeOH	473	491	18	49318	0.007
DMSO	476	499	23	44480	0.028
PBS 7.4	472	491	19	35926	0.005

*Table S13. Photophysical properties, including peak UV-vis absorption wavelength (λ_{abs}), peak emission wavelength (λ_{em}), Stokes' shift ($\Delta\lambda$), maximum molecular absorption coefficient (ε), and quantum yield (φ) of **C3** in various solvents. NA refers to not applicable due to the vanishing fluorescence signal.*

Solvent	λ_{abs} (nm)	λ_{em} (nm)	$\Delta\lambda$ (nm)	ε (M^{-1} cm^{-1})	φ
Toluene	470	NA	NA	31821	0.000
$CHCl_3$	478	NA	NA	45040	0.000
DCM	479	NA	NA	55757	0.000
Dioxane	467	NA	NA	36679	0.000

EA	471	NA	NA	34101	0.000
EtOH	471	NA	NA	41910	0.000
MeCN	470	NA	NA	43937	0.000
MeOH	471	NA	NA	41178	0.000
DMSO	473	NA	NA	38115	0.000
PBS 7.4	469	NA	NA	36297	0.000

*Table S14. Photophysical properties, including peak UV-vis absorption wavelength (λ_{abs}), peak emission wavelength (λ_{em}), Stokes' shift ($\Delta\lambda$), maximum molecular absorption coefficient (ε), and quantum yield (φ) of **C4** in various solvents.*

Solvent	λ_{abs} (nm)	λ_{em} (nm)	$\Delta\lambda$ (nm)	ε (M^{-1} cm^{-1})	φ
Toluene	583	612	29	68898	0.002
$CHCl_3$	588	612	24	108454	0.009
DCM	587	616	29	130820	0.003
Dioxane	577	606	29	46036	0.012
EA	576	609	33	74264	0.003
EtOH	578	612	34	107178	0.005
MeCN	575	614	39	101908	0.002
MeOH	577	610	33	106424	0.002
DMSO	581	618	37	91578	0.012
PBS 7.4	573	607	34	85622	0.003

*Table S15. Photophysical properties, including peak UV-vis absorption wavelength (λ_{abs}), peak emission wavelength (λ_{em}), Stokes' shift ($\Delta\lambda$), maximum molecular absorption coefficient (ε), and quantum yield (φ) of **C5** in various solvents.*

Solvent	λ_{abs} (nm)	λ_{em} (nm)	$\Delta\lambda$ (nm)	ε (M^{-1} cm^{-1})	φ
Toluene	690	731	41	105874	0.007
$CHCl_3$	689	728	39	139026	0.047
DCM	692	731	39	153798	0.009
Dioxane	675	721	46	68426	0.017

EA	666	726	60	84526	0.005
EtOH	672	725	53	105046	0.011
MeCN	670	726	56	99952	0.004
MeOH	668	720	52	108772	0.005
DMSO	671	737	66	84268	0.019
PBS 7.4	656	720	64	65202	0.004

10. Solvent viscosity

Table S16. The viscosity of glycerol/methanol binary mixture at various volume ratios of glycerol at 25°C.

Glycerol %	0	10	20	30	40	50	60	70	80	90	100
Viscosity (mPa·S)	0.53	0.92	1.58	2.97	5.60	11.18	24.52	53.27	135.72	366.45	920.88

11. References

1. M. J. Frisch, G. W. Trucks, H. B. Schlegel, G. E. Scuseria, M. A. Robb, J. R. Cheeseman, G. Scalmani, V. Barone, G. A. Petersson, H. Nakatsuji, X. Li, M. Caricato, A. V. Marenich, J. Bloino, B. G. Janesko, R. Gomperts, B. Mennucci, H. P. Hratchian, J. V. Ortiz, A. F. Izmaylov, J. L. Sonnenberg, Williams, F. Ding, F. Lipparini, F. Egidi, J. Goings, B. Peng, A. Petrone, T. Henderson, D. Ranasinghe, V. G. Zakrzewski, J. Gao, N. Rega, G. Zheng, W. Liang, M. Hada, M. Ehara, K. Toyota, R. Fukuda, J. Hasegawa, M. Ishida, T. Nakajima, Y. Honda, O. Kitao, H. Nakai, T. Vreven, K. Throssell, J. A. Montgomery Jr., J. E. Peralta, F. Ogliaro, M. J. Bearpark, J. J. Heyd, E. N. Brothers, K. N. Kudin, V. N. Staroverov, T. A. Keith, R. Kobayashi, J. Normand, K. Raghavachari, A. P. Rendell, J. C. Burant, S. S. Iyengar, J. Tomasi, M. Cossi, J. M. Millam, M. Klene, C. Adamo, R. Cammi, J. W. Ochterski, R. L. Martin, K. Morokuma, O. Farkas, J. B. Foresman and D. J. Fox, *Journal*, 2016.
2. C. Wang and Y. Yuan, *Phys. Chem. Chem. Phys.* , 2018, **20**, 16777-16785.
3. A. V. Marenich, C. J. Cramer and D. G. Truhlar, *J. Chem. Theory Comput.* , 2010, **6**, 2829-2844.
4. M. Cossi and V. Barone, *J. Chem. Phys.*, 2001, **115**, 4708-4717.
5. M. Caricato, B. Mennucci, J. Tomasi, F. Ingrosso, R. Cammi, S. Corni and G. Scalmani, *J Chem Phys*, 2006, **124**, 124520.
6. C. Wang, Q. Qiao, W. Chi, J. Chen, W. Liu, D. Tan, S. McKechnie, D. Lyu, X. F. Jiang, W. Zhou, N. Xu, Q. Zhang, Z. Xu and X. Liu, *Angew. Chem. Int. Ed.*, 2020, **59**, 10160-10172.
7. C. Wang and Q. Zhang, *J. Phys. Chem. C* 2018, **123**, 4407-4416.
8. X. Y. Zheng, F. Y. Cao, C. Wang, T. Tsuboi, Y. H. Zhu, Q. Ai, C. Deng, D. Wang, L. W. Su, Z. Liu and Q. S. Zhang, *J. Mater. Chem. C*, 2020, **8**, 10021-10030.
9. R. L. Martin, *J. Chem. Phys.*, 2003, **118**, 4775-4777.
10. C. A. Guido, P. Cortona, B. Mennucci and C. Adamo, *J. Chem. Theory Comput.* , 2013, **9**, 3118-3126.
11. T. Lu and F. Chen, *J. Mol. Graph. Model.*, 2012, **38**, 314-323.
12. T. Lu and F. Chen, *J. Comput. Chem.* , 2012, **33**, 580-592.
13. C. Wurth, M. Grabolle, J. Pauli, M. Spieles and U. Resch-Genger, *Nat. Protoc.* , 2013, **8**, 1535-1550.
14. D. Oesch and N. W. Luedtke, *Chem. Commun.*, 2015, **51**, 12641-12644.
15. K. Wang, W. Shi, J. Jia, S. Chen and H. Ma, *Talanta*, 2009, **77**, 1795-1799.
16. V. Martinez and M. Henary, *Chem. Eur. J.*, 2016, **22**, 13764-13782.
17. P. R. Hammond, *Journal of Photochemistry*, 1979, **10**, 467-471.